AN ABSTRACT OF THE THESIS OF

Shingo Ichikawa for the degree of Master of Ocean Engineering in Ocean Engineering presented on December 9, 2005.

Title: Laboratory Observations of Tsunami Runup on a Complex 3D Bathymetry using PIV

Abstract approved:

Redacted for Privacy

Daniel T. Cox

This thesis presents the details of a large-scale laboratory experiment to study the runup velocity on a complex 3D bathymetry. The PIV measurements including the instrumental setup, the recording procedure, and the image processing are presented.

Tsunami inundation directly affects the coastal population and is one of the most important tsunami processes to be understood because most of the deaths occurred during inundation. Therefore, it is vital that we understand the dominant mechanisms during tsunami inundation to predict the inundation level and inundation velocity to help reduce loss of life and damage in future events. Numerical simulations have been used to predict the maximum tsunami inundation level and run-up velocity. However, field data that can be used to validate the numerical models is limited. Laboratory measurements can be used to verify or refuse the present models.

A 3D complex physical model was constructed in the Tsunami Wave Basin at the O.H. Hinsdale Wave Research Laboratory at Oregon State University. The objective of the experiment was to measure both the tsunami velocity at offshore locations and the run-up velocities on the bathymetry. Since real world tsunami inundation may occur with or without wave breaking, and inundation with wave breaking, laboratory wave conditions were also chosen to have both types. Wave gages and ADVs (acoustic Doppler velocimeters) were used to measure the offshore wave height and wave speed, respectively, and PIV (particle

image velocimetry) was used to measure the shallow water and run-up wave velocities on land where it could not be measured by the ADV. The data acquired in this experiment were placed online as a part of the shared-use concept of the NEES (National Science Foundation's Network for Earthquake Engineering Simulation).

Laboratory Observations of Tsunami Runup on a Complex 3D Bathymetry using PIV

by
Shingo Ichikawa

A THESIS

submitted to

Oregon State University

in partial fulfillment of
the requirements for the
degree of

Master of Ocean Engineering

Presented December 9, 2005
Commencement June 2006

Master of Ocean Engineering thesis of Shingo Ichikawa presented on December 9, 2005.

APPROVED:

Redacted for Privacy

Major Professor, representing Ocean Engineering

Redacted for Privacy

Head of the Department of Civil, Construction, and Environmental Engineering

Redacted for Privacy

Dean of the Graduate School

I understand that my thesis will become part of the permanent collection of Oregon State University libraries. My signature below authorizes release of my thesis to any reader upon request.

Redacted for Privacy

Shingo Ichikawa, Author

ACKNOWLEDGEMENTS

The work of this thesis was partially funded by the George E. Brown Jr. Network for Earthquake Engineering Simulation (NEES) program of the National Science Foundation (CMS-0086571).

I would like to express my gratitude to my advisor, Daniel Cox, for providing me with the opportunity to work alongside him for the past two years. I would also like to thank Roy Rathja, Harry Yeh, and Solomon Yim for serving as my committee members and for their assistance throughout the project. I am also thankful for the support given to me by fellow graduate students, including Christopher Scott and Sungwon Shin. The success of the experiment was also due to the hard work of Charlie Bisgard, Chris Johnson, Daniel Grant, James Lynch, Yusuke Matsumura and the HWRL staff. I must thank my roommates, Brady Richmond and Jason Magalen for their help and friendship. I also thank Michiru Hirayama for her support and smile. Finally, I would like to thank my family for their encouragements and support during my study at Oregon State University.

TABLE OF CONTENTS

TABLE OF CONTENTS (Continued)

TABLE OF CONTENTS (Continued)

LIST OF FIGURES

LIST OF FIGURES (Continued)

LIST OF FIGURES (Continued)

LIST OF FIGURES (Continued)

LIST OF FIGURES (Continued)

LIST OF TABLES

LIST OF APPENDIX FIGURES

LIST OF APPENDIX FIGURES (Continued)

LIST OF APPENDIX TABLES

1. Introduction

The 2004 Indian Ocean earthquake, sometimes referred as the Sumatra-Andaman earthquake, generated the tsunami that killed an estimated 275,000 people in the coastal areas of Indonesia, Sri Lanka, South India, Thailand and other countries. The estimated magnitude of the earthquake ranges from 9.0 to 9.3, which makes it the second largest ever recorded.

Tsunamis have different characteristics in deep and shallow water. In deep water, tsunamis generally have an extremely long wavelength (~ 500 km), a small wave height, and travel at 500 km/hr to 1000 km/hr. It is also worth noting that tsunamis have a different distribution of energy than other types of water waves. For example, the energy contained in a wind wave is primarily concentrated at the water surface. However, the energy in a tsunami is uniformly distributed over the entire water depth, even in very deep water. In shallow water areas, a tsunami's speed decreases due to decreasing water depth and its shape deforms to produce a larger wave height.

Tsunami inundation directly affects the coastal population and is one of the most important tsunami processes to be understood because most of the deaths occurred during inundation. Therefore, it is vital that the dominant mechanisms during tsunami inundation should be understood to predict the inundation level and inundation velocity to help reduce loss of life and damage in future events. Numerical simulations have been used to predict the maximum tsunami inundation level and run-up velocity. However, field data that can be used to validate the numerical models is limited. Laboratory measurements can be used to verify or refuse the present models.

A 3D complex physical model was constructed in the Tsunami Wave Basin at the O.H. Hinsdale Wave Research Laboratory at Oregon State University. The objective of the experiment

was to measure both the tsunami velocity at offshore locations and the run-up velocities on the bathymetry. Since real world tsunami inundation may have inundation with or without wave breaking, and inundation with wave breaking, laboratory wave conditions were also chosen to have both types. Wave gages and ADVs (acoustic Doppler velocimeters) were used to measure the offshore wave height and wave speed, respectively, and PIV (particle image velocimetry) was used to measure the shallow water and run-up wave velocities on land where it could not be measured by the ADV. The data acquired in this experiment were placed online as a part of the shared-use concept of the NEES (National Science Foundation's Network for Earthquake Engineering Simulation). Chapter 2 gives a literature review for tsunami inundation, PIV and other work related to this project. Chapter 3 gives details of the experimental facilities and PIV technique. Chapter 4 gives the procedure of PIV recording and image processing using a commercial software package. Chapter 5 gives the results and the comparisons of PIV data with that of ADV for both breaking and non-breaking waves. Chapter 6 gives the conclusions of this project.

2. Literature review

2.1 Tsunami runup velocity and inundation

Three dimensional laboratory measurements of tsunami inundation were conducted by Briggs et al. (1994). The dimensions of the basin used were 30 m wide by 25 m long by 32 cm deep. For the Briggs experiment, tsunami waves were represented by solitary waves. There are strict limitations for properties of the wavemaker, such as stroke limitation, water depth limitation and so on. Therefore, a wave with maximum wavelength of all wave cases was chosen as a model wave to represent the characteristics of a tsunami. A linear relationship between the runup distance and runup velocity was found, but for this experiment the bathymetry was idealized as linear and uniform in the along tank direction.

Runup of solitary waves on a circular laboratory island was observed by Briggs et al. (1995). It presented the runup profile at twenty locations around the perimeter of the island. The maximum inundation was observed at the rear of the circular island. From this experiment, it appeared that the level of inundation was highly related to the shape of the bathymetry. Run-up velocity is one of the most important parameters for designing the coastal structures. Tsutsumi et al. (2000) suggested a method of estimating the velocity of tsunami flow by estimating the forces exerted on damaged structures constructed along the coast.

Theoretical, experimental, and field studies of run-up phenomena are briefly discussed by Liu et al. (1990). Shallow-water equations can be applied to calculate wave velocity and water surface elevation in 1D and non breaking waves. It was mentioned that the shallow water equations can be used to solve a bore (broken waves).

2.2 Particle image velocimetry

The general system of PIV is to calculate flow velocity by analyzing particle displacements from multiple images. The principal of the PIV mechanism and technique were detailed by Kompenhans et al. (1998). PIV is applied for laboratory flows which are often small scale models. There are few papers presented the PIV measurements for large scale models. However, there have been some field applications. Fujita et al. (1998) presented the comparisons of the large scale open channel flow by PIV and ADV, which showed good agreements. Greated et al. (1992) presented the very useful review for the PIV technique in the coastal engineering laboratory. Several important criteria for PIV measurements were deiscussed: the seeding density, illumination interval, focus, and the photographic magnification and the error sources. The accuracy of PIV is determined by two phases. One is the recording of the flow, and the other is the analysis of the images. To acquire the most reliable results, the flow should be well seeded and the interrogation window should be large enough to calculate the local velocity. It was suggested that once these conditions are satisfied, the final error can be less than 2% of the maximum velocity measured.

The velocity measurements of a plunging breaker were conducted by Emarat et al. (2000). They used PIV to measure the plunging breaker and conducted a numerical model simulation based on the Navier-Stokes equations. The comparisons for PIV and the numerical model generally showed good agreement. However, the PIV technique could not obtain the maximum horizontal velocity at the wave crest. Therefore, there were some uncertainties about the maximum velocity at the breaker. Yamada et al. (2000) showed good observation of the breaker deformation using the PIV. They presented the spatial distribution of the horizontal and vertical velocities and the kinetic energy at the three phases of the wave: non-breaking, spilling, and plunging. It was observed that as the wave phase proceeded from non-breaking, spilling to plunging, the velocity and the energy increased around at wave crest area.

2.3 Other work directly related to this project

There were other experiments using the same or similar bathymetry as was used for this project. Those reports are briefly listed as follows:

- Design and Implementation of a Physical Model for Keystone Harbor, Washington, (Richmond, 2005)
- Keystone Phase II: Alteration of the Harbor and Relocation of the Jetty (Bisgard, Grier, Ichikawa, 2005, unpublished report)
- 3D Physical Model of Tsunami Inundation over a Complex Bathymetry (Lynch, 2005, unpublished REU report)
- Breaking and non-breaking solitary wave impact pressures on a cylinder over a 3D bathymetry (Bisgard, 2005)

Richmond (2005) conducted the tests for currents and waves over a 1:40 scale physical model of Keystone Harbor (phase-I) in the Tsunami Wave Basin. A series of the tests were conducted to evaluate the performance of the existing and proposed jetty extension. Bisgard et al. (2005) conducted the current and wave tests over an alternative bathymetry of Keystone Harbor (phase-II). This alternative included widening of the harbor, dredging the navigation channel and relocating the existing jetty, and a LIDAR scan of the bathymetry used for the presented study. The measurements of free surface displacement and water particle velocity over the entire bathymetry (same as phase-II) were conducted by Lynch (2005). In addition, Bisgard (2005) measured the wave impact pressure on a circular cylinder located inside the harbor for both breaking and non-breaking solitary wave.

3. Facility and experimental technique

3.1 Laboratory facilities

This experiment was conducted in the Tsunami Wave Basin, which is 48.8 m long, 26.5 m wide, and 2.1 m deep. The wavemaker is a multidirectional, piston type with twenty-nine, 2 m high wave boards and a maximum stroke of 2.0 m. The 3D complex bathymetry, originally constructed for an earlier experiment, was kept in place for this experiment. Figure 1 shows the dry bathymetry.

Figure 1: 3D complex bathymetry in the Tsunami Wave Basin.

For the earlier project the bathymetry was surveyed using a LIDAR camera and was converted to a x, y, z grid with constant spacing of $\Delta x = \Delta y = 10$ cm. Although this grid was not used directly for this project, it provides the bottom boundary condition for future numerical models. Figure 2 shows the contour plot of the bathymetry from the grid data.

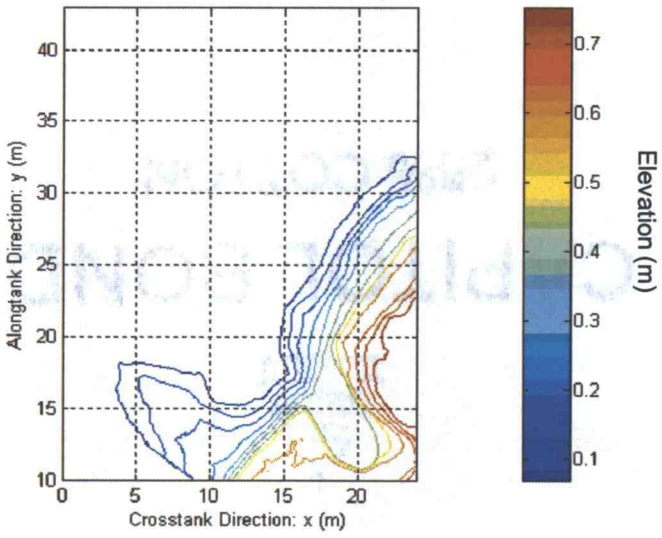

Figure 2: Contour plot of the bathymetry.

3.2 PIV technique

3.2.1 Background of PIV

As discussed earlier, PIV (Particle image velocimetry) can be used to measure laboratory flows were the film of water is thin as is the case for tsunami inundation. A commercially available system, the Flow Master 2D PIV system manufactured by LaVision, was used for this experiment. The Flow Master system includes an Imager Pro Plus 2M camera, DaVis software package, and 2D PIV software package. A detail of the system is shown in Table 1.

Table 1: Imager Pro Plus 2M camera system.

System	Description
Imager Pro Plus 2M	1648 x 1214 pixels resolution, 30frames/sec
Camera Lens	Nikon 20mm focal length, F2.8
Computer	Dual processor PC, including 2 x P4 processors (2.8 GHz), 120GB Harddisk, 17"flat screen monitor, keyboard, mouse
DaVis Software package	Version 7.0, 32-bit software for image acquisition and processing, data import/export control
2D PIV Software package	Cross- and auto correlation image processing algorithm, advanced vector post-processing

Flow in the FOV (field of view) must be seeded with tiny particles that can be traced during the image recording. The FOV is divided into small sub-areas, or interrogation window, and each window is processed using a cross correlation technique. During this process, the peak correlation is found between two consecutive images with a small time separation, and the local velocity vector is calculated. Figure 3 shows the calculation of the local vector field from a PIV recording using cross correlation.

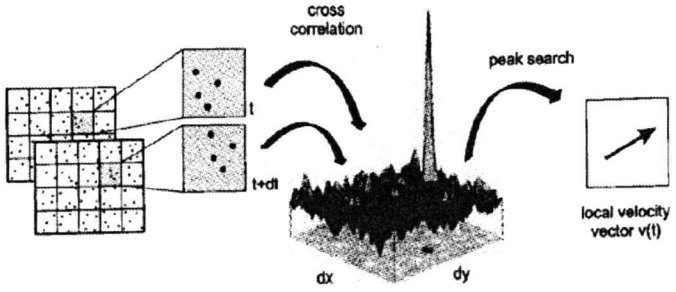

Figure 3: Schematic evaluation of a PIV recording using cross-correlation (LaVision, 2005).

3.3 Developing PIV proficiency

To obtain a better understanding about the PIV technique, a practice recording was conducted before starting the laboratory experiments. A white sheet of cardboard covered with small black dots was placed on a record player. The camera was installed on a tripod at approximately 1.5 m high from the turntable. Figure 4 shows two consecutive raw images recorded by the camera. A 30 Hz sampling rate was used for the recording. Therefore, the time separation between these two images was dt =1/30 s.

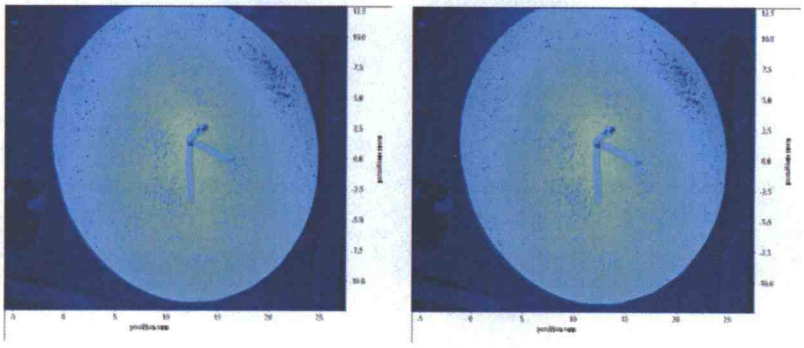

Figure 4: Two continuous images of a rotating, piece of white card-board dt=1/30 s.

The DaVis software package provided the vector field shown in Figure 5. For this process, the interrogation window was 64 x 64 pixels. Since the FOV had a 1648 x 1214 pixel resolution, there were 25 x 18 interrogation windows and a local velocity vector was calculated for each interrogation window. It is important to choose the appropriate interrogation window size. Choosing too small of an interrogation window size will result in failure to obtain correct vector fields because the allowable maximum velocity has a linear relationship with the size of the interrogation window. Choosing too big of an interrogation window size will result in having fewer vectors and more average values that may not represent the local particle velocity. Some miscalculated velocity vectors are shown in Figure 5 as white and orange vectors around the periphery. Possible causes of these errors are an insufficient number of tracers in the

interrogation window, light reflection, and interrogation window size. The horizontal and vertical axes do not show the real dimension of the picture, and thus, the magnitude of velocity was not to scale. To obtain the true dimension the actual length of the FOV is needed. Details of the image processing including vector field processing and calibration process will be discussed in Chapter 4.

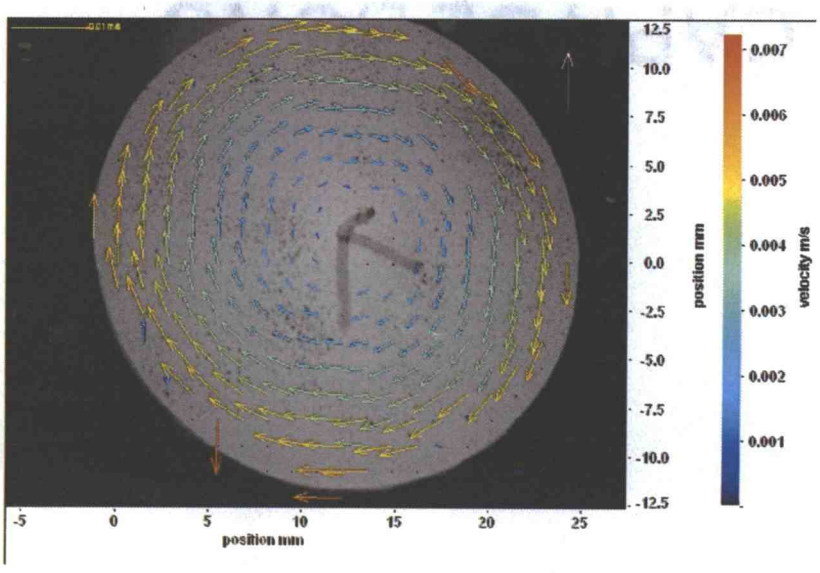

Figure 5: Vector field of rotating white board.

4. Recording procedure and image processing

4.1 General setup of experiment

4.1.1 Area of Interest

Three areas of interest on the 3D bathymetry were chosen: 1) a steep bluff, 2) low foreshore, and 3) embayment as shown in Figure 6. The steep bluff was selected because it had the steepest slope where the run-up and run-down could be observed. The embayment section had a very shallow water depth and was surrounded by an elevated coastline where turbulent bores were observed. The low foreshore section had a very mild slope and was the point of maximum inundation.

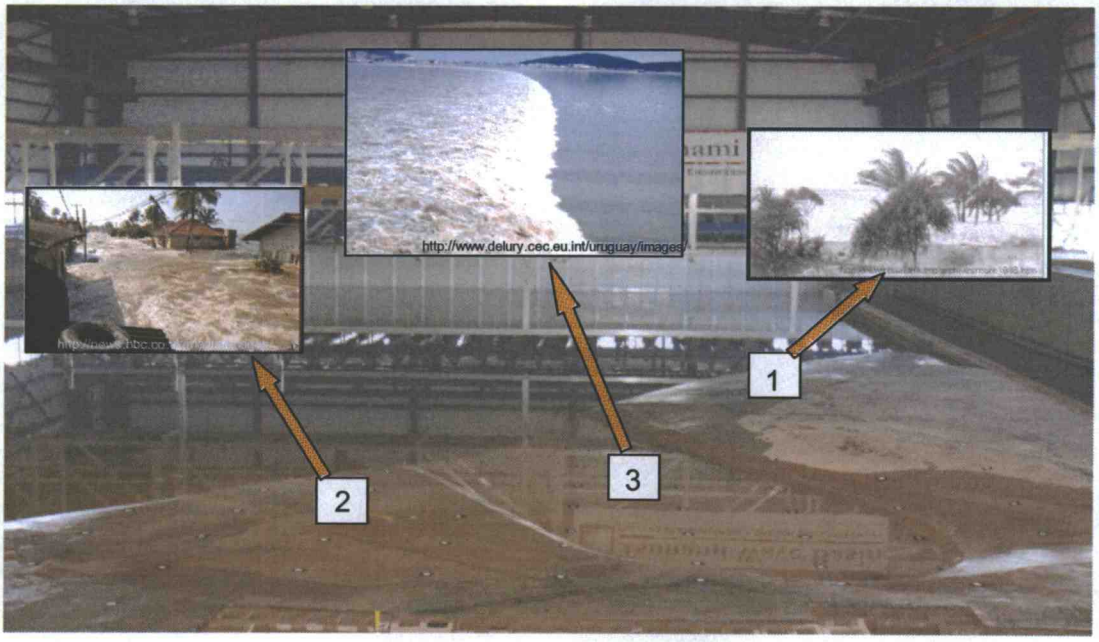

Figure 6: Three areas of interest on the model bathymetry. 1) steep bluff, 2) low foreshore, 3) embayment.

4.1.2 ADVs and wave gages

To measure the free surface velocity and the displacement, four SonTek ADV (acoustic Doppler velocimeter), and four wave gages were used. All instruments were sampled at 50 Hz. The SonTek ADVs measured water particle velocity at 8 cm vertically below the still water level at the embayment section. A measured velocity has a component in x,y and z direction, respectively. Recording in very pure water may result in failure of acquiring accurate velocity because an ADV detects small particle in water. Therefore, seeding materials were added to the water uniformly in the tank for the ADV recording. The quantity of seeding material was determined based on the SonTek ADV manual. The seeding density of 10-50 mg/l was suggested in the manual, and the volume of water in TWB was approximately 550,000 liter. Therefore, 210 kg of seeding material was used. Wave gages measured the water surface displacement by a process where the voltage fluctuation is measured across two aluminum wires that are partially submerged in the water. Water surface elevation was obtained in metric units using calibration coefficient that is the linear relationship between metric and voltage.

4.1.3 Wave cases

Previous experiments conducted in the TWB provided guidance in selecting the wave conditions. Wave cases were determined using the following criteria: conservation of mass, breaking and non-breaking waves, and run-up speed. Target wave heights were 5 cm and 25 cm in a water depth of 55 cm and 5 cm in a water depth of 44 cm water depth. The "user defined wave" was chosen to use the large stroke of the wavemaker. Table 2 lists the wave cases used in the experiment.

Table 2: Wave cases used in experiment.

Case	Target wave height (cm)	Offshore water depth; D (cm)	Average of measured wave height at offshore location, Y=32 (m); Ho (cm)
1	5	44	4.51
2	User defined	44	7.93
3	5	55	4.44
4	25	55	22.69

All target wave heights given in Table 2, except the user defined wave, were input value from the "Tsunami" menu item in wavemaker program supplied by the manufacture. The wave defined as a "Tsunami" in the wavemaker program is a solitary wave. However, it doesn't exactly represent the true tsunami characteristics due to its shorter wavelength and wave period. A tsunami in the real world, as mentioned before, has an extremely long wavelength. For example, given a wavelength of 500 km and a wave height of 1 m in the real world, the ratio of the wavelength to the wave height is 2×10^{-6}. In laboratory experiments, it would be impractical to generate such a wave. Therefore, the user defined wave was used to make a solitary wave with as long a wavelength as possible. It is generated by prescribing the wave board displacement which was set 1.62 m using the error function to determine the profile of the wave board displacement. The wave board displacement profiles for all are shown in Figure 7.

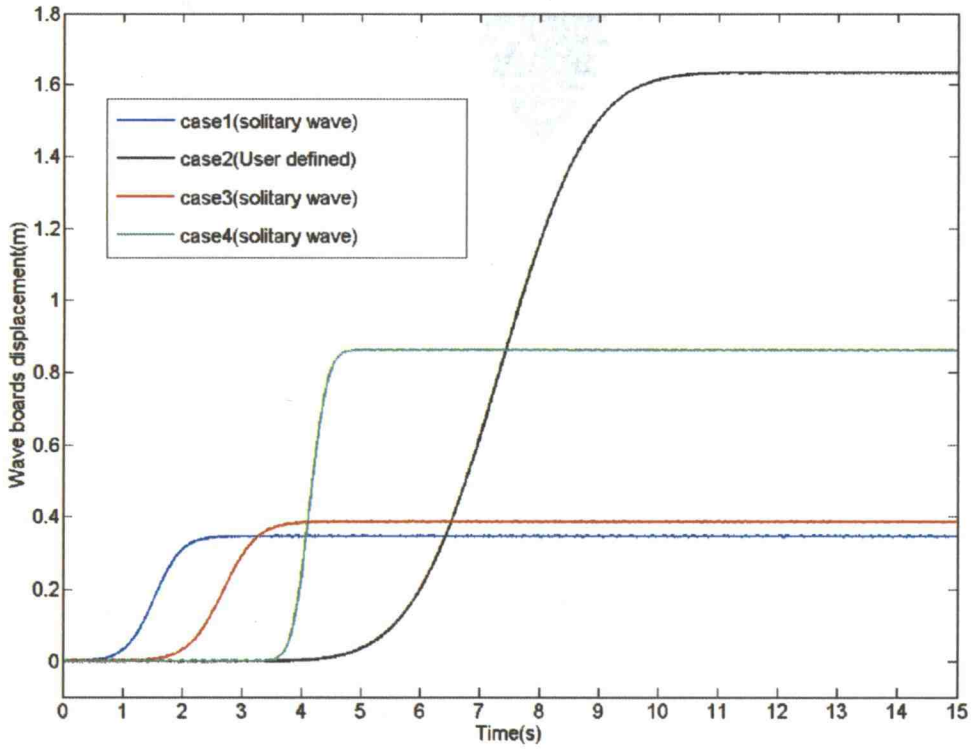

Figure 7: Wave board displacement for each case.

4.1.4 Wait time test

The wait time, or duration until the water surface calms down after running a wave, is an important quantity needed to conduct experiments efficiently and accurately. Therefore, a test was done to determine the wait time necessary before starting actual measurements. The largest wave being tested was case 4. Therefore, this time was used for all 4 cases. The sampling frequency of the ADV was 2 Hz for the wait time test, and the duration of the test was one hour. Figure 8 shows the standard deviation of the velocity for an ADV developed in deep water. The small open circles represent the standard deviation computed every 5 minutes and the small dots are every 1 minute. From Figure 8 the wait time for each case was determined to be 10 minutes.

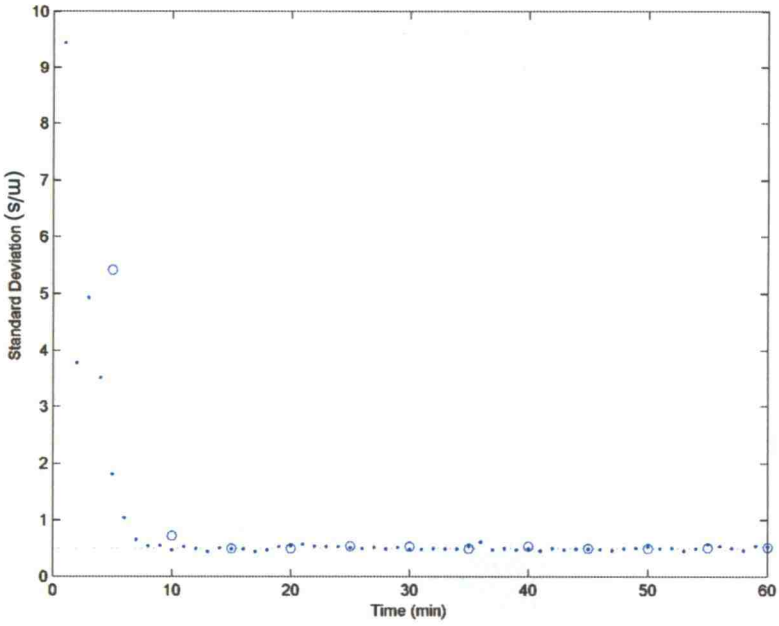

Figure 8: Plot to determine the wait time in-between wave runs.

4.1.5 Repeatability test

A repeatability test was conducted to check the accuracy of the data acquisition system and the repeatability of the wavemaker operation. The test consisted of three runs which are shown in Figure 9. The red, blue and black lines show water particle velocity in the cross tank direction (Vy) for 1st, 2nd and 3rd trial, respectively. Figure 9 (b) and (c) provide a detailed look at the maximum and minimum velocity, respectively. From these figures it is concluded that the data acquisition system is accurate and that the wavemaker produces a repeatable motion.

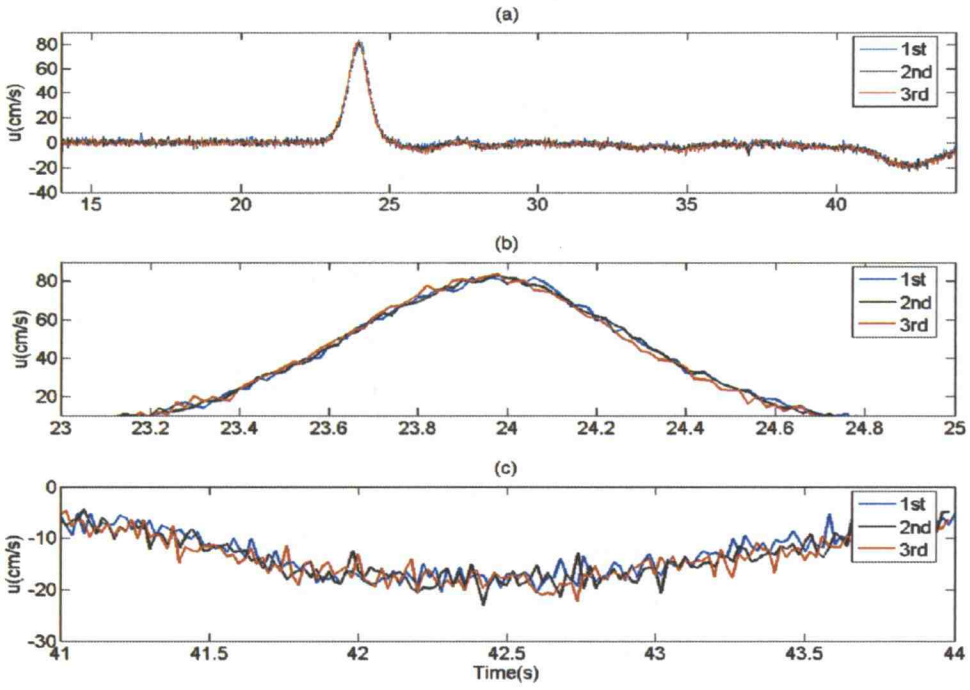

Figure 9: Repeatability test for ADV580.

4.1.6 Setup of ADV and wave gages

ADVs and wave gages were installed on a frame hung from a bridge as shown in Figure 10 and were offset slightly (0.9 cm) at each x-location. The ADVs and wave gages were sampled synchronously by triggering the ADVs to record when the wave gages started recording. The details of this process are presented in Chapter 5.

Figure 10: Setup of ADVs and wave gages on the frame.

4.2 PIV recording

4.2.1 Preliminary experiments using PIV

To obtain a better understanding of the PIV measurements including the optimal camera location and type of tracers, preliminary experiments were conducted using the setup shown in Figure 11. The camera fixed on the tripod was located on the deck of the bridge and pointed down onto the model bathymetry. The DAQ (data acquisition) system including the monitor and hard drive can be seen next to the camera. The distance between the camera and hardware was less than 5 m due to the length of the cables.

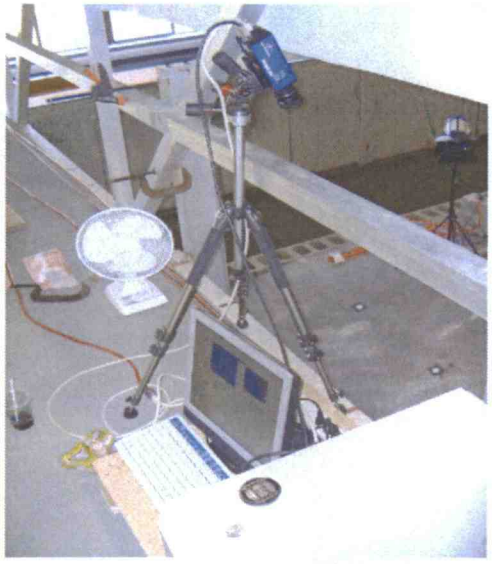

Figure 11: Camera setup on the bridge during preliminary testing.

The LaVision sales representative suggested a diameter of the tracers at least 0.5 cm and a preferable size is 1 cm or more if the distance between the camera and object is 6 m. The relationship between the height of the camera and the tracer diameter is linear. For example, if the camera is set at a distance of 4.5 m from the target, the diameter of the tracers should be at least 0.38 cm diameter and 0.75 cm or greater is preferable. Using this guidance, a few tracer types and sizes were tested using the PIV system. First, bean shaped Styrofoam with a maximum length of 1.2 cm were used. This size was large enough. However, the Styrofoam pieces typically formed several large groups when they were floating on the water surface. Figure 12(a) shows

the Styrofoam floating in water. Most of the Styrofoam is out of water and may be very sensitive to air resistance while it moves on the water surface. Due to these points the Styrofoam was determined to be an inappropriate tracer for PIV. HDPE (High Density Polyethylene) solid balls were purchased from McMASTER-CARR to be used as tracers for PIV. Four hundred HDPE solid balls with a diameter of 3/8 inch (0.95 cm) and 1750 HDPE balls with a diameter of 5/16 inch (0.79 cm) were purchased based on the available stock at that time. Both sizes were large enough according to the tracer size criterion. The specific gravity of the HDPE solid ball was 0.96, which was very similar to that of water. Figure 12(b) and (c) show the 3/8 inch and 5/16 inch diameter HDPE solid balls floating on water. Since the density of the HDPE solid ball is very similar to that of water, they float on water with the top slightly out of water. The air resistance for the HDPE solid balls is negligible and the 3/8 inch diameter is large enough for the PIV to trace it. Therefore, it was used as tracer particle. It may be desirable to use each of them without mixing. However due to the limited supply of them, it was necessary to use them at the same time.

Figure 12: Seeding materials floating in water. (a) Styrofoam (b) HDPE Solid ball 3/8 inch diameter (c) HDPE Solid ball 5/16 inch diameter.

4.2.2 Setup of instruments

The PIV camera and related components were setup on the mobile bridge in the Tsunami Wave Basin as shown in Figure 13.

Figure 13: Instrument setup on the bridge.

The camera was mounted on a tripod mount, which was attached to an I-beam. The power supply was attached to the top of the I-beam near the camera mount, as shown in Figure 14.

Figure 14: Camera and power supply attached to the I-beam.

To set up the camera, the I-beam had to be placed on top of the bridge using the over head crane. This process is shown in Figure 15(a). After placing the I-beam on the bridge, two clamps at the front of the I-beam and two clamps at the back were used to secure the I-beam to the bridge. Once in place and secure, the camera could be positioned, as shown in Figure 14(b).

Figure 15: Setup of the I-beam and camera. (a) I-beam installation on top of the bridge (b) Camera and power supply setup on the I-beam.

The DAQ for PIV including the hardware, monitor, and keyboard were set on a wood pallet as shown in Figure 16. The maximum cord length between the camera and the hardware was 5 m and the length of the I-beam jutting out from the edge of bridge was approximately 2 m. Therfore the PIV DAQ was moved when the camera location was changed due to the short cord lengths.

Figure 16: DAQ for PIV

The DAQ for the wave gage and a LED (Light-emitting diode) was located on a table at the center of the bridge, as shown in Figure 17. The small blue box with a red button is the switch for the LED. The DAQ acquired three signals: the wave gage at the wavemaker, the displacement of one of the wave boards, and the LED signal. The signals acquired on this DAQ are shown in Chapter 4.3.3

Figure 17: DAQ for wave gage and LED.

The LED was set on the edge of a white wooden bar as shown Figure 18. The location of the LED was chosen to be in the FOV of the camera and it was turned on and off manually by the switch shown in Figure 17. The LED signal was used to synchronize the PIV data with ADV data. Details are presented in Chapter 4.3.3.

Figure 18: LED installed on the wood bar.

4.2.3 Image calibration

To estimate the true velocity vector field, the images were calibrated to relate the image coordinate system to the real world and to remove bias from the camera setup. Therefore, the calibration process was needed to revise the error in the camera image. A grid was painted on each area of interest to provide a real-world reference to calibrate the images.

Figure 19 shows the grid painted on the steep bluff section of the bathymetry. Other sections are shown in the Appendix A. Large white dots of 5 cm diameter were painted on a 1m x 1m grid and small dots of 2.5 cm diameter were on a 20 cm x 20 cm grid. To provide good contrast, the 5 cm diameter white dots were painted over 10 cm x 10 cm black squares and the 2.5 cm diameter white dots were painted over 5 cm x 5 cm black squares. Only the small 2.5 cm diameter dots were used to calibrate the image calibration because the DaVis Software manual suggests that at least 20 to 100 reference points should be distributed over the complete FOV. For example, the FOV on the steep bluff section was 1.957 m x 2.679 m and it included 90-100 small dots which is greater than the number specified by the DaVis software. It is noted that Figure 19 was taken at an oblique angle to orient the observer on the bathymetry. The FOV of the PIV images were taken essentially directly overhead to minimize distortion.

Figure 19: Dots for calibration of image at the steep bluff.

It worth noting that since the bathymetry was not flat, the distance between the dots was measured in the x-y plane, not along the bathymetry. This was done by using two, level rulers, one to measure the liner distance parallel to the flat bottom and another perpendicular to the bottom to mark the position of the dot.

It is important to note that the camera used in the experiment is a 2D PIV camera and it allowed for either a 1D or a 2D calibration, but not a 3D calibration. Because the image is 2D, the calibrated image has no depth component and the bathymetry was regarded as a flat plate parallel to the flat bottom of the basin. The procedure for calibration was as follows.

1. In the calibration window of the DaVis software package, define the experimental setup by choosing "2D type calibration".
2. Define the coordinate system by choosing "right hand coordinate".
3. Under "Select used calibrated plate", choose the calibrated plate as "2D" and mark types are "dots". Also input the mark size and the distance between each mark as 2.5 cm and 20 cm, respectively.

4. Under "Image acquisition", take a base image for calibration (example shown in Figure 20). The recording after calibration should be conducted with exactly the same FOV as this image. In other words, the PIV recording at the other FOV needs new calibration according to the new image.

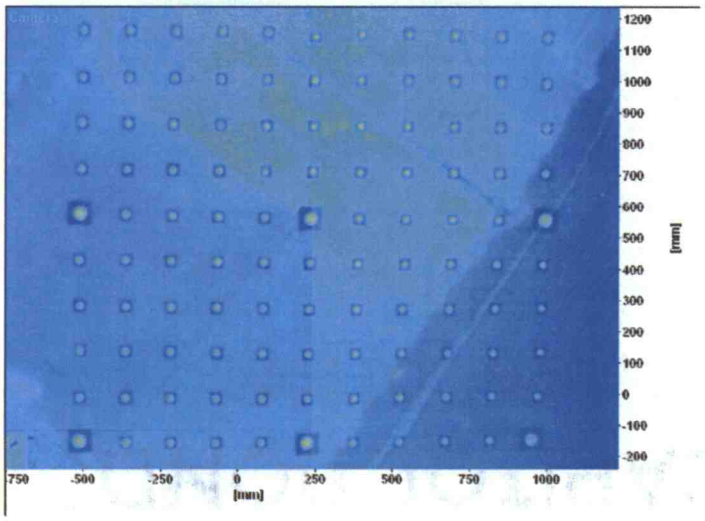

Figure 20: Example of an image to calibrate.

5. Under "Mark definition", choose 3 marks from the image that will be used to calibrate the whole image. The first mark will be the origin of the calibrated image.
6. The other marks will be found automatically according to the 3 marks defined in previous procedure and are shown as small green dots on the image as shown in Figure 21. After the marks are detected the user must check for any miss-detected marks. These were typically marked on the bathymetry or the larger 5 cm diameter marks. Including mis-detected marks in the calibration process will lower the accuracy of the calibration.

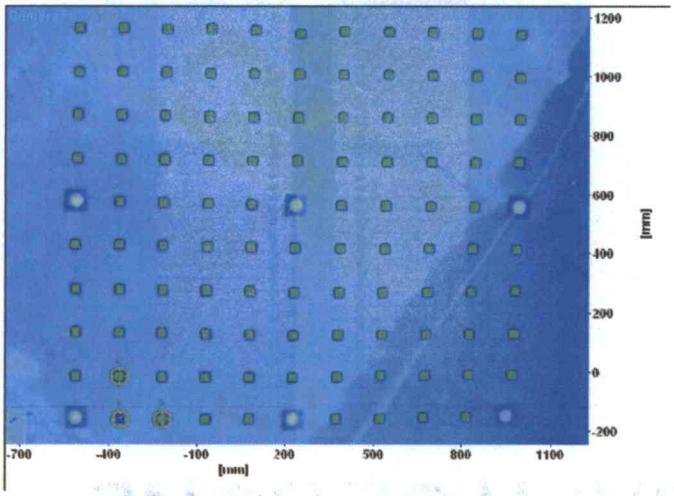

Figure 21: Marks found using the calibration software (green squares).

7. Finally, the calibrated image is displayed as shown in Figure 22. After the image calibration is complete, save the results. The calibration function will be applied to all recordings in the directory of the calibration file.

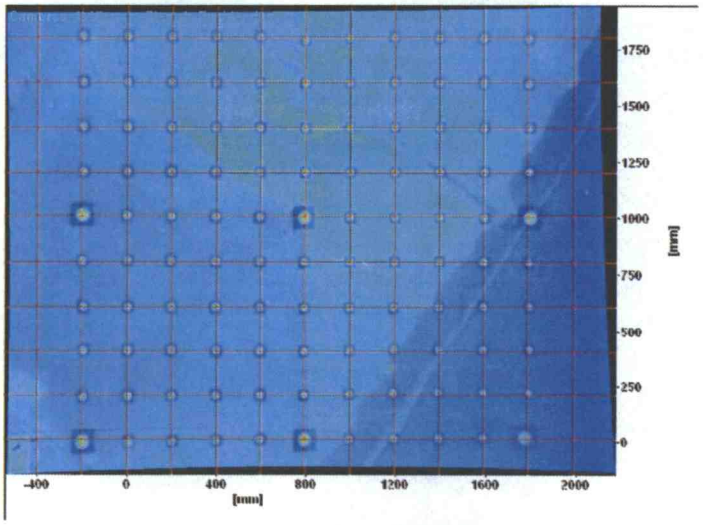

Figure 22: Calibrated image.

4.2.4 Lighting

Proper lighting is one of the most important components in PIV recording. A typical small-scale laboratory PIV setup uses a light sheet that is formed by double pulsed laser beams to illuminate tracer particles. The double pulse laser is used for two purposes: to establish a small sampling rate and to provide the contrast necessary to identify the tracers.

In this experiment a light sheet was not used. Therefore, one concern was the illumination of the tracers. To obtain a better understanding of the effect lighting plays in the image, an experiment was conducted using a spotlight to illuminate the FOV as shown in Figure 23. On the steep bluff, PIV recording was conducted with the spotlight on and with it off. The netting shown in Figure 23 was used to prevent the tracers from drifting away during preliminary tests and was not used for the final tests.

Figure 23: Setup for light effect test. The spotlight was used to illuminate the FOV and the netting was used to prevent the tracers from drifting away.

Figure 24(a) and 24(b) show a raw image taken by the camera deployed on the top of the bridge without using the spotlight and the corresponding vector field, respectively. Figure 24(c) and 24(d) show a raw image taken by camera with the spotlight and the corresponding vector field, respectively. Comparing these two figures, one can see that the spotlight provides uniform lighting in the center of the FOV, but it is not uniform over the entire image (Figure 24(c)).

Comparing the vector fields, one can see that the image without the spotlight was the better of the two. Even though these vector fields were generated using a different number of tracers, the comparison is useful to get an idea of the effect of light on the image. As previously shown, there were more vectors without the spotlight and fewer erroneous vectors. These differences may be caused by the difference in the uniformity of the lighting within the FOV. Based on these comparisons, no spotlight was used for this experiment.

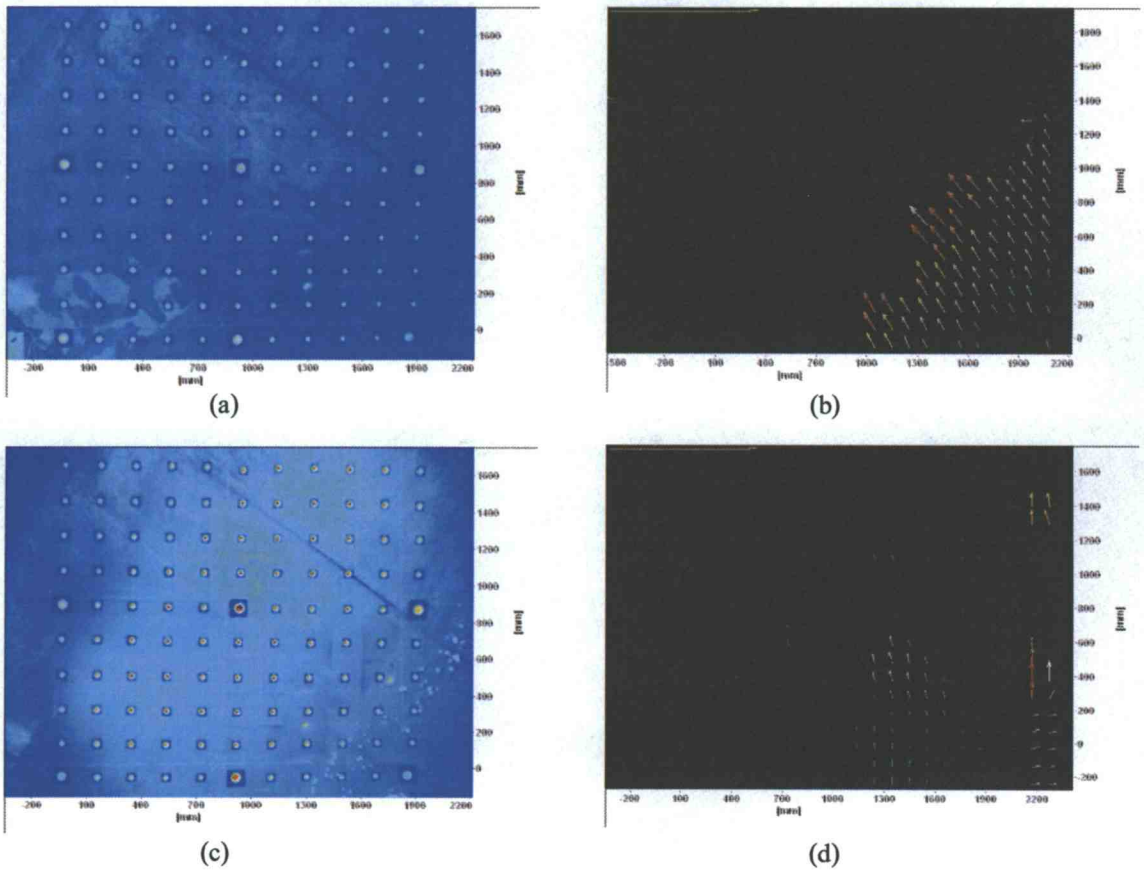

Figure 24: Raw image and corresponding vector field for (a) FOV without spot light, (b) Sample vector field from (a), (c) FOV with spotlight , (d) Sample vector field from (c).

There was also light contamination from the overhead lights in the TWB (Figure 25(a)), so they were turned off during testing. Plastic sheeting (Figure 25(b)) was placed over the

verification in the roof of the basin to prevent ambient lighting from contaminating the image as well.

(a) (b)

Figure 25: (a) Overhead lights in the TWB. (b) Plastic sheeting placed over the roof vents.

4.2.5 Method used to add tracers to the FOV

To obtain an appropriate vector field from the convective images, tracer particles were placed on the water surface and the dry beach prior to each test. Additionally, tracers were distributed manually in the FOV as the wave passed by to increase the local tracer density, especially in the trough of the wave. Figure 26(a) shows the tracers ready to be distributed onto the water surface as the wave passes and Figure 26(b) shows the dustpan used to carry this out. Typically, half of the tracers were added prior to the test and the remaining half were added as the wave passed by. The tracer density was an important factor in the quality of the data. Therefore, tracers were added in such a way that the tracer density was as uniform as possible.

(a) (b)

Figure 26: Addition of tracer particles to the FOV. (a) Student ready to add tracers as the wave passes, (b) Dust pan used to add tracers.

4.3 Recording procedure

4.3.1 Field of view and test cases

As previously mentioned, the experiment was conducted at three areas of interest: the steep bluff, embayment, and low foreshore sections. In Figure 27, blue, red and black dots represent the 1 m x 1 m grid painted at the steep bluff, embayment, and low foreshore sections, respectively. Contours represent the elevation measured from the floor of the basin.

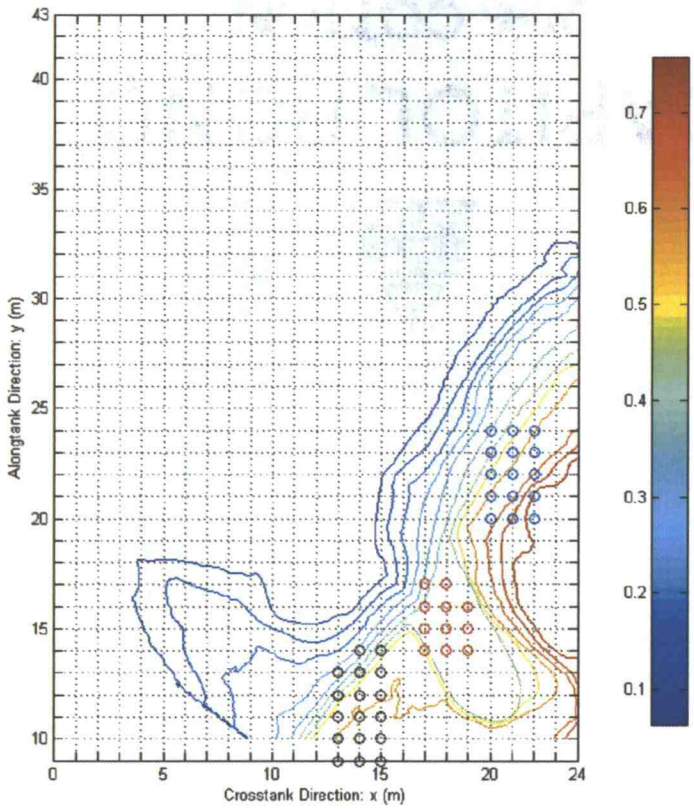

Figure 27: Complete test grid for PIV testing. Contours are measured from the basin floor. Circles represent the 1 m x 1 m grid painted on the bathymetry. Blue, red, and black circles correspond to the steep bluff, embayment, and low foreshore sections, respectively.

The FOV was determined based on the number of grid dots within the FOV (dots used to calibrate the image) with a given camera location. For example, Figure 28 shows the detailed PIV grid painted on the bathymetry at the steep bluff section. The large blue dots represent the white dots with a diameter of 5 cm, and the small blue dots represent white dots with a diameter of 2.5 cm. With the camera mounted on top of the bridge, the FOV was approximately 2.0 m in the cross-tank direction and 2.6 m in the along-tank direction, which covered the painted grid in the along-tank direction and approximately half of the grid in the cross-tank direction. In some cases multiple camera positions were used at a single location to capture the inundation event. The boundaries of the FOVs used for this experiment are listed in Table 3.

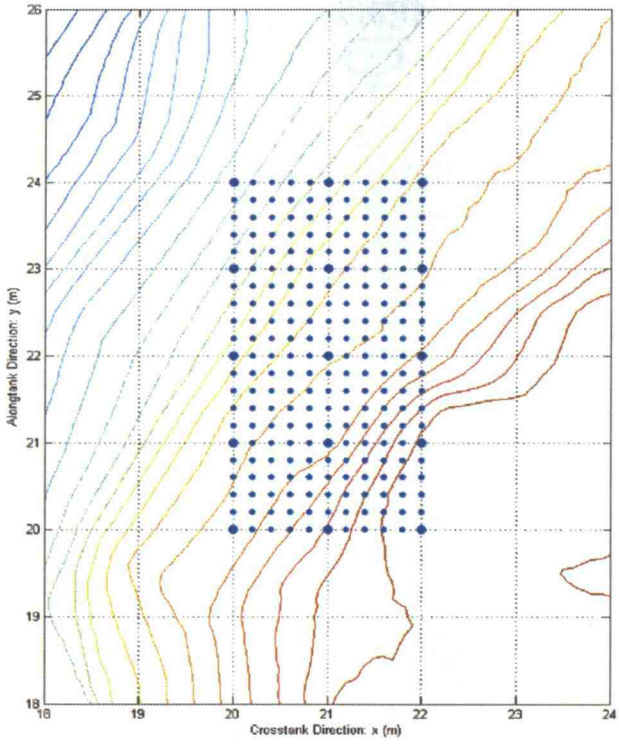

Figure 28: Location of the grid painted on the steep bluff section along with contours of the bathymetry measured from the basin floor.

Table 3: FOV boundaries for each area of interest.

Area Of Interest	FOV	Location (X(m), Y(m))
Steep bluff	S-1	X=20-22, Y=22-24
	S-2	X=20-22, Y=21-23
	S-3	X=20-22, Y=20-22
Embayment	E-1	X=17-19, Y=15-17
	E-2	X=17-19, Y=14-16
Low foreshore	L-1	X=13-15, Y=11-13
	L-2	X=13-15, Y=10-12
	L-3	X=13-15, Y=9-11

Table 4 delineates the test number, area of interest (AOI), water depth, field of view (FOV), and target wave height for each test conducted as part of this experiment. From this point on, the test number will be used to describe the test conditions. The maximum inundation levels for the tests are briefly sketched in Appendix B.

Table 4: Test cases for PIV.

Test	AOI	Water depth,D (cm)	FOV	Target wave height (cm)
1	Steep bluff	44.0	S-1	5.0
2	Steep bluff	44.0	S-1	User defined
3	Steep bluff	44.0	S-2	User defined
4	Steep bluff	44.0	S-3	User defined
5	Steep bluff	55.0	S-1	25.0
6	Steep bluff	55.0	S-2	5.0
7	Steep bluff	55.0	S-3	5.0
8	Low foreshore	44.0	L-1	5.0
9	Low foreshore	44.0	L-1	User defined
10	Low foreshore	44.0	L-3	User defined
11	Low foreshore	55.0	L-2	5.0
12	Low foreshore	55.0	L-3	5.0
13	Low foreshore	55.0	L-3	25.0
14	Embayment	44.0	E-1	5.0
15	Embayment	44.0	E-1	User defined
16	Embayment	44.0	E-2	5.0
17	Embayment	44.0	E-2	User defined
18	Embayment	55.0	E-1	5.0
19	Embayment	55.0	E-1	25.0
20	Embayment	55.0	E-2	5.0

4.3.2 Recording procedure

The following procedure was used for the PIV recording:

(1) Setup the camera on the bridge

The I-beam was installed on top of the bridge such that the cross tank location was equal to the center of the AOI (e.g. x = 21 m for the steep bluff section). The camera was deployed on the I-beam as described in Chapter 4.3.2. Care was taken to orient the camera perpendicular to the target.

(2) Calibrated the image

After the FOV was selected, the calibration procedure described in Chapter 4.3.3 was conducted.

(3) Prepared to collect the PIV data

At least four people were needed for the PIV recording: one to run the wavemaker, one to run the DAQ for the wave gages and LED, one to run the DAQ for the PIV, and one to add tracers to the FOV as the wave passed by.

(4) Turned on the LED

The LED signal was turned on by hand to synchronize the time series recorded by the PIV camera with the time series recorded by the rest of the instrumentation (e.g. wave gages and ADVs). The details of the synchronization are described in Chapter 4.3.3. The LED produced an output signal of 3.5 V when turned on and 0 V when turned off.

(5) Started the DAQ for the wave gages and LED

Beginning from a still water condition (no water motion in the basin), the DAQ for the wave gages and LED was started with a recording time of 2 minutes at a sampling rate of 30 Hz (PIV DAQ was also set to sample at 30 Hz).

(6) Started the wavemaker

The wavemaker was started using the wavemaker control system with the appropriate input conditions.

(7) Started the DAQ for the PIV recording

The recording time for the PIV was up to 11 seconds (314 consecutive images sampled at 30 Hz). Therefore, care was taken to determine the start of the PIV DAQ to capture the entire event. This was done by observing the wave propagation and starting the DAQ by hand. In some cases 11 s was not enough time to capture the whole event, so multiple recordings were collected at that location.

(8) Turned off the LED

Shortly after the DAQ for the PIV was started, the LED was turned off. The change in the LED signal was recorded on both the DAQ systems (wave gage DAQ recorded a drop from 3.5 V to 0 V and the PIV DAQ recorded the visual signal of the LED turning off). Only the images recorded after the LED was turned off were used in the PIV analysis. This sequence was used because the PIV camera focuses on the LED when it is illuminated instead of the tracer particles.

(9) Added tracers to the water surface

Prior to starting the wavemaker, tracers were added to the surface of the water and the dry beach. Additionally, tracers were sprinkled on the free surface as the wave propagated past the instrument frame. It was difficult to achieve a uniform distribution of tracers within the FOV, so this process was repeated until it was confirmed that the tracers were distributed uniformly within the FOV.

(10) Collected tracer particles

Upon completion of the test all of the tracer particles were collected using a pool cleaning net, which is shown in Figure 29(a). Some of the tracers stuck together when they were floating on the surface of the water so a small amount of liquid detergent, shown in Figure 29(b), was applied to the tracers.

(a) (b)

Figure 29: Useful tools (a) Pool cleaning net, (b) Detergent used to prevent tracers from sticking together.

(11) Waited for the water to return to rest

After each test, it took 10 minutes to allow the water in the basin to settle. This time was determined from the repeatability test.

4.3.3 Image processing

After the tests were run, the images were processed using the DaVis Software to acquire the velocity vector field. This chapter describes this process in detail using data from the steep bluff section as an example.

(1) Verified that the correct calibration file was in the file folder

In the "properties" dialog box (Figure 30), it was verified that the raw image was calibrated properly.

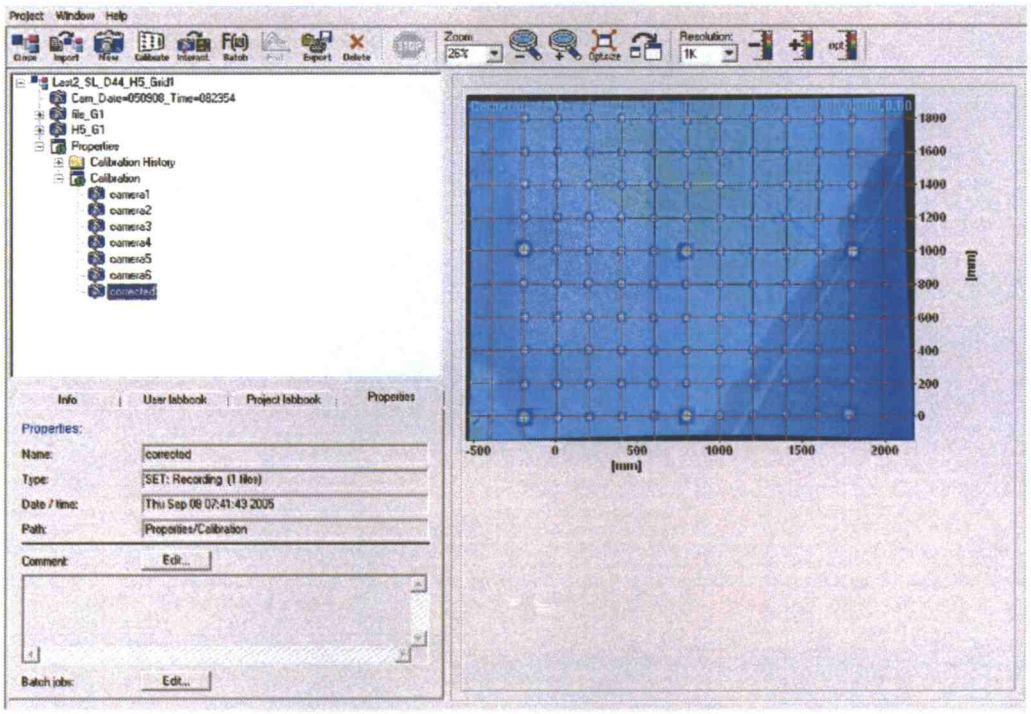

Figure 30: Properties dialog box.

(2) Checked the quality of the raw images

Figure 31 shows 4 images selected from a total of 341 images (11 seconds), and the letter i represents the index number of an image.

First, the image corresponding to i=1 was dark as expected due to the illuminated LED (bottom left hand side of the FOV) as shown in Figure 31(a). As mentioned above, the camera adjusted the resolution of each image based on the brightness of the image. The LED was much brighter than the rest of the image; therefore, it was clearly shown while the remainder of the image was dark.

Second, the image where the LED was turned off was located. For the recording shown in Figure 31 this transition occurred between images i=53 and i=54 (Figure 31(b) - (c)). The transition point always occurred between two images (i.e. the transition time was less than 1/30 seconds).

Third, it was verified that the water particles were not in motion at the transition point (i=54 shown in Figure 31(c)). Essentially, this verified that the LED was turned off before the water particles began to move.

Fourth, because the DAQ could only record up to 341 images (11.37 s at 30 Hz) it was verified that the record length was sufficient to capture the entire inundation event. In the event that this record length was not sufficient, two or more experiments were conducted and synchronized in post-processing using the LED and wave gage time series.

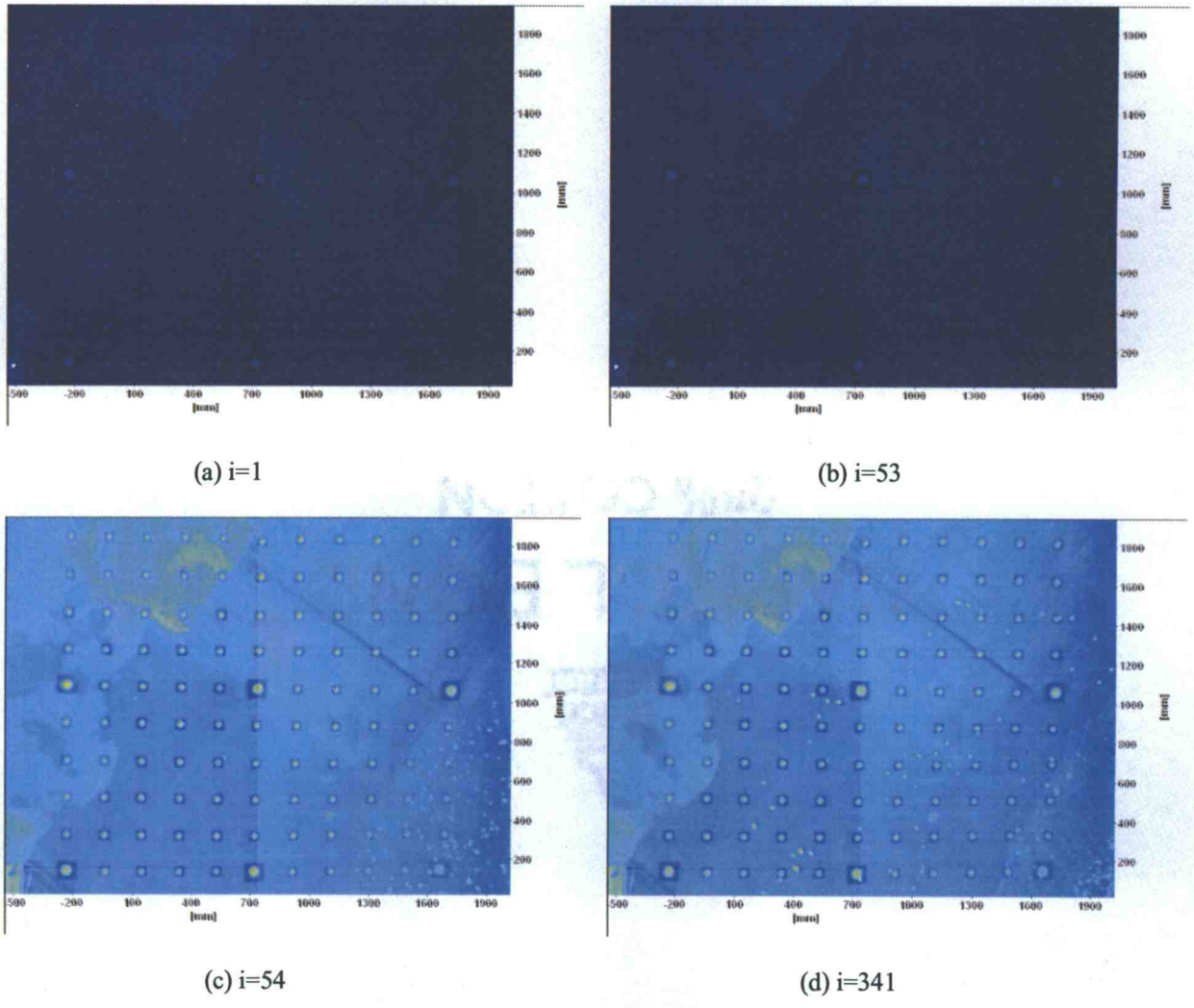

(a) i=1

(b) i=53

(c) i=54

(d) i=341

Figure 31: Raw images from a PIV recording on the steep bluff section.

(3) Calibration of all images

Before calculating the velocity vector field from the images they must be converted into calibrated or corrected images. This calibration was conducted using the "Batch process" window in the DaVis software package (Figure 32). In the "Operation list", "image correction (raw -> world)" was selected and was applied to all 341 images.

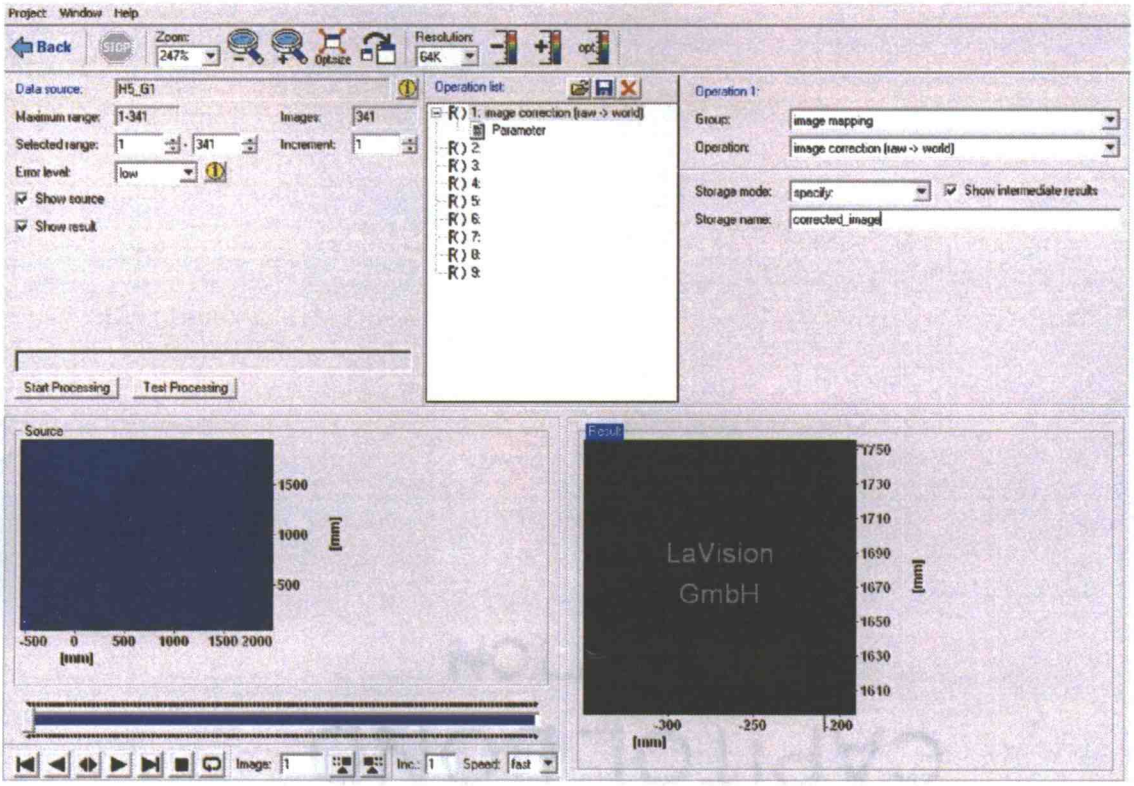

Figure 32: Image correction using the "Batch process" window.

After the images were corrected, the continuous image stream was checked using the window shown in Figure 30. The corrected images, shown in Figure 33, were saved in the same file folder as the raw images. In Figure 33(c) and (d) some black space can be seen around the edges of the FOV and was typical for all of the corrected images.

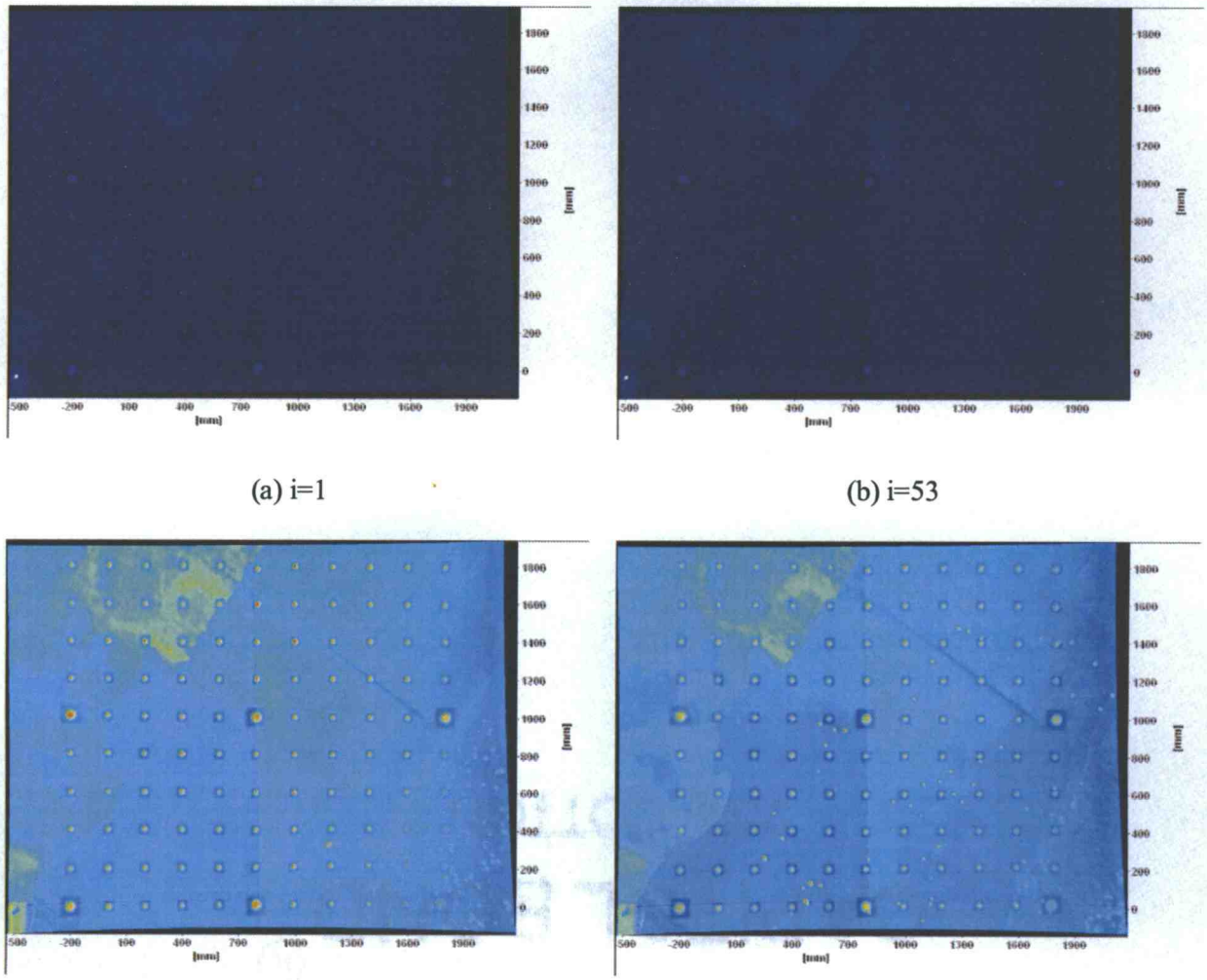

(a) i=1 (b) i=53

(c) i=54 (d) i=341

Figure 33: Corrected images from a PIV recording on the steep bluff section.

(4) Computation of the velocity vector field

The velocity vector field was computed from the corrected images using the "Batch process" window in the DaVis software package. Under the "Operation list", "PIV Time-series cross correlation" was selected (see Figure 34) to calculate the velocity vectors. Under the sub-operation "Vector calculation parameter", an appropriate interrogation window size and overlap coefficient was selected.

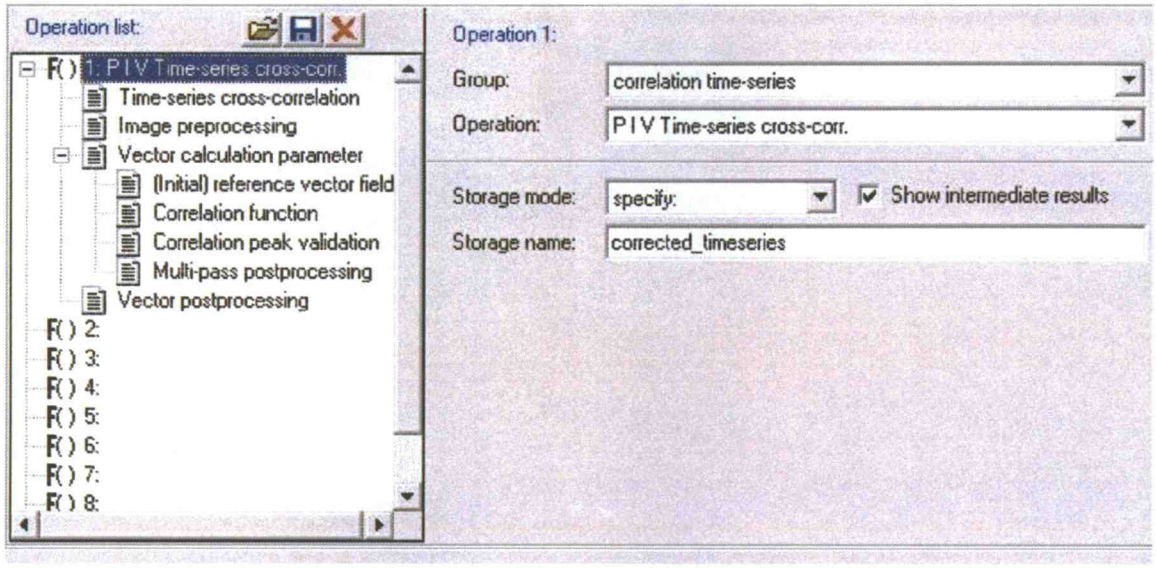

Figure 34: PIV time series dialog box used to calculate the velocity vector field.

Selecting an appropriate interrogation window size was important when calculating the vector field. The allowable interrogation window size ranged from 4 x 4 to 1024 x 1024 pixels (the whole image had a resolution of 1600 x 1200 pixels). For example, choosing 64 x 64 pixels for the interrogation window size, the image would be divided into (1600/64) x (1200/64) = 469 sub squares where 469 velocity vectors will appear.

The number of pixels in the FOV was fixed based on the resolution of the camera (1600 x 1200 pixels). This resolution was not changed based on the distance from the camera to the object or the camera angle; however, these geometric factors did affect the physical dimensions of the image. For example, the physical dimensions of an image became smaller as the camera was moved closer to the object, while the resolution of the image did not change. The physical dimensions of each image were determined from the image calibration process described above. For example, the dimensions of the FOV on the steep bluff section were approximately 2.6 m x 2.0 m with a fixed image resolution of 1600 x 1200 pixels. Therefore, 1 pixel corresponded to 2.6 m / 1600 pixels = 1.6 mm/pixel. If the interrogation window size was 64 x 64 pixels, then the

physical dimensions of the interrogation window were 10.4 cm x 10.4 cm.

The maximum allowable velocity within each interrogation window is given to be

$$V_A = \frac{1}{3} Lf \tag{4.1}$$

where V_A is the maximum allowable velocity in an interrogation window, L is the length of one side of an interrogation window, and f is the sampling rate in Hz. For example, the maximum allowable velocity for this case was

$1/3 \times 0.104\ m \times 30\ (1/s) = 1.04\ m/s$.

In this case, if the water particle velocity in the FOV was larger than 1.04 m/s then the interrogation window size of 10.4 cm x 10.4 cm would not be big enough to accurately calculate the velocity. Possible solutions would be to move the camera away from the object or select a larger interrogation window size. It is likely that increasing the interrogation window size would be the easiest way to solve the problem. However, this means that the number of velocity vectors within the image would decrease.

The number of vectors that were calculated within an image could then be increased by using the "Overlap function" under the "Vector calculation parameter" in the operation list. The overlap function overlaps each interrogation window with its neighbors as shown in Figure 35.

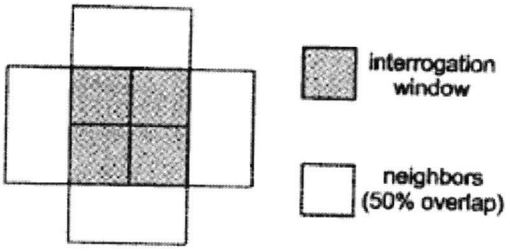

Figure 35: Example of a 50% overlap on the interrogation window (LaVision, 2005).

For example, using an interrogation window size of 128 x 128 pixels and 0% overlap on an image with 1600 x 1200 pixels yields 13 x 9 windows with a total of 117 vectors. The same parameters with a 50% overlap yields 25 x 18 windows with a total of 450 vectors.

(5) Post processed the vector fields

The calculated vector fields were post processed to remove erroneous vectors using several filters available in the "Vector post processing" window shown in Figure 36.

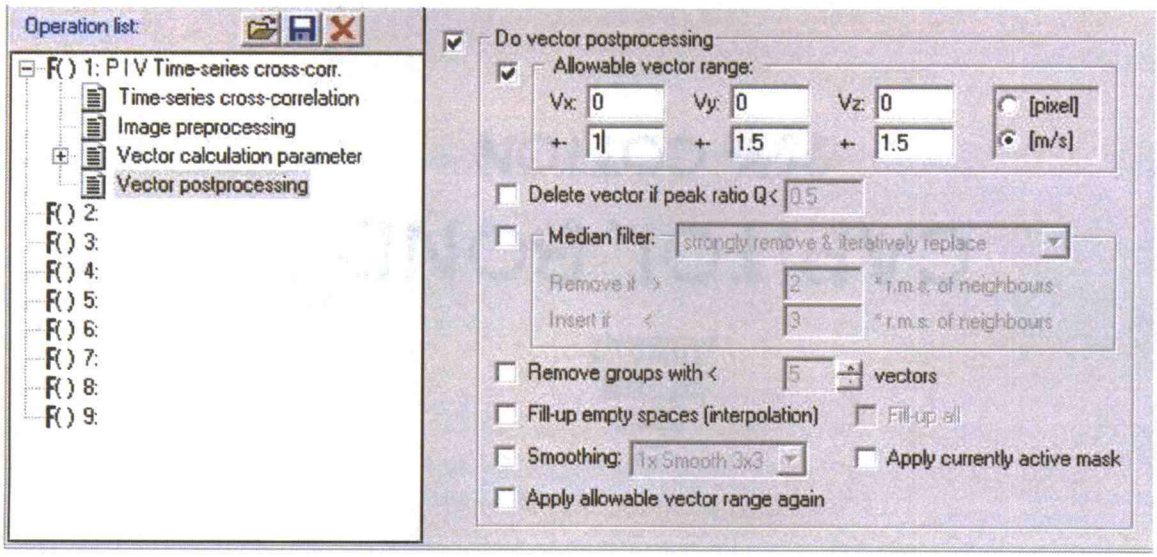

Figure 36: Vector post processing window.

(5-1) Allowable vector range

One method to reduce the number of erroneous vectors is to set an allowable velocity range for the flow field. These values can be input in either m/s or pixels for each component of the velocity (i.e. x, y, and z directions). For example, some obvious errors were shown in Figure 5 for the record player example.

(5-2) Median filter

The median filter computes the median velocity vector from 8 neighboring vectors (Figure 37) and checks that each velocity vector satisfies the criteria given below

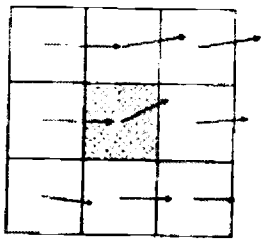

Figure 37: Local median filter (LaVision, 2005).

Criteria for the median filter are:

$$U_{median} - U_{rms} \le U \le U_{median} + U_{rms}$$
$$V_{median} - V_{rms} \le V \le V_{median} + V_{rms} \quad (4.2)$$

where $U_{meadian}$ = median value of the U component of velocity in the entire flow field,

V_{median} = median value of the V component of velocity in the entire flow field

U_{rms} = standard deviation of the U component of velocity from the neighboring vectors,

V_{rms} = standard deviation of the V components of velocity from the neighboring vectors.

And the standard deviation is defined as,

$$U_{rms} = \sqrt{\frac{1}{N-1}\sum_{i=1}^{N}(U_i - U_{median})^2} \quad (4.3)$$

(5-3) Fill-up empty space

The "Fill-up empty space" function can be used to fill the empty space within the flow field with interpolated velocity vectors. This function can be very useful when calculating quantities such as the vorticity and divergence, which rely on derivatives that are very sensitive to missing data. This function is not recommended unless the interpolated vectors seem to be reliable. Therefore, it is important to compare each image before and after the interpolation. This function was not used to post process the vector fields in this experiment to avoid the possibility of poorly interpolating the vectors.

(5-4) Smooth 3 x 3

The "Smooth 3 x 3" function can be used to smooth the final vector field to reduce noise in the flow field. If the "Smooth 3 x 3" function is applied to empty space within the flow field, all non zero neighbors will be averaged and the mean value will be placed in the empty space. This function is also useful when calculating derivatives of vector fields. However, this function was not applied to the vector fields during post-processing

In general the "fill-up empty space" and "smooth 3 x 3" functions are very useful for sparse vector fields. However, they were not applied to this experiment because the quantities involving derivatives of the velocity vector field was not needed. The "median filter" function was not appropriate for the vector field in this experiment because the vectors in the FOV were relatively sparse. Therefore, only the "allowable vector range" function was applied to post-process the vector field.

(6) Calculated the Vector field

Using the process presented above, the vector fields from the PIV recording were calculated. Figure 38 shows an example of the vector field computed for case 1 at FOV S-1 on the steep bluff.

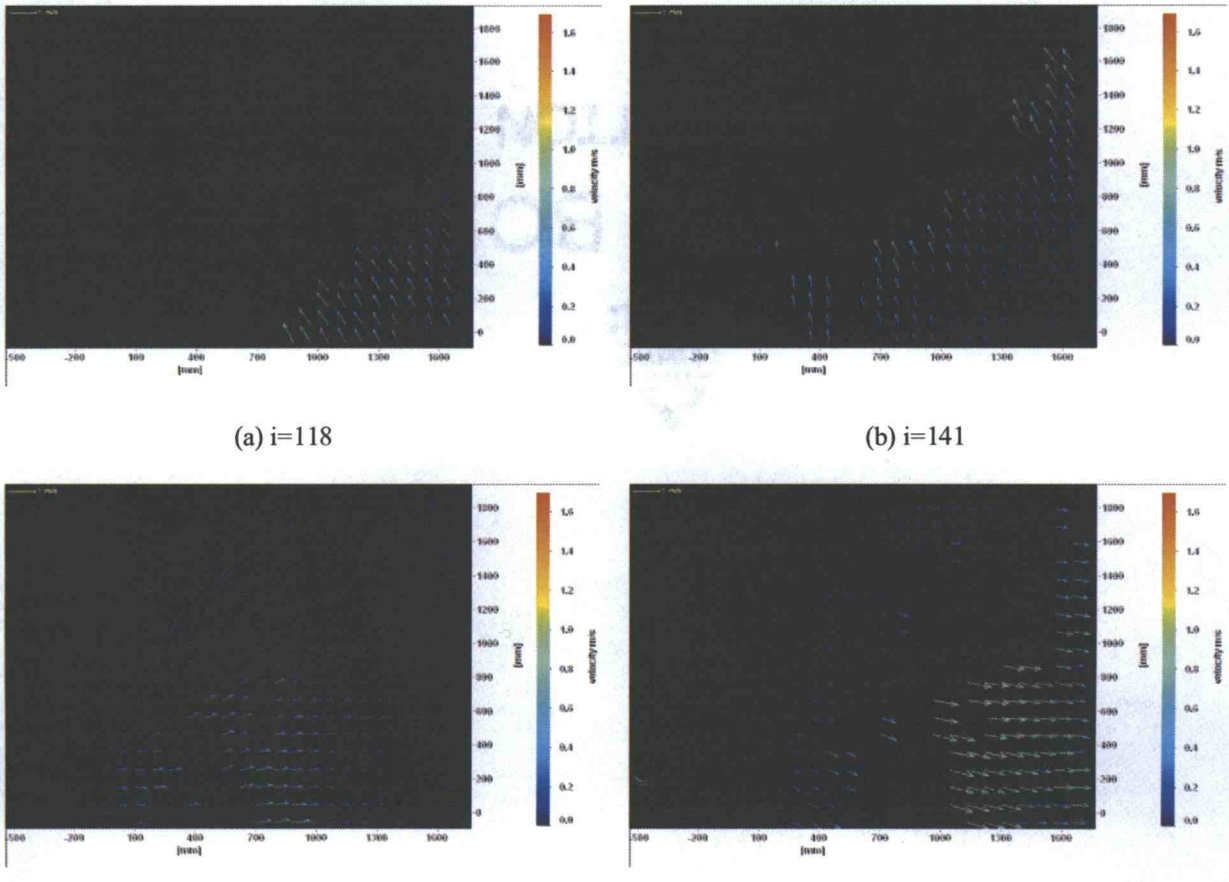

(a) i=118 (b) i=141

(c) i=170 (d) i=193

Figure 38: Vector field calculated from the PIV images on the steep bluff section.

(7) Overlaid the vector field onto the image

Finally, the vector field was overlaid onto the actual image recorded by the PIV camera as follows. The "Data and display properties" window was opened from the "Export" dialog. In the "Data and display properties" window, "Vector Background Raw Image" was selected and "Blending mode" was set to "raw image" as shown in Figure 39.

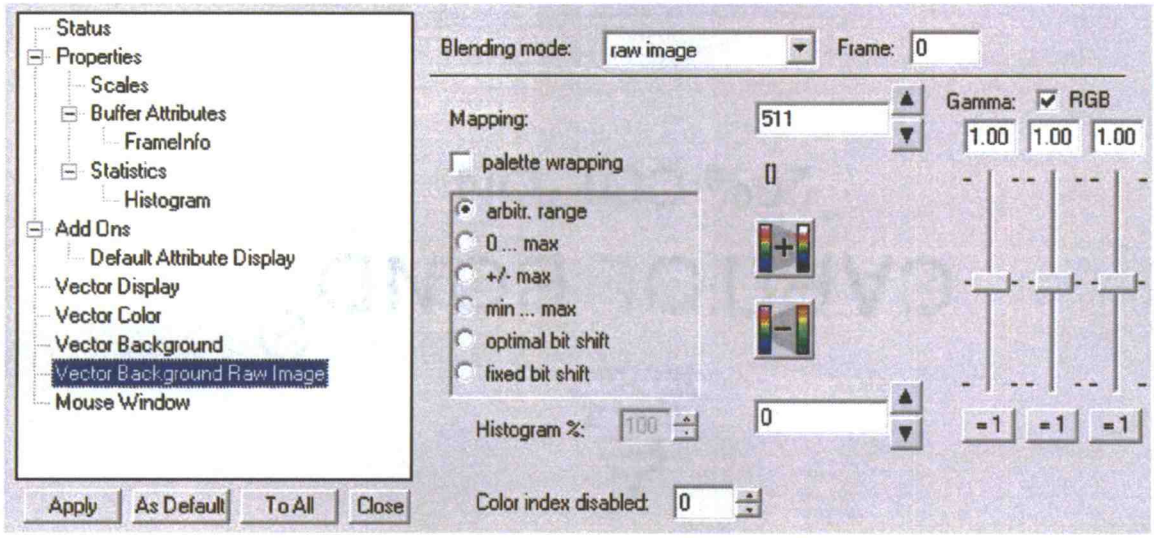

Figure 39: Dialog box used to overlay the vector field onto the original image.

The color bar was also added to the figure by using the "Add Ons" function in the "Data and display properties" shown in Figure 40.

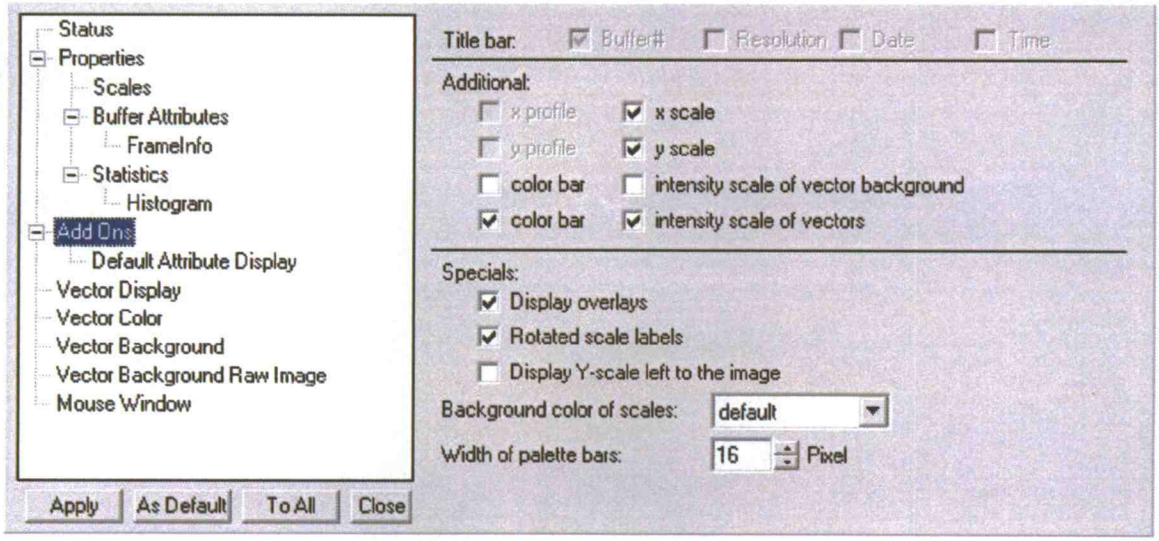

Figure 40: Setting color bar and label.

The length and size of the vectors displayed on the image could then be changed by setting "Display Grid Factor" and "Vector Length". A reference vector could also be added by selecting "Show Reference" shown in Figure 41.

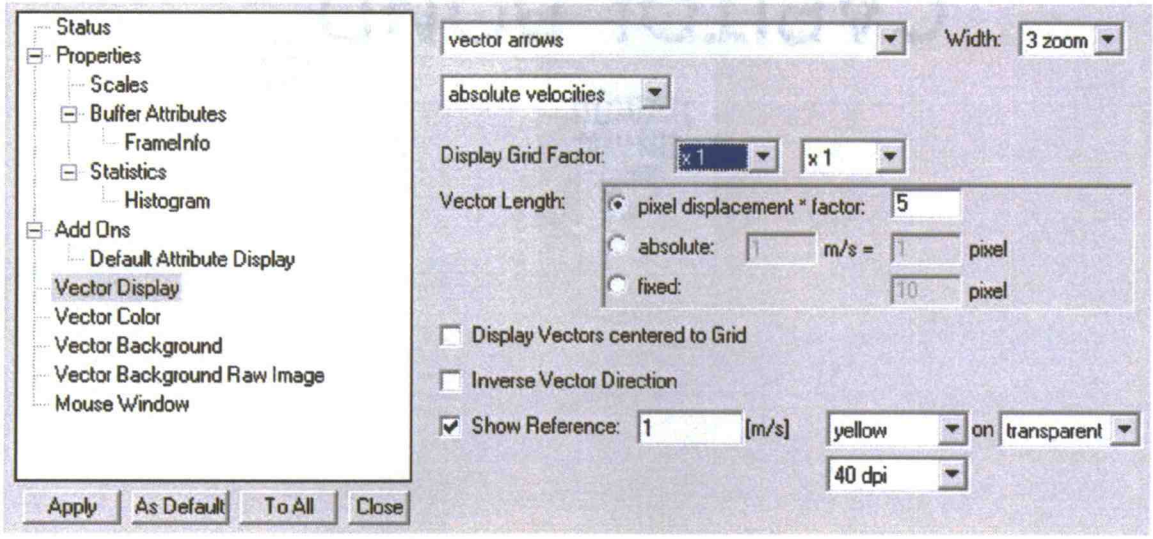

Figure 41: Setting vector size and reference vector.

Figure 42 shows the final results of vector field overlaid on the background image using the same index numbers that were used in Figure 38.

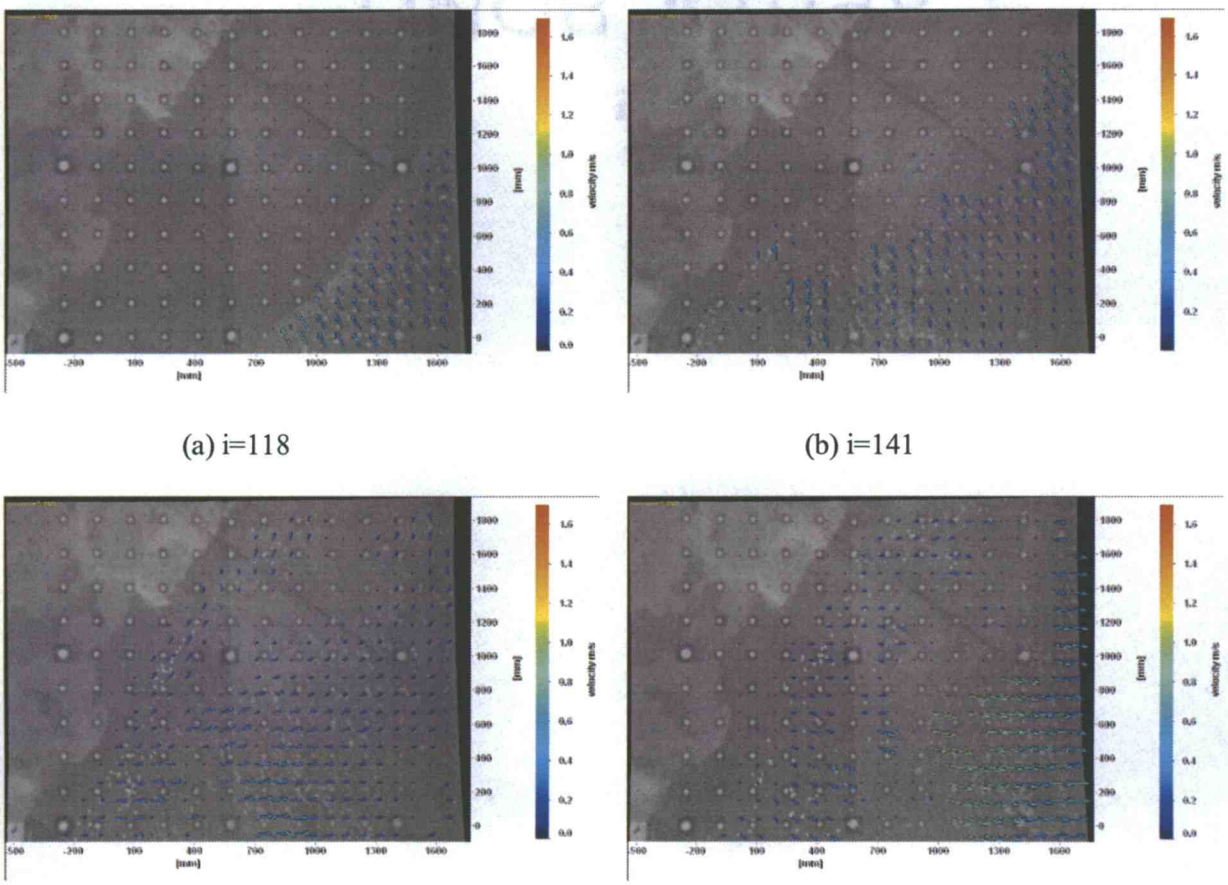

(a) i=118 (b) i=141

(c) i=170 (d) i=193

Figure 42: Vector field overlaid on the original images from the PIV camera on the steep bluff section.

(8) Synchronization of PIV vector fields with the remaining instrumentation using the LED signal

Figure 43 shows a time series of the free surface measured at the wavemaker and the signal output by the LED for test 1. The sudden drop (+3.5 V to 0 V) in the LED signal corresponds to the LED being turned off, which was also identified in the PIV record. Because the LED signal was sampled on the same DAQ as the wave gages and ADVs, one was able to use the LED to synchronize the PIV images with the remaining instrumentation.

For example, Figure 43 shows that the maximum free surface elevation at wave gage 0 occurred at t_W=5.3667 s and the LED was turned off at t_L=11.5 s. From the images (Figure

42(b)) it was seen that the LED was turned off at the 53rd image; therefore $t_{i=53}$=11.5 s. Moving backwards at a sampling rate of 30 Hz, the 1st image (Figure 42(a)) was at $t_{i=1}$=9.77 s. Setting t_W=0.0 s, the 1st image occurred at $t_{i=1}^{'}$ =4.4 s. From Figure 44, it was seen that the time when the maximum wave height occurred at wave gage zero was $t_W^{'}$=10.98 s. This method was applied to the data and a comparison of the ADV and PIV time series is shown in Chapter 5.2 and other data for time series of LED and wave gages are in Appendix C.

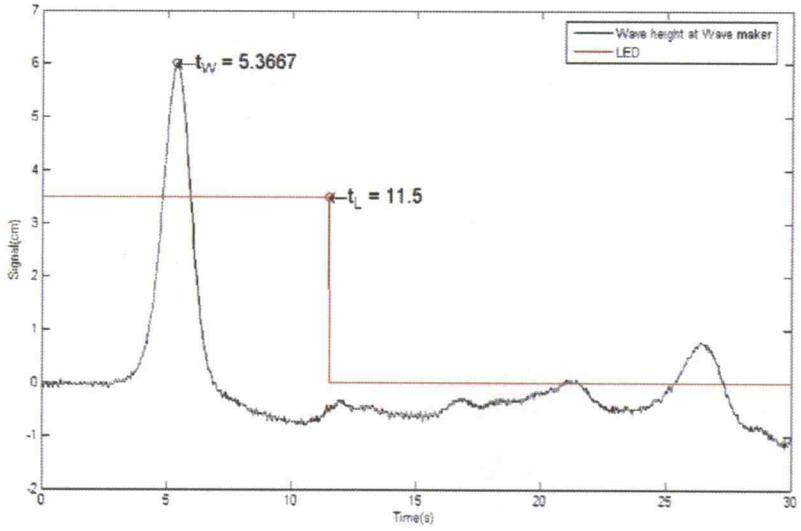

Figure 43: Wave gage and LED time series used to synchronize the PIV recording with the other instruments.

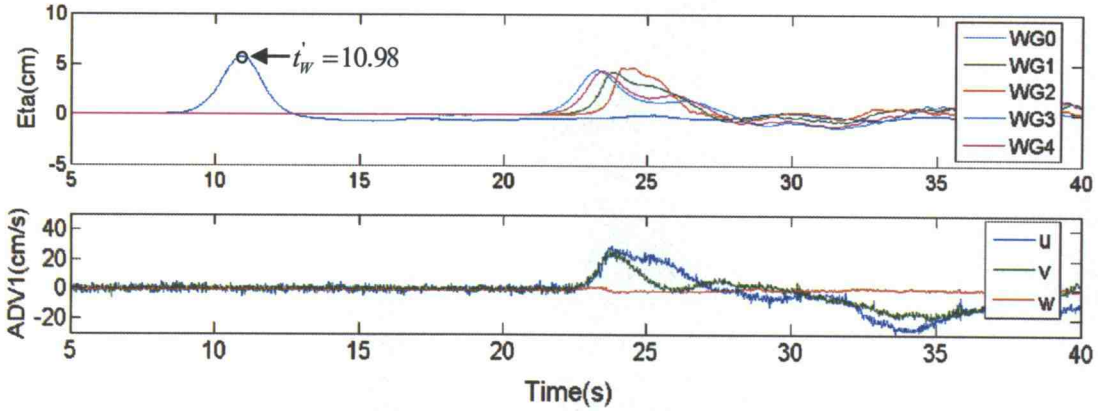

Figure 44: Time series of velocity recorded by the ADV and free surface recorded by the wave gages.

5. Results and discussions

5.1. Results of recording

5.1.1 ADV and wave gage results

Water particle velocity using ADVs and wave height using wave gages were measured over the majority of the basin as presented in previous chapter. The testing grid of ADVs and wave gages at a water depth of 55 cm is shown in Figure 45. The ADV needs at least 5 cm distance from its probe to the bottom boundary to measure velocities. Measurements were made from offshore area to onshore and ADVs and wave gages were removed were the water depth was too shallow to conduct measurements. For 55 cm water depth, the area inside the harbor can was measured.

Figure 46 and 48 shows the time series of wave gages and ADVs for cases 3 and 4, respectively. Description of the cases is listed in Table 2. Measurements were conducted at the Embayment section, Y=1 6m. WG0 represents the wave gage at the wavemaker. Wave gage 1, 2, 3 and 4 are located at X=18, 19, 16 and 17 m, respectively. ADV 1, 2, 3 and 4 are located at 18, 19, 16 and 17m. The probe of ADV was 3 cm below the still water level. These ADV data were used to compare with corresponding PIV data, which is in Chapter 5.2.

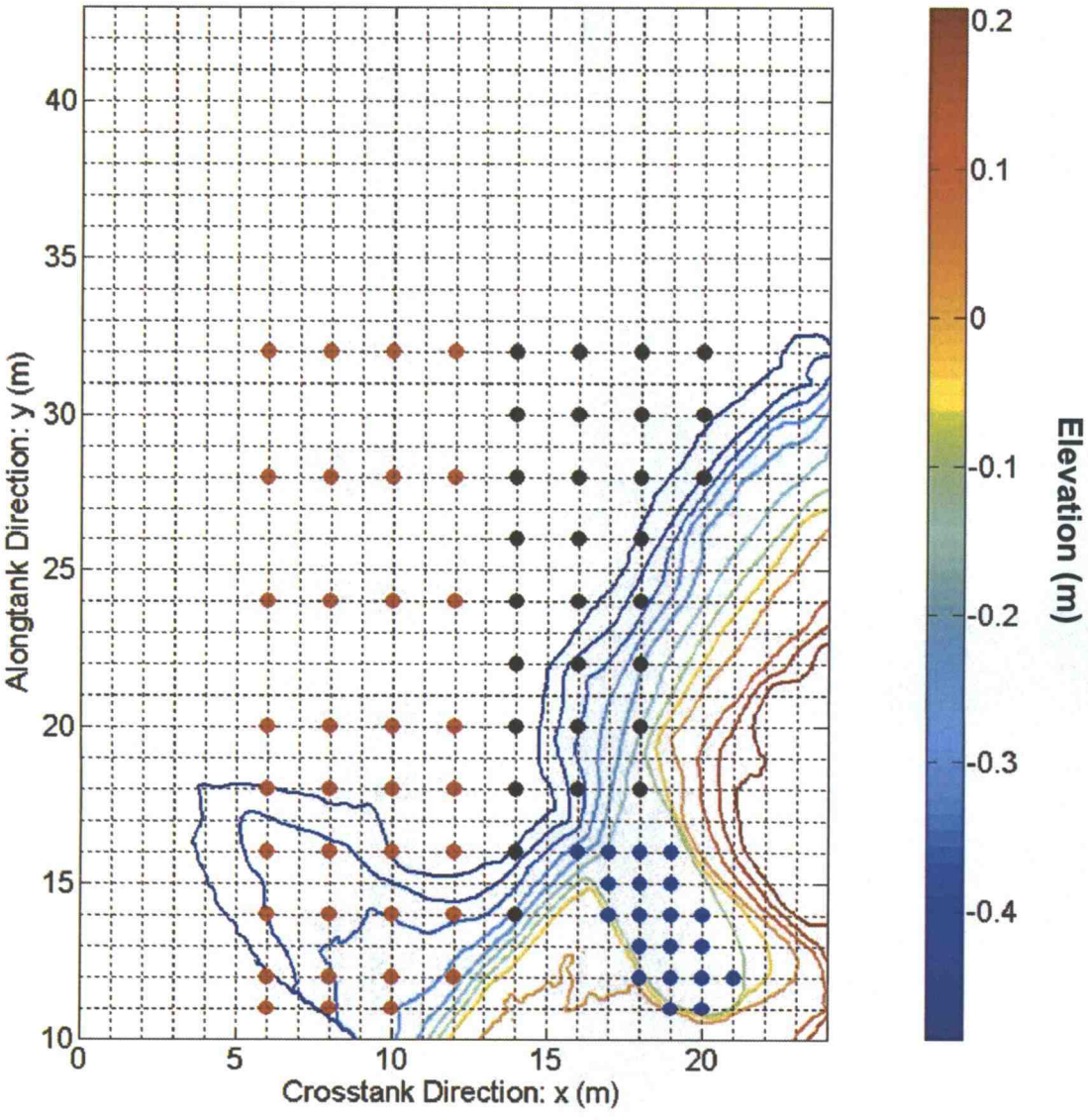

Figure 45: Test grid for ADVs and wave gages: D=55 cm.

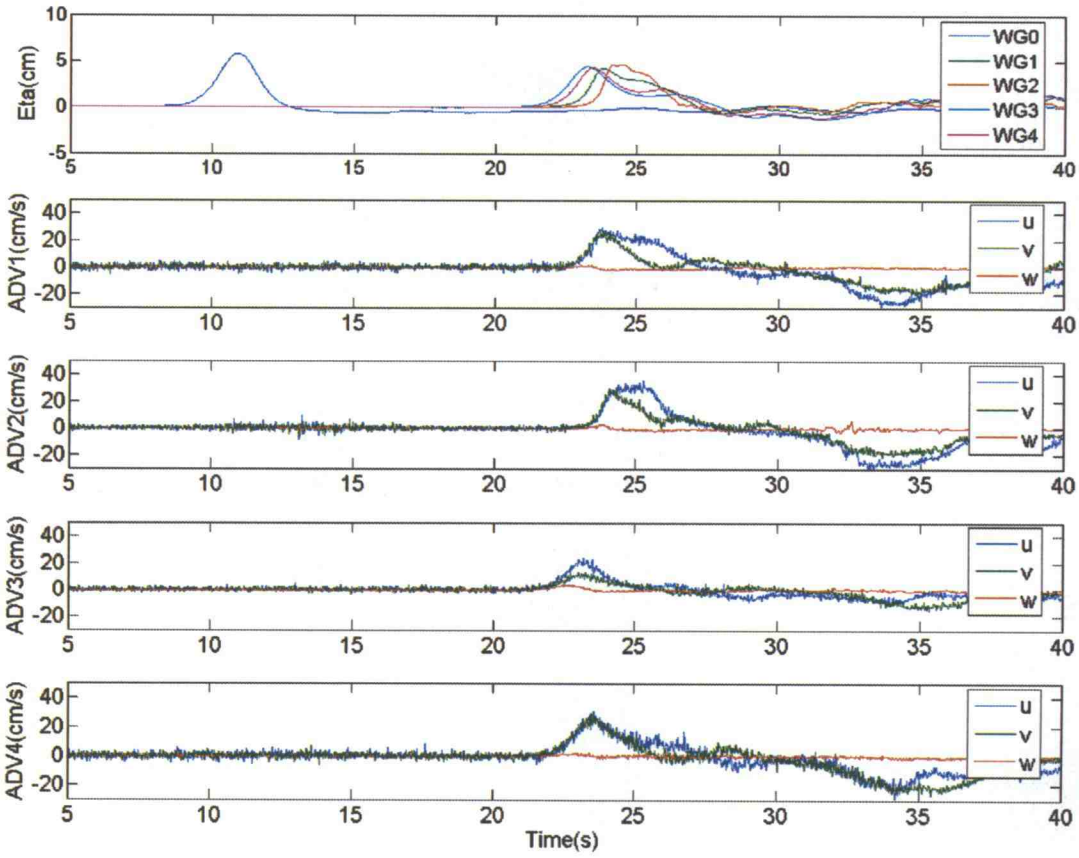

Figure 46: Time series of wave gages and ADV; D=55 cm; Ho=4.4 cm; Y=16 m; A1X=18 m, A2X=19 m, A3X=16 m, A4X=17 m; W1X=18 m, W2X=19 m, W3X=16 m, W4X=17 m.

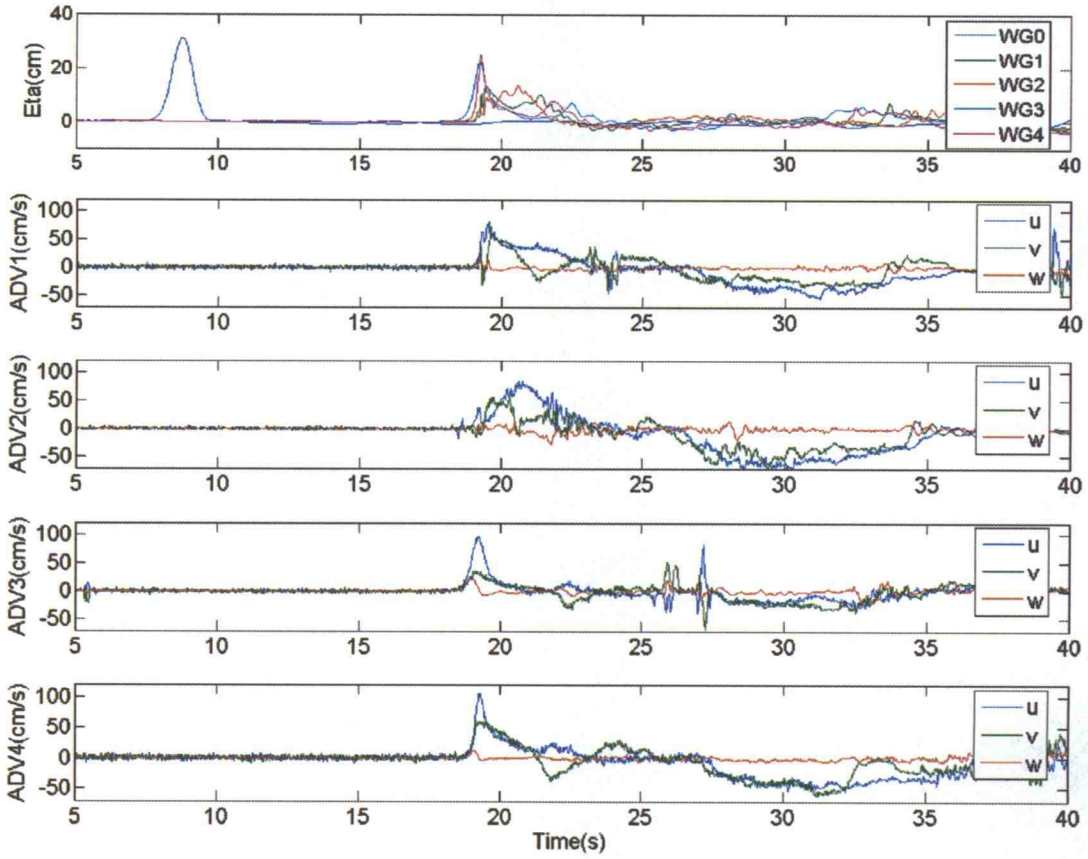

Figure 47: Time series of wave gages and ADV; D=55 cm; Ho=22.7 cm; Y=16 m; A1X=18 m, A2X=19 m, A3X=16 m, A4X=17 m; W1X=18 m, W2X=19 m, W3X=16 m, W4X=17 m.

5.1.2 PIV results at the steep bluff

(1) Test 1 (D=44 cm, FOV=S-1, Ho=4.4 cm)

Figure 48 shows the vector fields for test 1. The number of images recorded was 341 at a sampling rate of 30Hz. For each figure, 't' represents the time in the time series of wave gage and LED. The symbol 'i' represents the image index number in the PIV recording.

For example, Figure 48(a) is at t=12.00 seconds and i=68. That means the figure is at t=12.00 seconds and is the 68th figure in the PIV time series. For this test, D=44 cm and Ho=4.4 cm. The FOV S-1 (x=20-22 m, y=22-24 m) captures most of the wave motion including both run-up and run-down. When a wave inundates at its maximum elevation, the water particle velocity at the front part of propagating wave should be zero. Therefore, it can be observed that a wave inundates at maximum elevation between Figure 48(d) and (e). Some vectors moving upward in the FOV can be observed in Figure 48(d). The wave was then reflected by the steep bluff and changed its direction to the offshore in Figure 48(d)-(e).

The maximum velocity is presented in each figure as Vmax for a reference. It is worth noting that the rundown velocity was as large as the runup velocity, as can be seen by comparing figures 49 (b) and (f). Figure 48(a) shows a good distribution of vectors in the FOV. Those of (f) are relatively sparse. It is assumed that there were enough distributed tracers in Figure 48(a), resulting in a vector field that was uniformly distributed. It is not difficult to obtain a uniform vector field when such a small area needs to be seeded. As the area to be seeded increases, however, the resulting vector fields become sparse as shown in Figure 48 (b) to (f). In those cases, whole the vector field can not be obtained. It was still possible to observe the local wave motion and representative wave speed from these local vector fields, however.

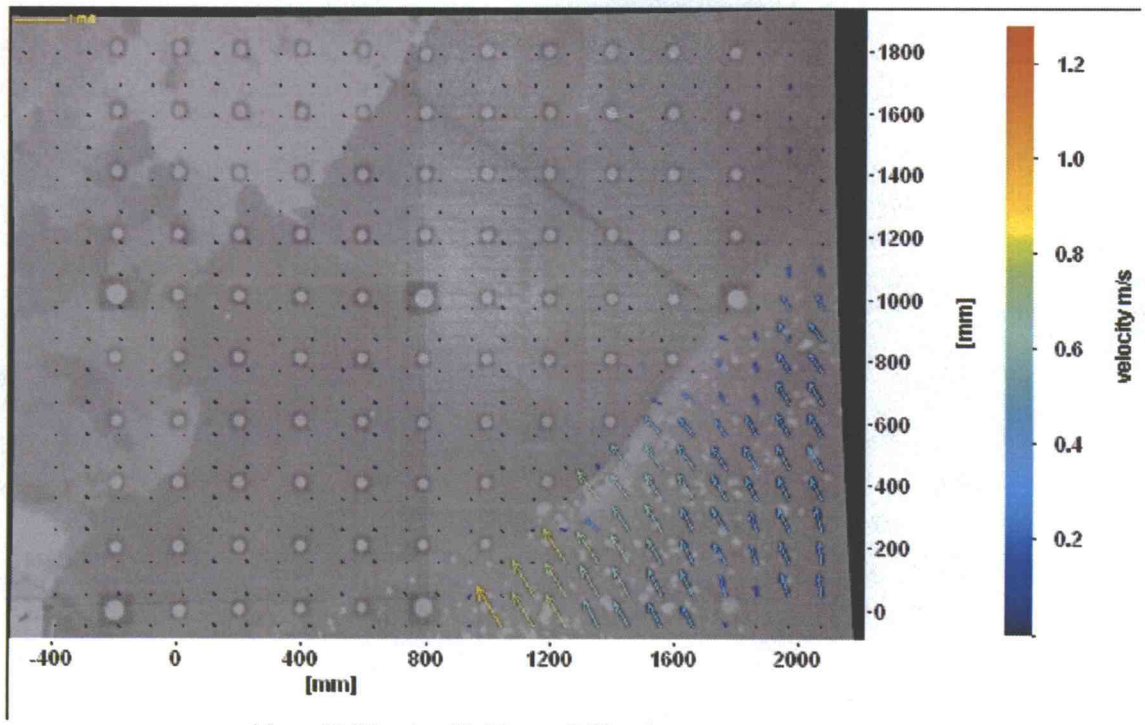

(a) t = 12.00 s; i = 68; Vmax=0.89 m/s

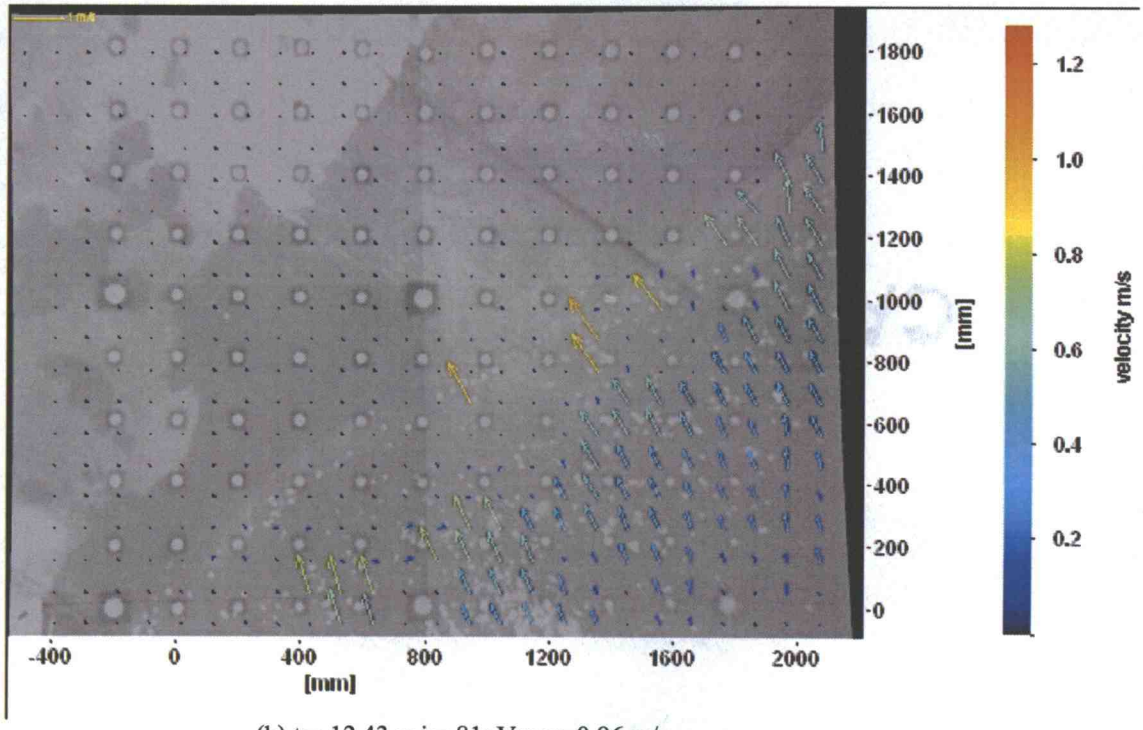

(b) t = 12.43 s; i = 81; Vmax=0.96 m/s

Figure 48: Vector field for test 1; steep bluff; D=44 cm; FOV=S-1; Ho=4.5 cm.

Figure 48(continued)

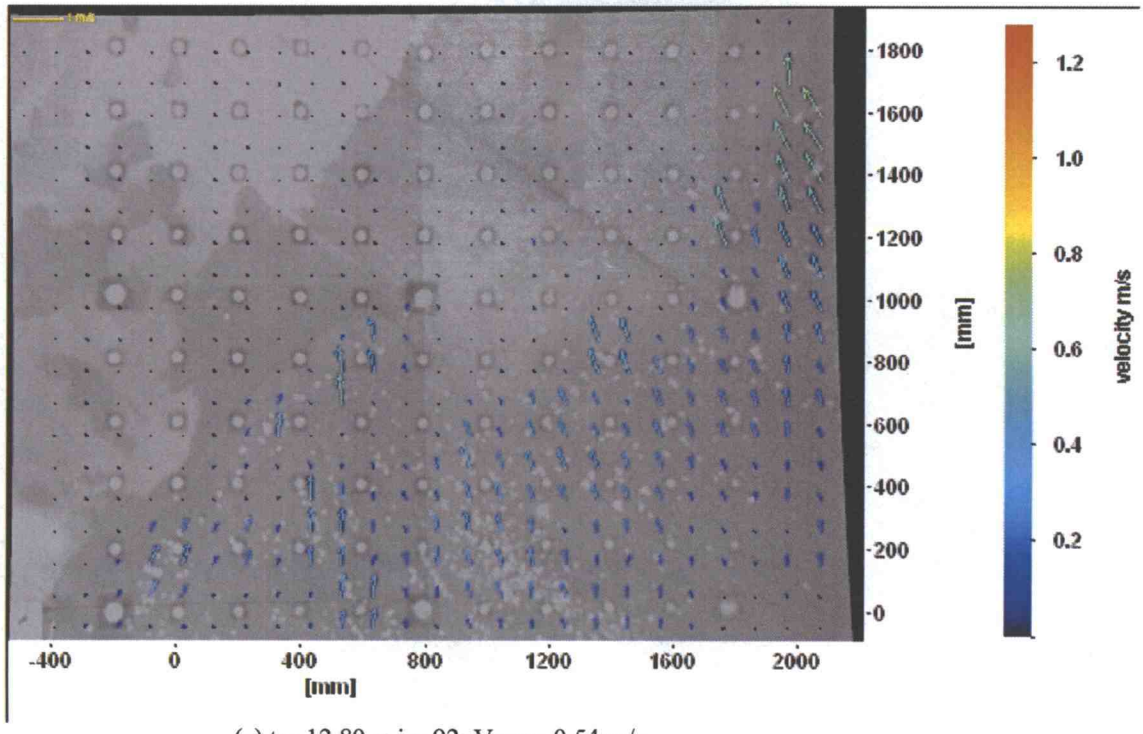

(c) t = 12.80 s; i = 92; Vmax=0.54 m/s

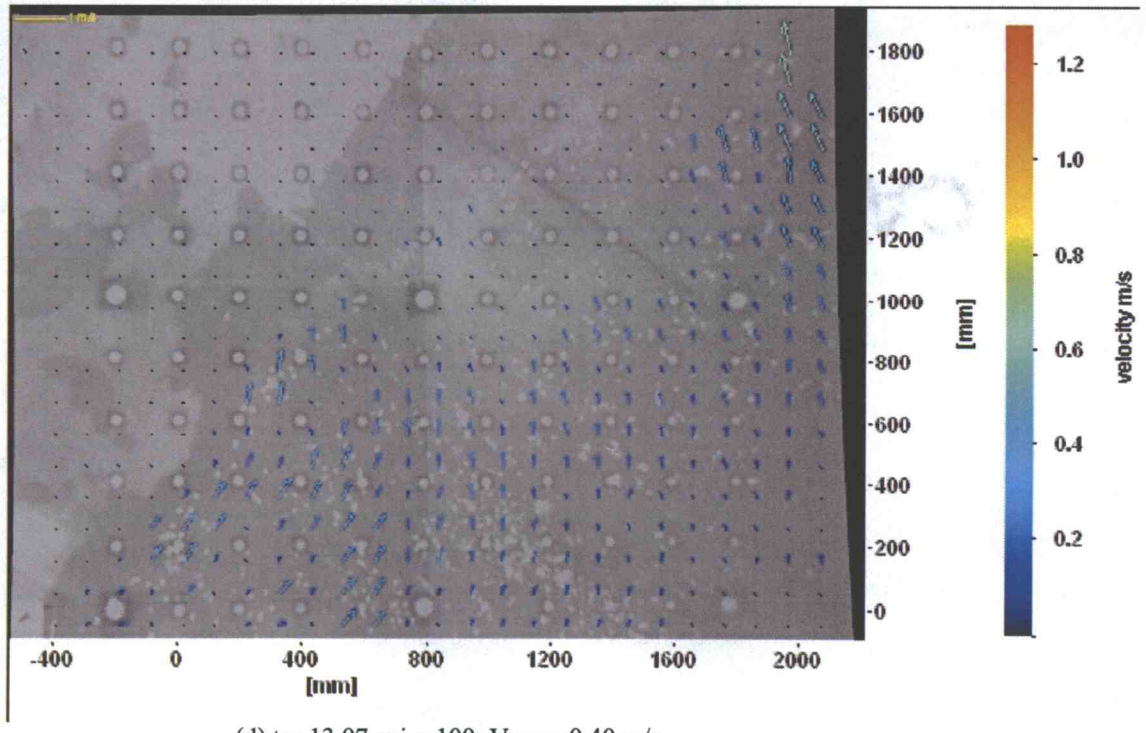

(d) t = 13.07 s; i = 100; Vmax=0.40 m/s

Figure 48(continued)

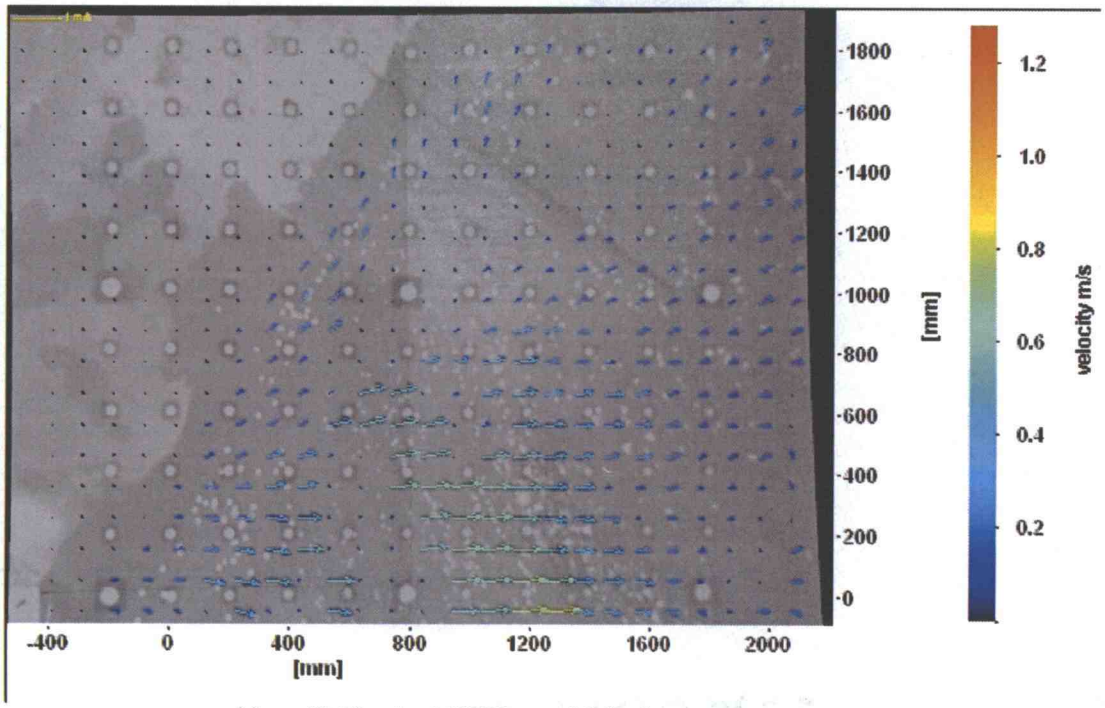

(e) t = 13.70 s; i = 119; Vmax=1.06 m/s

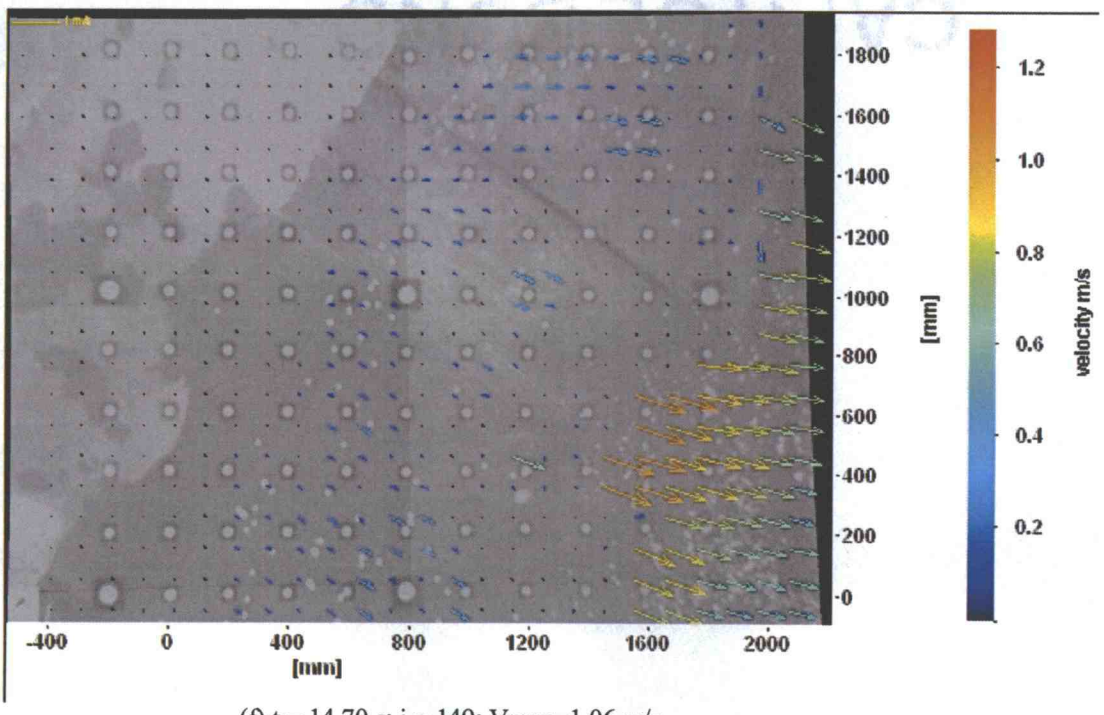

(f) t = 14.70 s; i = 149; Vmax=1.06 m/s

(2) Test 2 (D=44 cm, FOV=S-1, Ho= 7.9 cm)

Figure 49 shows the vector field for test 2. The user defined wave has different characteristics from other "Tsunami" or solitary waves. For example, case 1(i.e. Ho=4.5 cm, D=44 cm) was generated by using a 16 % stroke of the wave board. The maximum wave board displacement is 2 m. The user defined wave is generated by using 81 % stroke. Therefore, the most remarkable difference between the solitary wave and the user defined wave is the wavelength. From the results of the ADVs, in general, a user defined wave has larger velocity than that of case 1. The same trend can be seen for run-up velocity with the PIV measurements.

First, the wave inundated from the bottom of the FOV as shown in Figure 49(a) and (b). Then the tracers began to separate into mainly two flows. One flow inundated to the top in the FOV and the other was reflected by the steep slope, changing its direction as a return flow as shown in Figure 49(c) to (e). It can be observed from the vector field that the front area of the propagating wave has maximum velocity. This also held true for test 1. The vector field presented in Figure 49 is sparser than that in Figure 48. This may be explained by size of area to be seeded. It is obvious that the area to be seeded in Figure 49 is larger than that in Figure 48. In addition, flow separation during the wave inundation enhanced sparser tracers in the FOV.

Case 2 shows a larger inundation than case 1. The FOV S-1 can not hold the entire wave inundation for this case. Therefore, test 3 and 4 at the FOV S-2 and S-3 are added to measure run up velocity. The PIV time series of test of 2, 3, and 4 can be synchronized using the time series of the wave gage and LED. Time series of the wave gages and LED for all tests are in Appendix C.

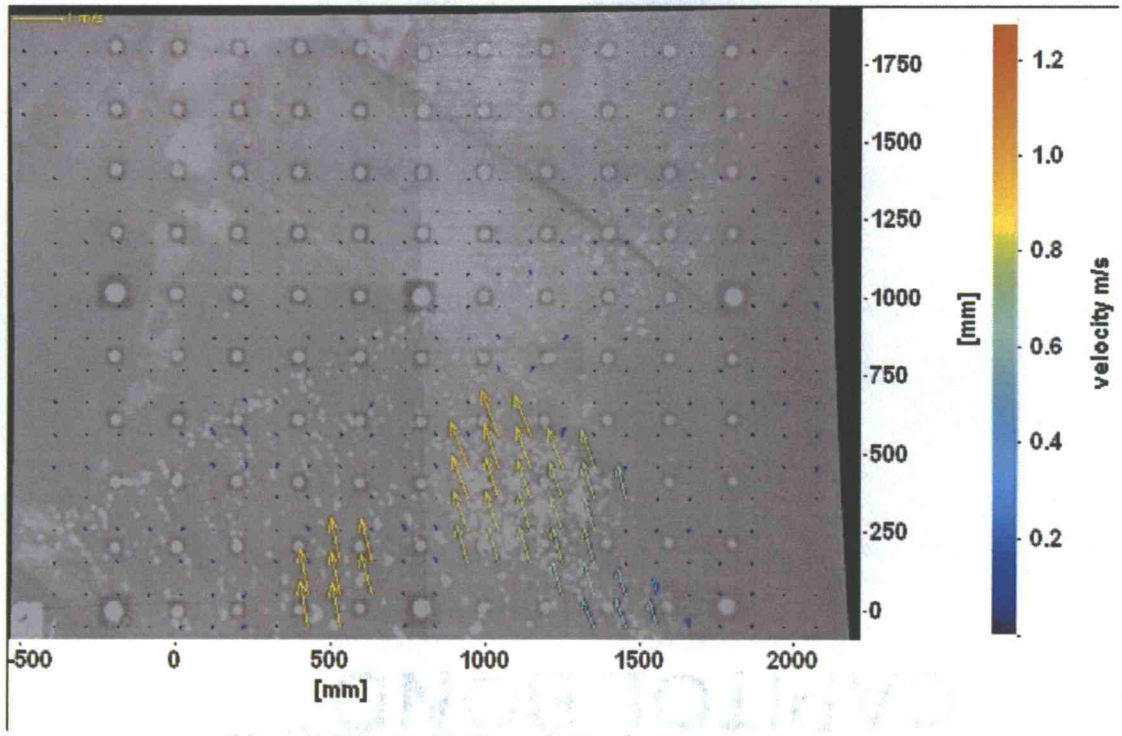

(a) t = 41.37 s; i = 80; Vmax=0.94 m/s

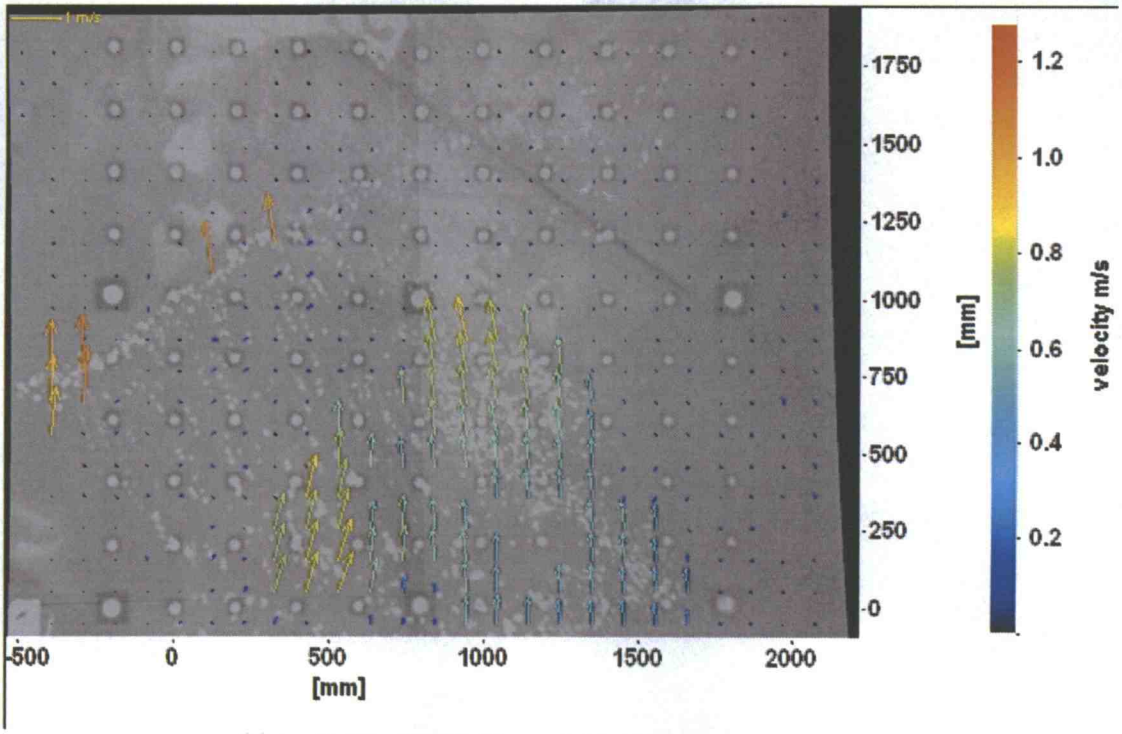

(b) t = 41.77 s; i = 92; Vmax=1.11 m/s

Figure 49: Vector field for test 2; steep bluff; D=44 cm; FOV=S-1; Ho=7.9 cm.

Figure 49(continued)

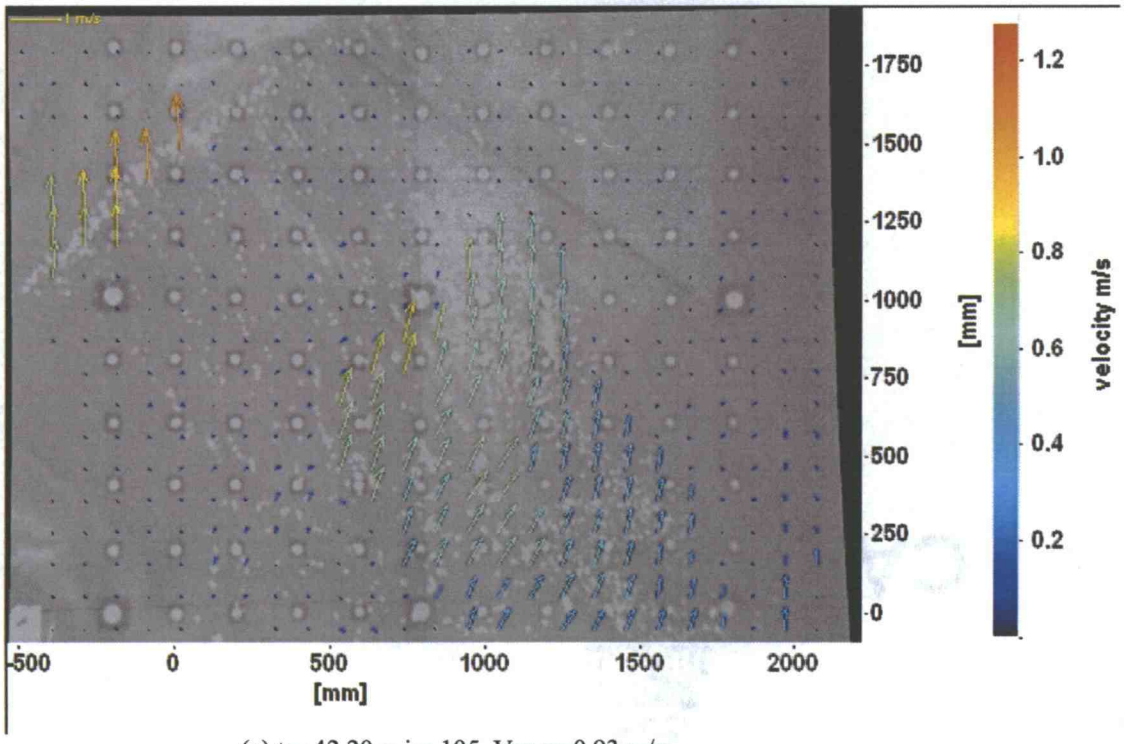

(c) t = 42.20 s; i = 105, Vmax=0.93 m/s

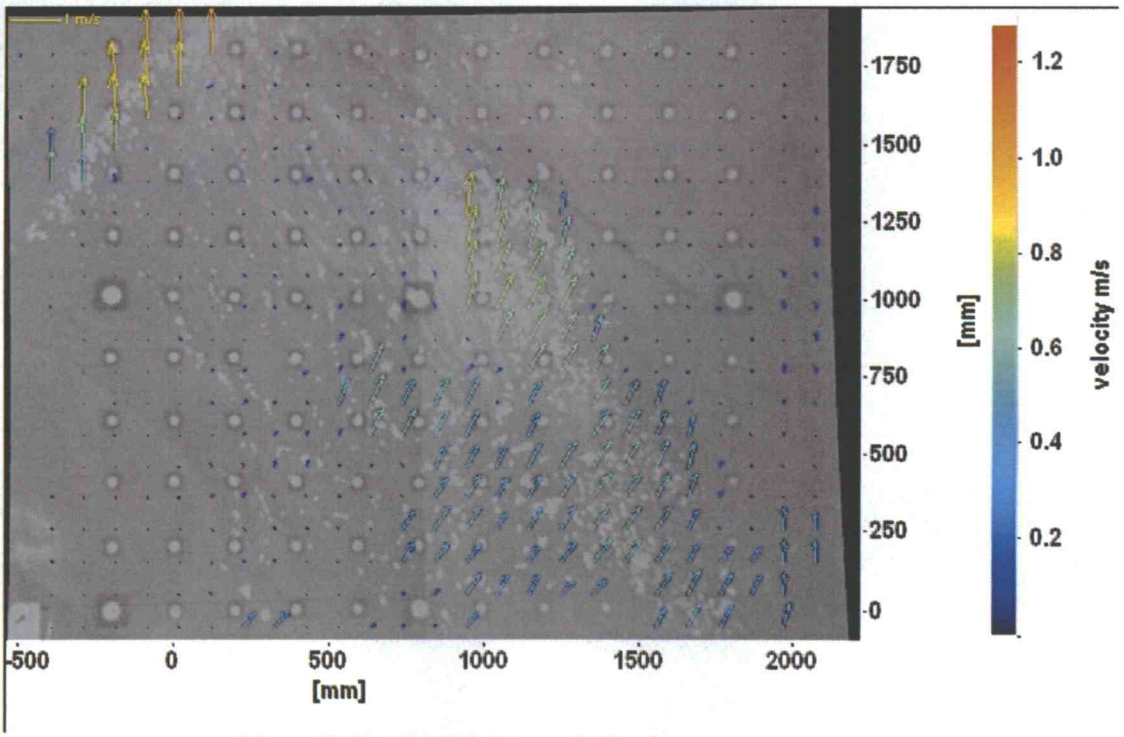

(d) t = 42.43 s; i = 112; Vmax=0.62 m/s

Figure 49(continued)

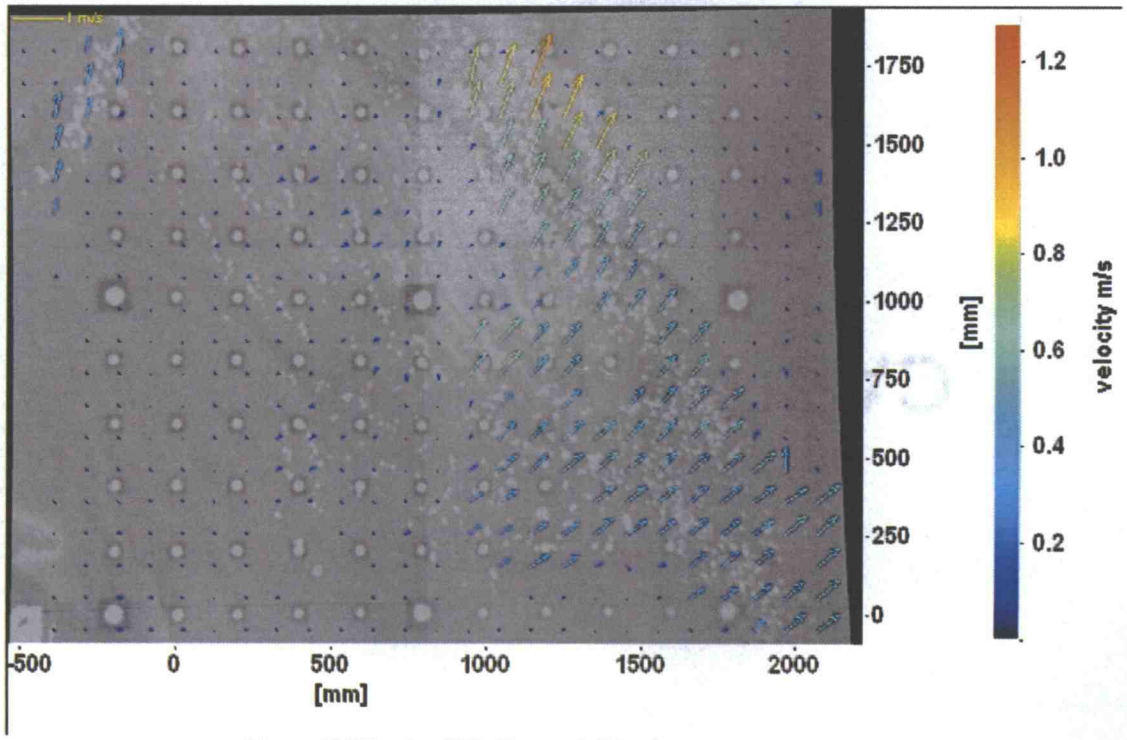

(e) t = 42.87 s; i = 125; Vmax=1.02 m/s

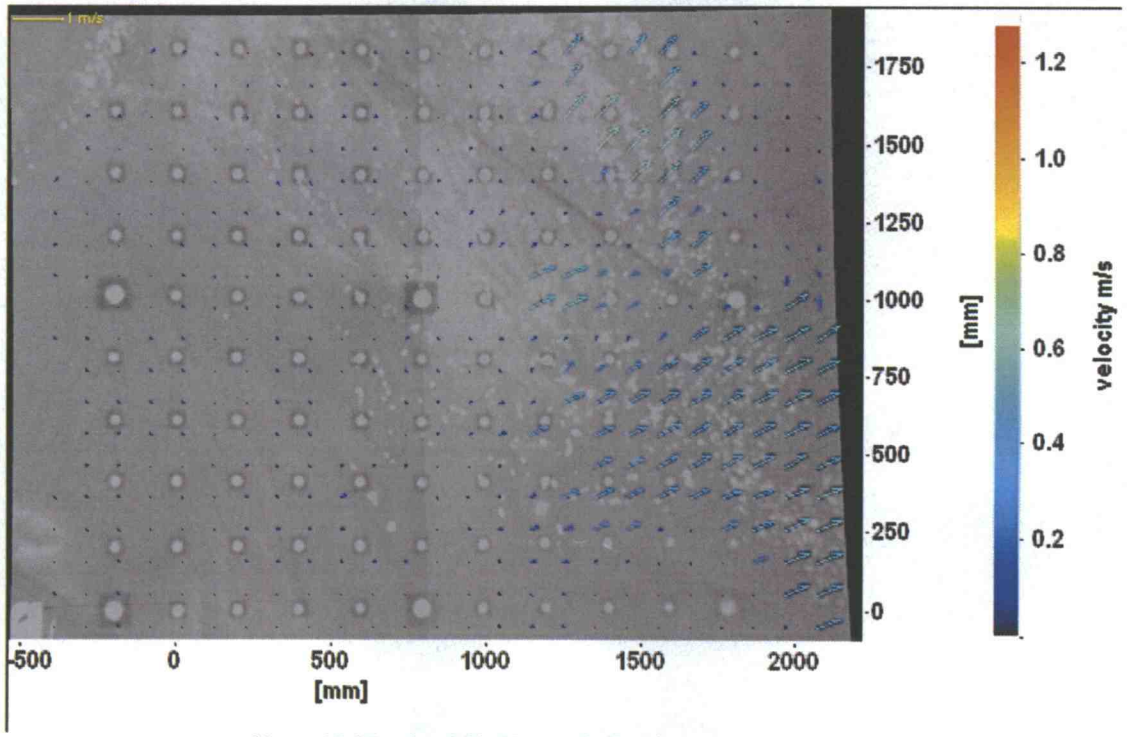

(f) t = 43.37 s; i = 140; Vmax=0.62 m/s

(3) Test 4 (D=44 cm; FOV=S-3, Ho=7.9 cm)

Figure 50 shows the vector fields for test 4. It is worth noting that the user defined wave was measured for both tests 2 and 4. The only difference is the location of FOV. The FOV S-1(X=20-22 m, Y=22-24 m) was selected for test 2. FOV S-3 (X=20-22 m, Y=20-22 m) was selected for test 4. Different tests were repeated for the same wave case, because the user defined wave inundates from FOV S-1 to S-3. The tracers distribution in FOV is not the same in Figure 49 and 51 because they are different trials. Therefore, local vectors emerged in different locations between the two figures.

From Figure 50(a), it can be observed that the runup velocity did not decrease by inundating from FOV S-1 to S-3. However, the surging wave slowed down due to the steep slope as shown in Figure 50(b). The wave reflected by the slope changed its direction (Figure 50(c)) and finally returned to the offshore direction (Figure 50(d)).

Now the wave inundation at the steep bluff compared to a real world scenario is discussed. From the view of a person who observes the wave from inland at the steep bluff section, the wave inundates up to the bluff, then flowed parallel to the edge of the bluff with strong velocity. Suppose a person stands on a small white dot at x=1000 and y=1250 in Figure 50(b). The most dangerous wave for them is not the wave that inundates toward them directly from offshore, but the wave reflected by the bluff, which is approaching from the side as shown in Figure 50(c). Wave inundation reflected by the bluff may be described as "secondary wave inundation". The person's location on land is in danger due to secondary wave inundation. This is only one example of wave inundation for the bathymetry. However it should be noted that sometimes the secondary wave inundation causes the maximum inundation level to be reached.

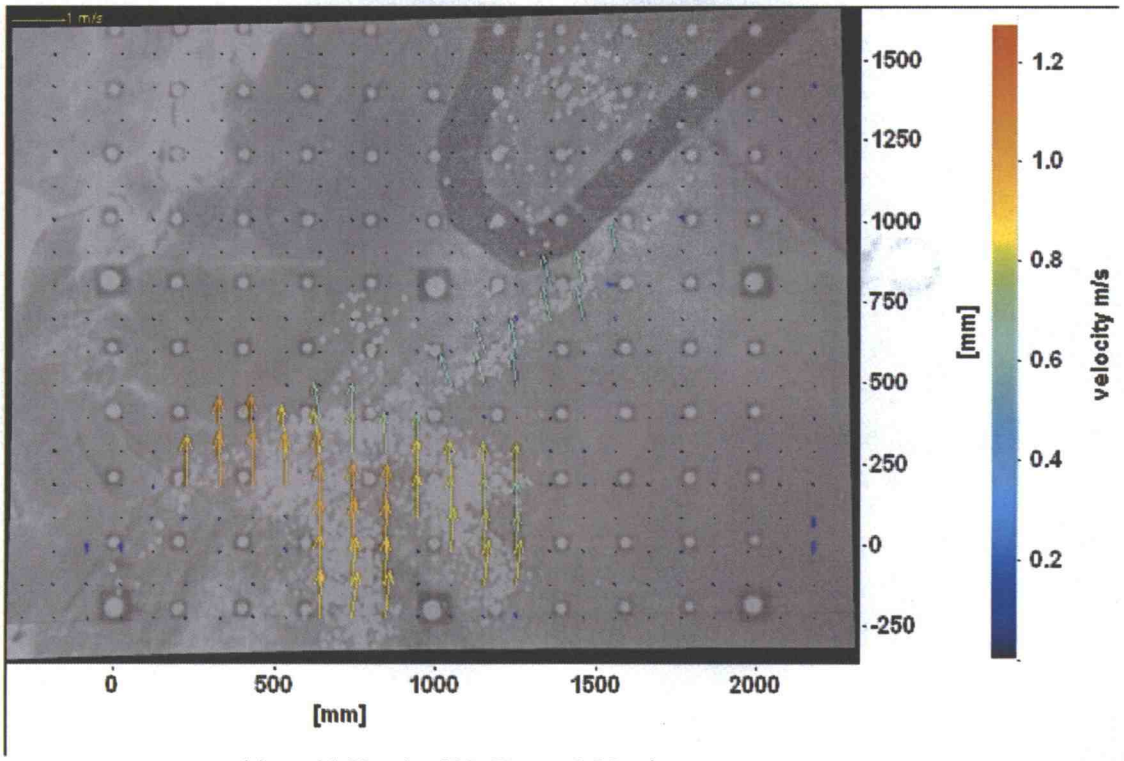

(a) t = 44.00 s; i = 105; Vmax=1.05 m/s

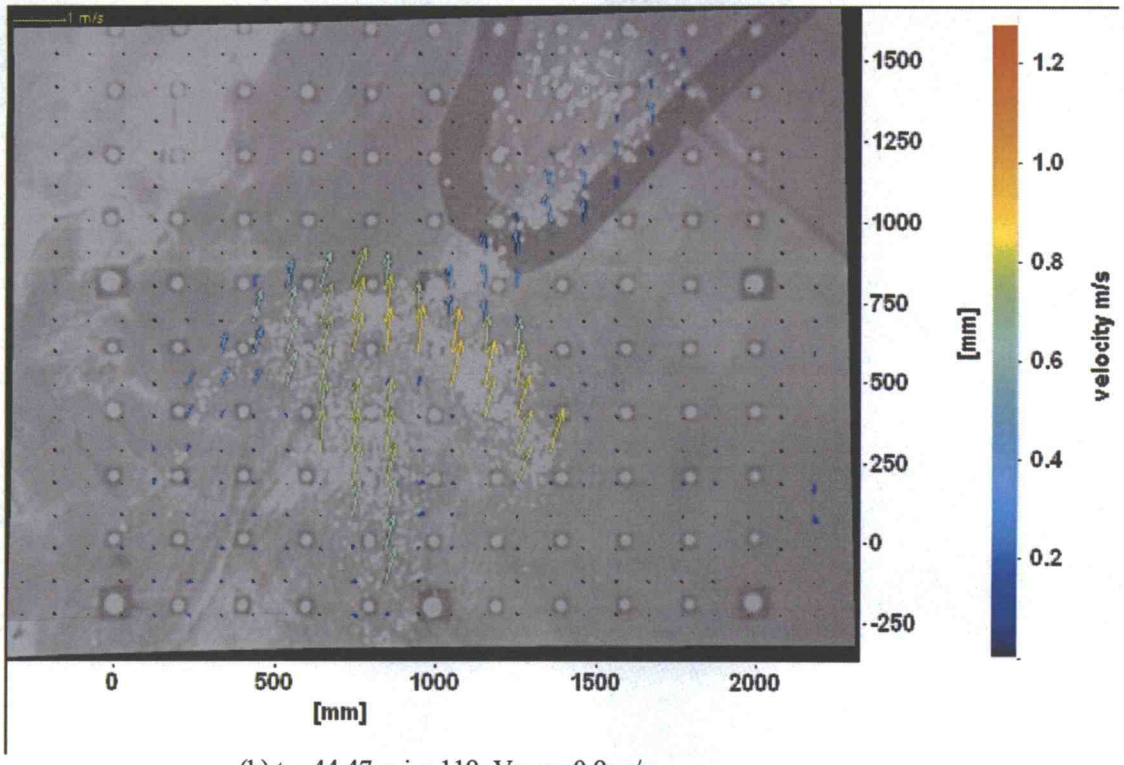

(b) t = 44.47 s; i = 119; Vmax=0.9 m/s

Figure 50: Vector field for test 4; steep bluff; D=44 cm; FOV=S-3; Ho=7.9 cm.

Figure 50(continued)

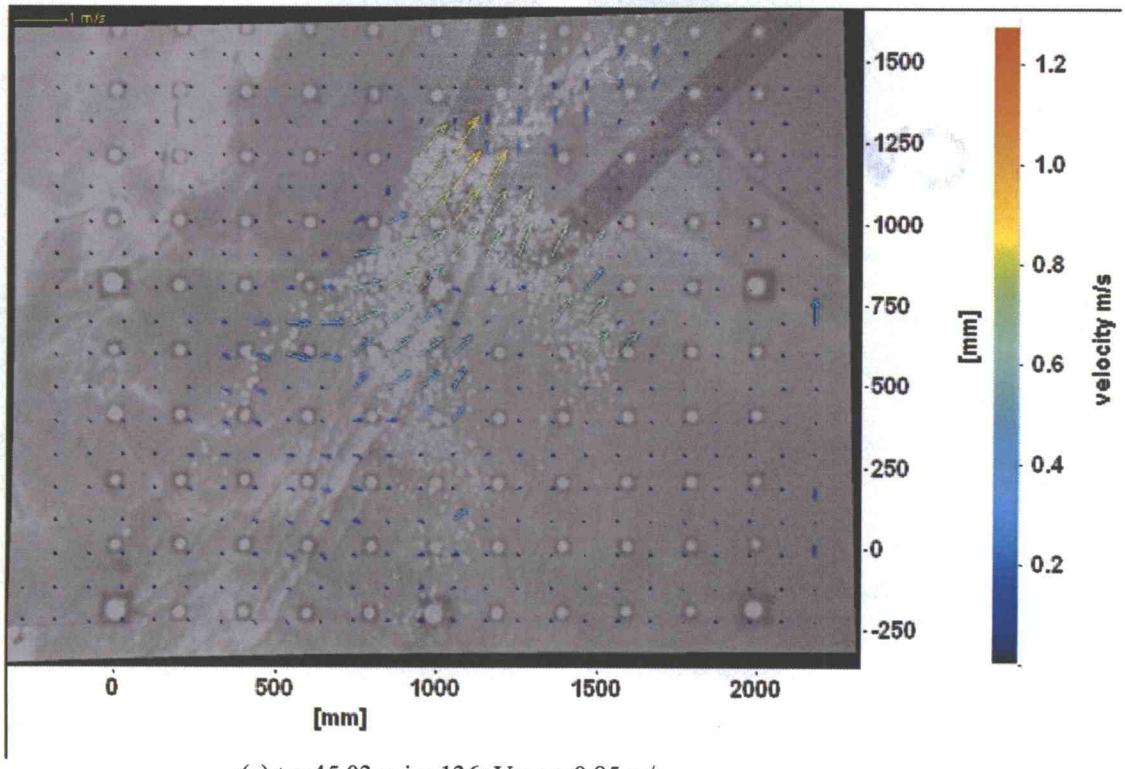

(c) t = 45.03 s; i = 136; Vmax=0.85 m/s

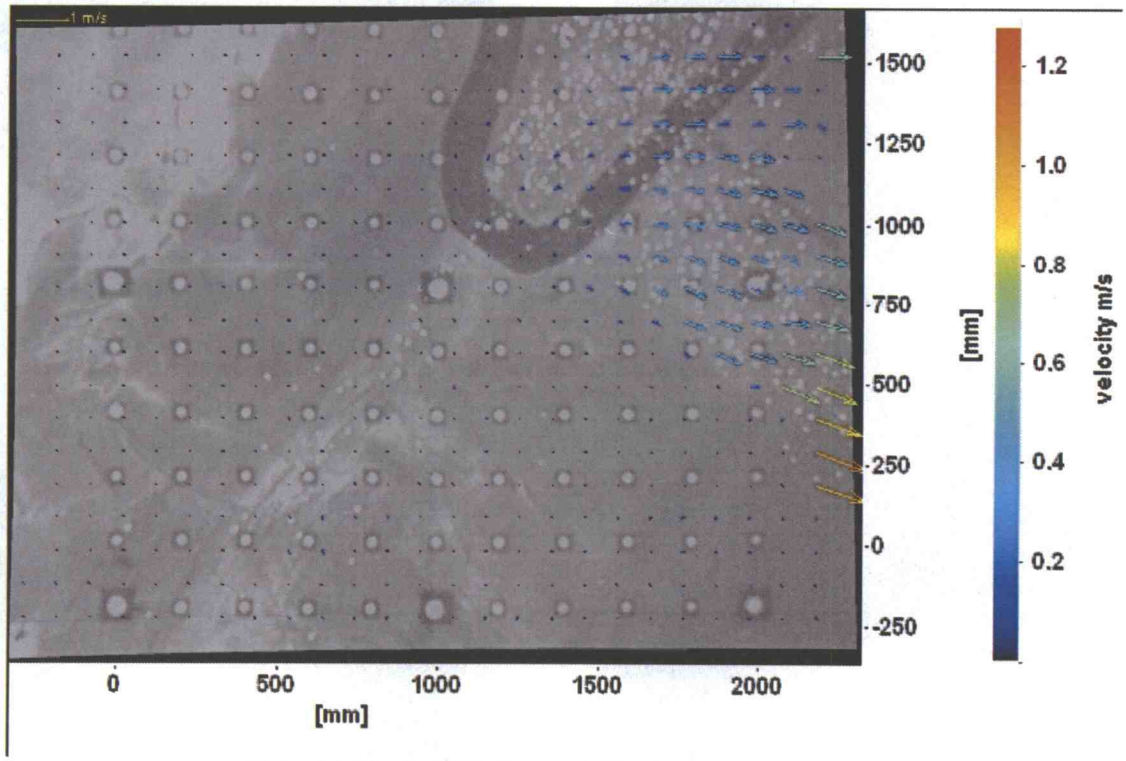

(d) t = 46.90 s; i = 192; Vmax=1.00 m/s

(4) Test 5 (D=55 cm, FOV=S-1, Ho=22.7 cm)

Water particle velocity with Ho=22.7 cm was larger than with any other type of wave. This was the only case that the interrogation window size of 128 x 128 pixels could not be applied. The window size of 128 x 128 pixels was too small to calculate water surface velocity for this case. Therefore, the interrogation window size of 256 x 256 pixels was applied for case 4. To avoid losing a lot of vectors, 50 % overlap was applied for each interrogation window. The calculated vector field for test 5 is presented in Figure 51. Measurements of the maximum inundation level were not conducted since the wave was large enough to inundate most areas of the model. For all wave cases, except for the case 4, the water surface velocity was measured from the tracers by the PIV. However, for only wave case 4, the tracers were not easily detected by the PIV since they were covered with the white water of the breaking wave. The PIV seemed to detect the white water as tracers, instead. Tracers were put in by the same method as for other tests. However, it is obvious from Figure 51 that they could not be detected for the breaking (surface roller) area. The resulting vector field was noisier and had more errors due to the white water. It was observed that the vector field itself had some uniformity in terms of magnitude and direction. Figure 51(a) shows that the wave was already broken when it came into FOV S-1. Therefore, the PIV traced the white water from the beginning. The velocity was much larger than those of any other type of waves. The maximum velocity measured in each figure was near 3 m/s. After the front part of a breaking wave passed through, some tracers were detected as shown in Figure 51(c) and (d). Calculated velocity from the white water had some uncertainties in its accuracy. On the other hand, velocities obtained by the tracers in Figure 51(c) and (d) were more reliable. The water surface velocity at the front part of the breaking wave was larger than that behind the breaking part. The velocities at the rear part of the breaking wave were approximately 1.5 to 1.8 m/s. Therefore, it is assumed that water surface velocity of breaking area should be larger than these velocities.

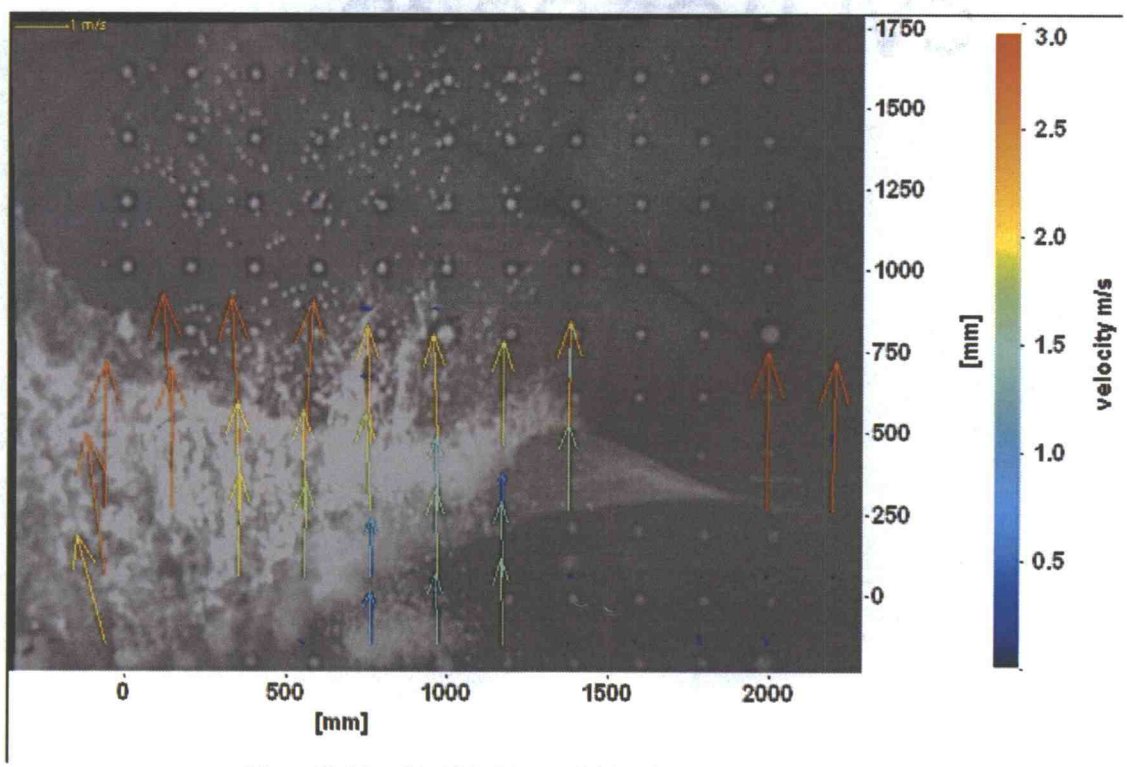

(a) t = 13.37 s; i = 107; Vmax=2.95 m/s

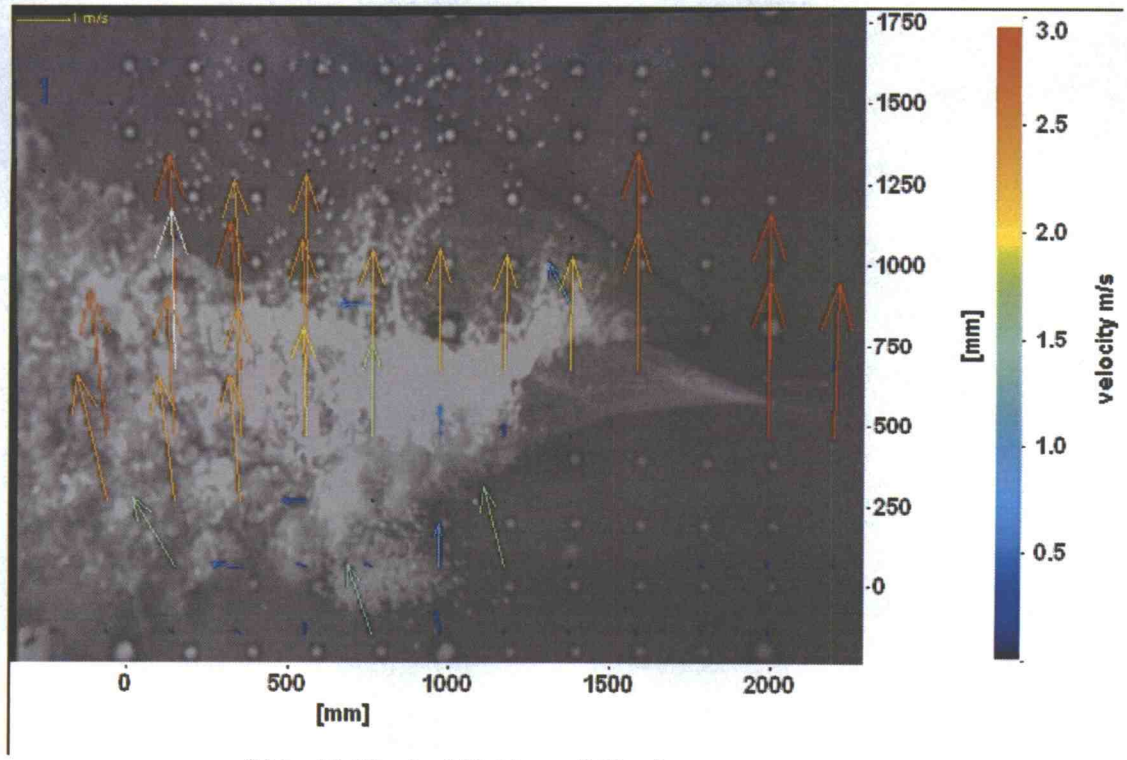

(b) t = 13.47 s; i = 110; Vmax=2.99 m/s

Figure 51: Vector field for test 5; steep bluff; D=55 cm; FOV=S-1; Ho=22.7 cm.

Figure 51(continued)

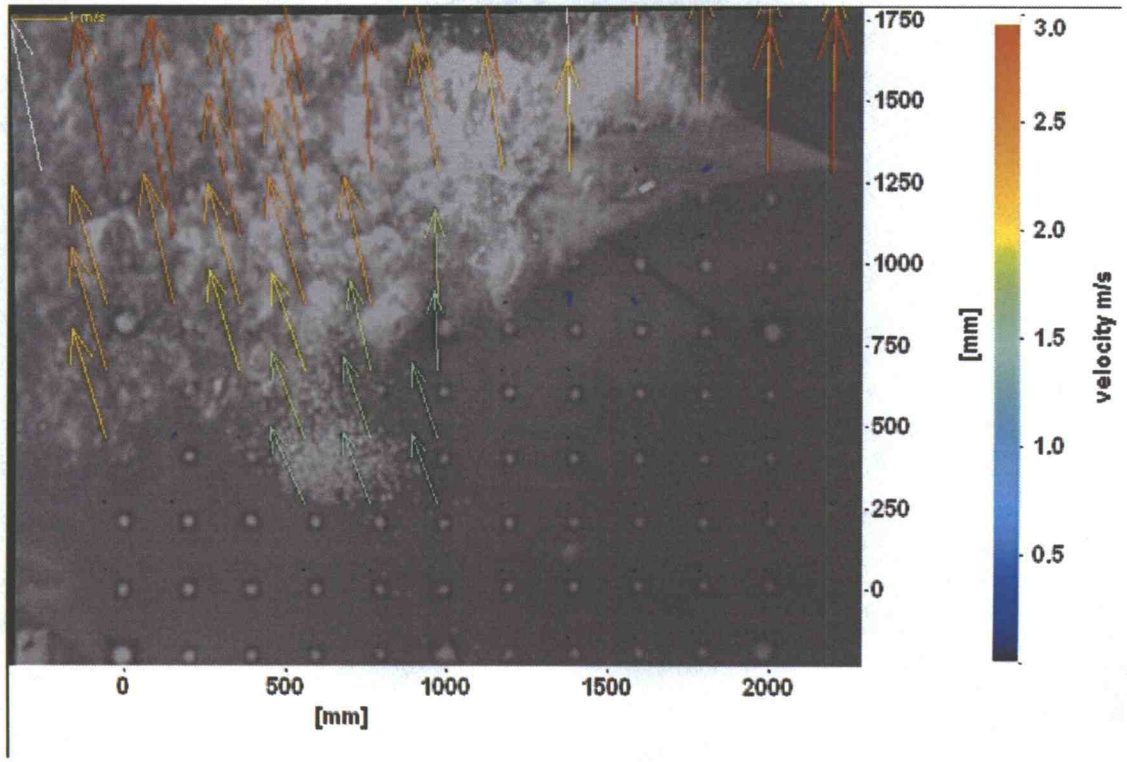

(c) t = 13.73 s; i = 118; Vmax=2.97 m/s

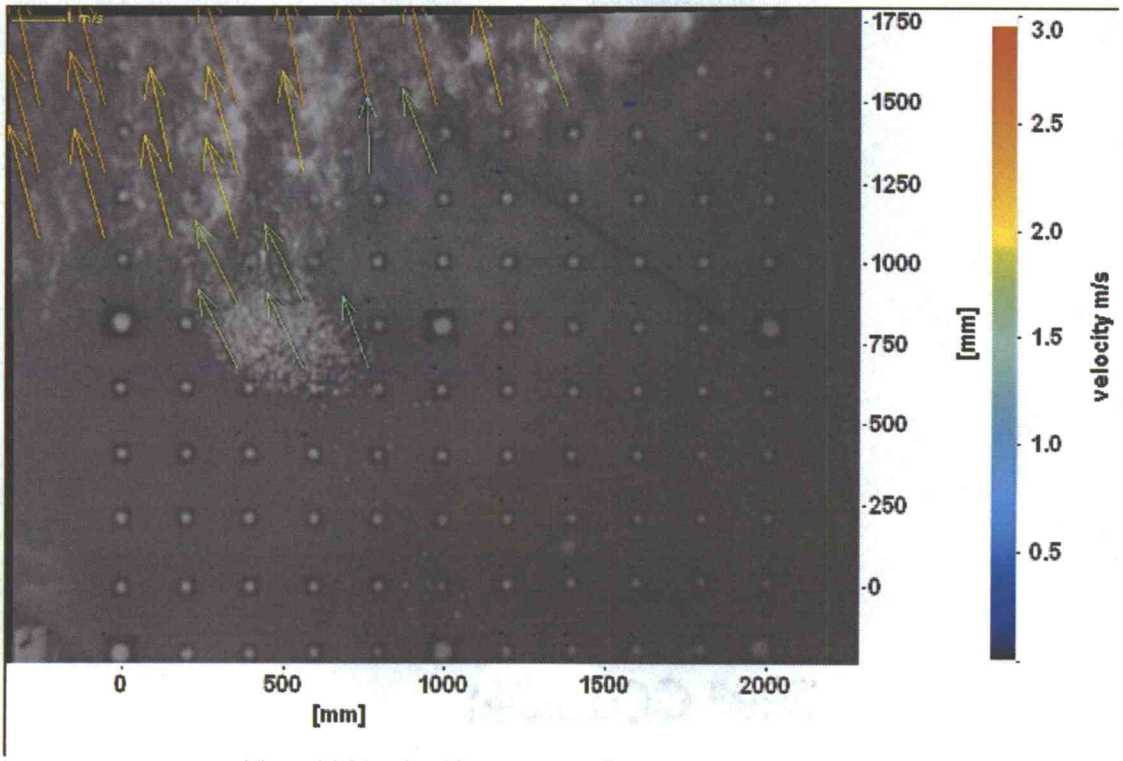

(d) t = 14.00 s; i = 126; Vmax=2.43 m/s

5.1.3 PIV results at the low foreshore

(1) Test 8 (D=44 cm, FOV=L-1, Ho=4.5 cm)

The low foreshore section was an area where the maximum inundation level typically was observed since it had a flat plane area behind a mild slope area. Figure 52 shows velocity vectors for test 8. The inundation level was low and water particle velocities were small. Case 1 generally showed the minimum inundation level among all wave cases and the FOV L-1 was the area with mild slope. Therefore, no remarkable inundation was observed for this test. There were two interesting characteristics to be mentioned. First, run down velocities were larger than those of run up, as seen by comparing with Figure 52(b) with (d). Second, it is observed from Figure 52(c) that there were two different wave directions existing at the same time. The vectors at the left bottom in the FOV were directed to offshore or left in the FOV. At the same time, the vectors at the top right in the FOV were directed onshore. This means that wave run up and run down occurred at the same time.

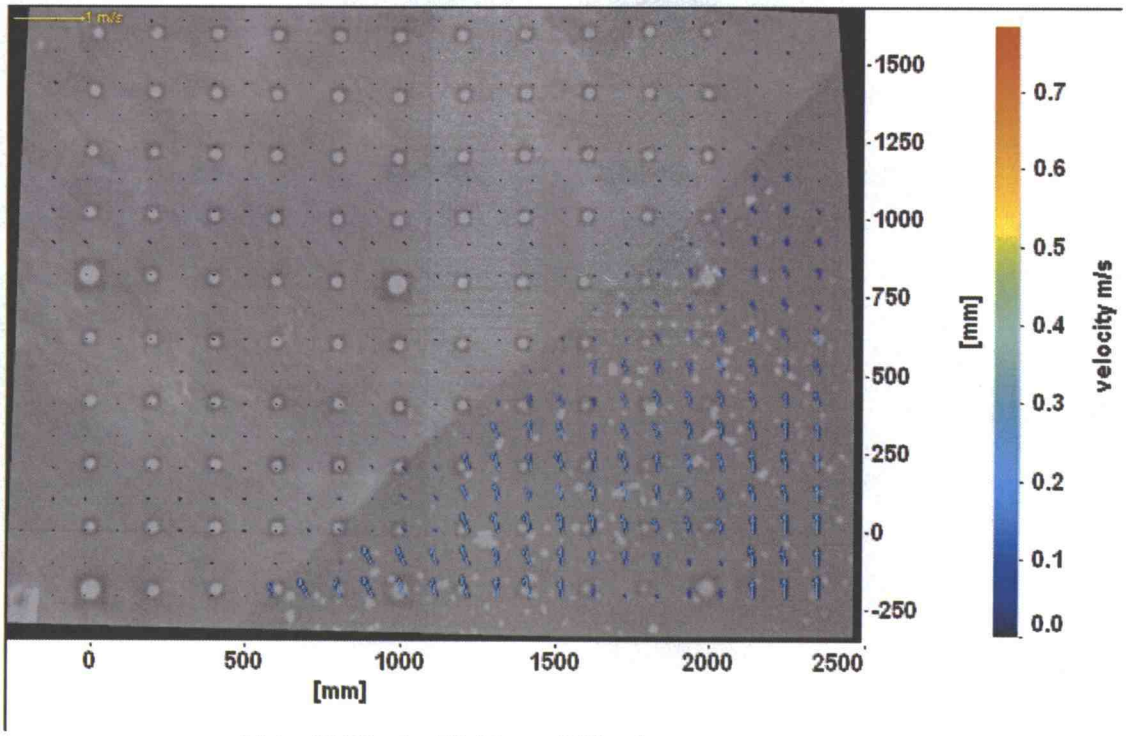

(a) t = 48.27 s; i = 73; Vmax=0.28 m/s

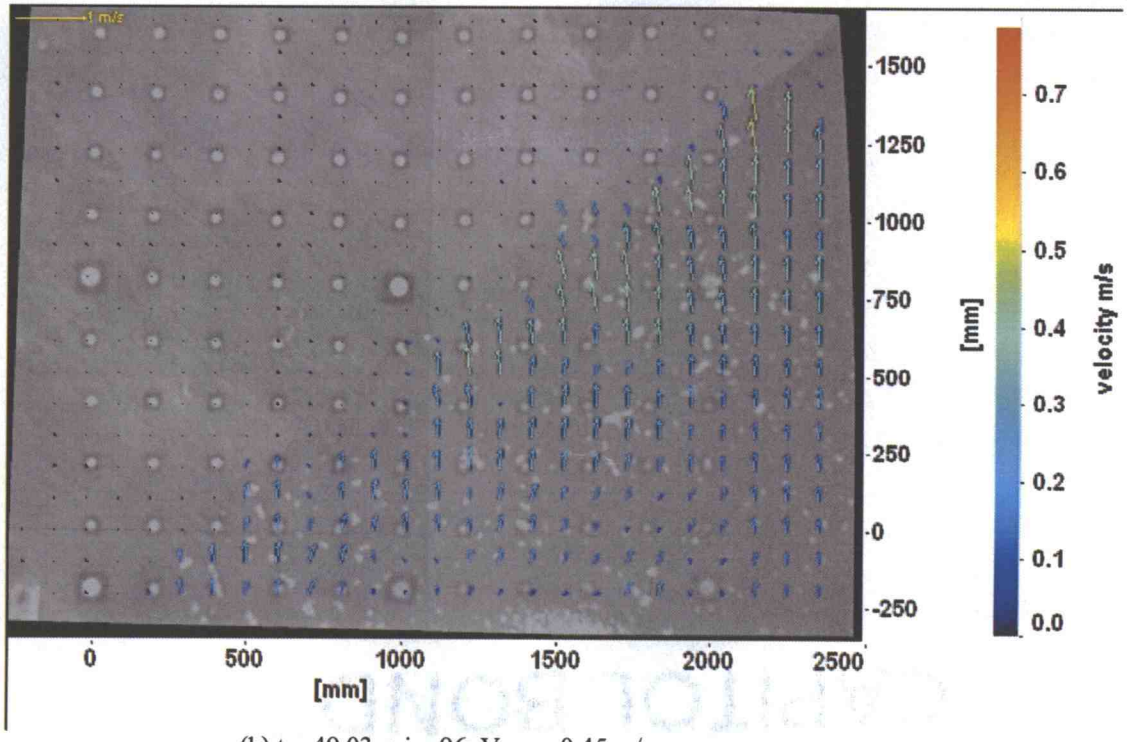

(b) t = 49.03 s; i = 96; Vmax=0.45 m/s

Figure 52: Vector field for test 8; low foreshore; D=44 cm; FOV=L-1; Ho=4.5 cm.

Figure 52(continued)

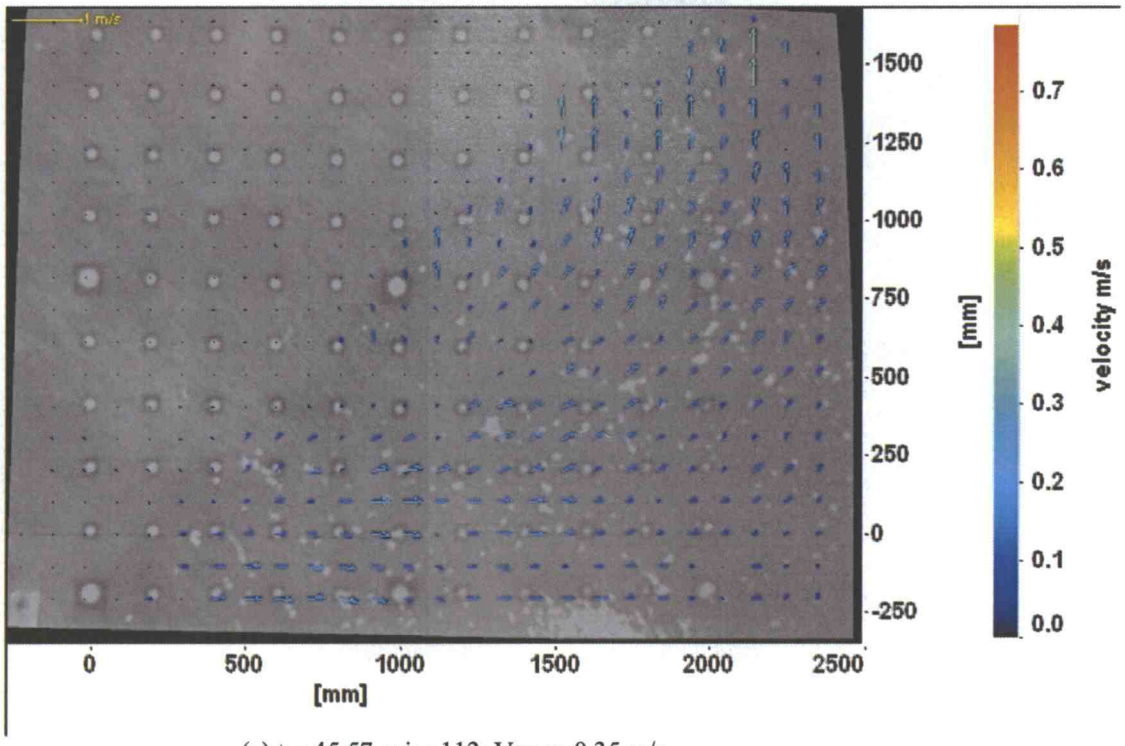

(c) t = 45.57 s; i = 112; Vmax=0.35 m/s

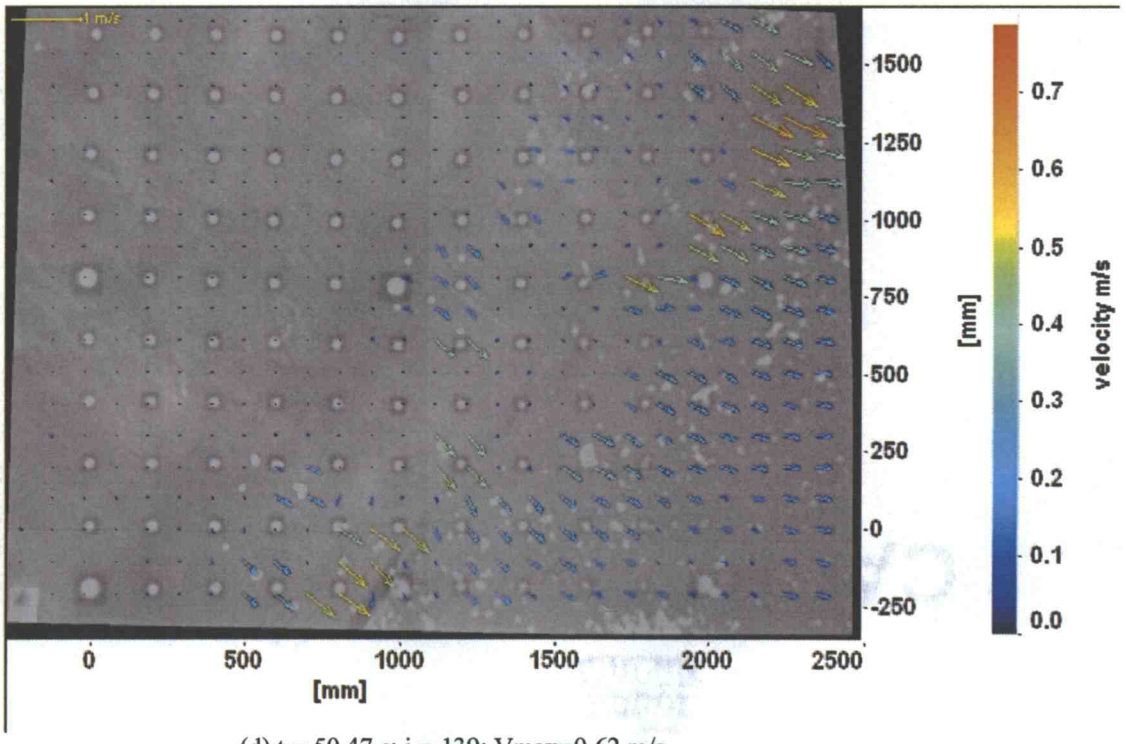

(d) t = 50.47 s; i = 139; Vmax=0.62 m/s

(2) Test 11 and 12 (D=55 cm, FOV=L-2 and L-3, Ho=4.44 cm)

Case 3 marked the maximum inundation level at the low foreshore, except for case 4 (over flooded case). Figure 53 (a) and (b) show the vector field for test 11 (i.e. FOV L-2). Figure 53(c) and (d) show the vector fields for test 12 (i.e. FOV L-3).

From Figure 53(a) to (d), it was observed that the run up direction was uniform. Since the bathymetry and topography was flat, wave reflection was not observed. However it was observed at the steep bluff section. Also the return flow was not observed for the test 11 and 12. Tracers carried by the wave finally stayed at the bathymetry/topography after the wave reached maximum inundation level. This is because the wave inundation at the low foreshore composed a very thin water film on the bathymetry/topography. The water depth of the film was too thin to carry 0.8 cm diameter tracers floating in the water. It can also be stated that return flow was not strong enough to carry the tracers back to offshore. Therefore, it was observed at the low foreshore that wave inundated to a larger extent relative to the steep bluff, and the return flow was not as strong as in the steep bluff region.

Now the wave inundation at the low foreshore compared to a real world scenario is discussed. From the previous observation, the person who is standing at the section should be aware of the first inundation of the wave. An observer should be prepared for flooding, since inundated water will remain without returning offshore.

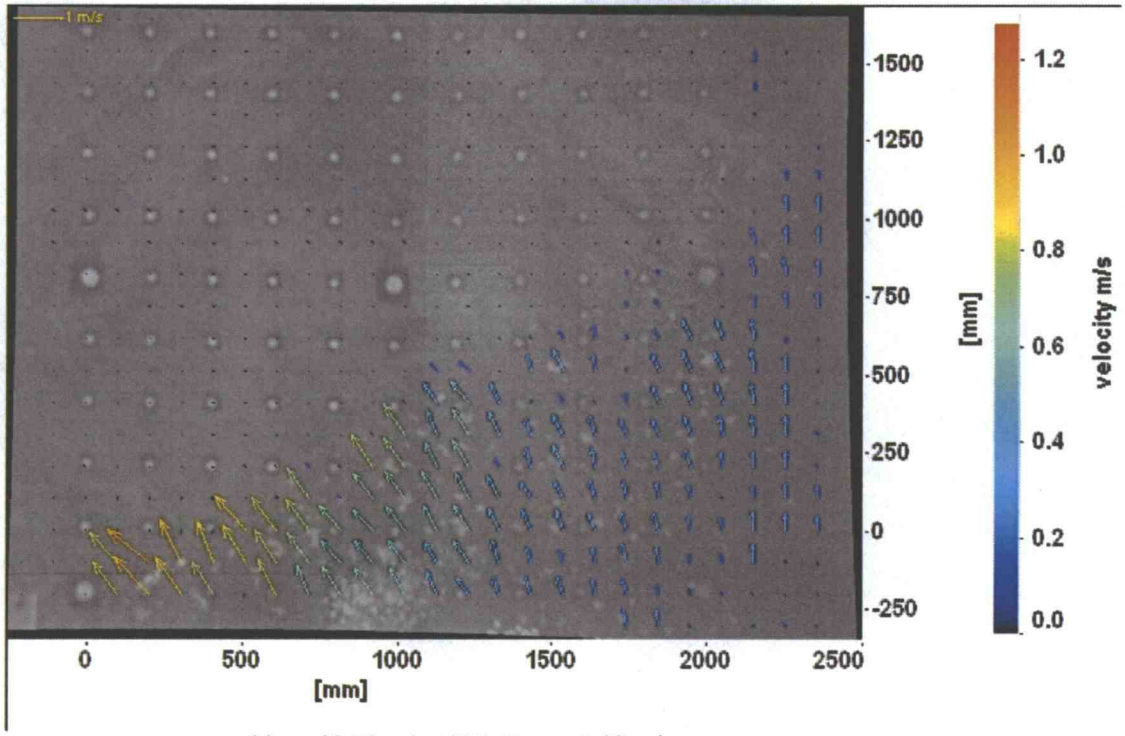

(a) t = 23.70 s; i = 117; Vmax=1.02 m/s

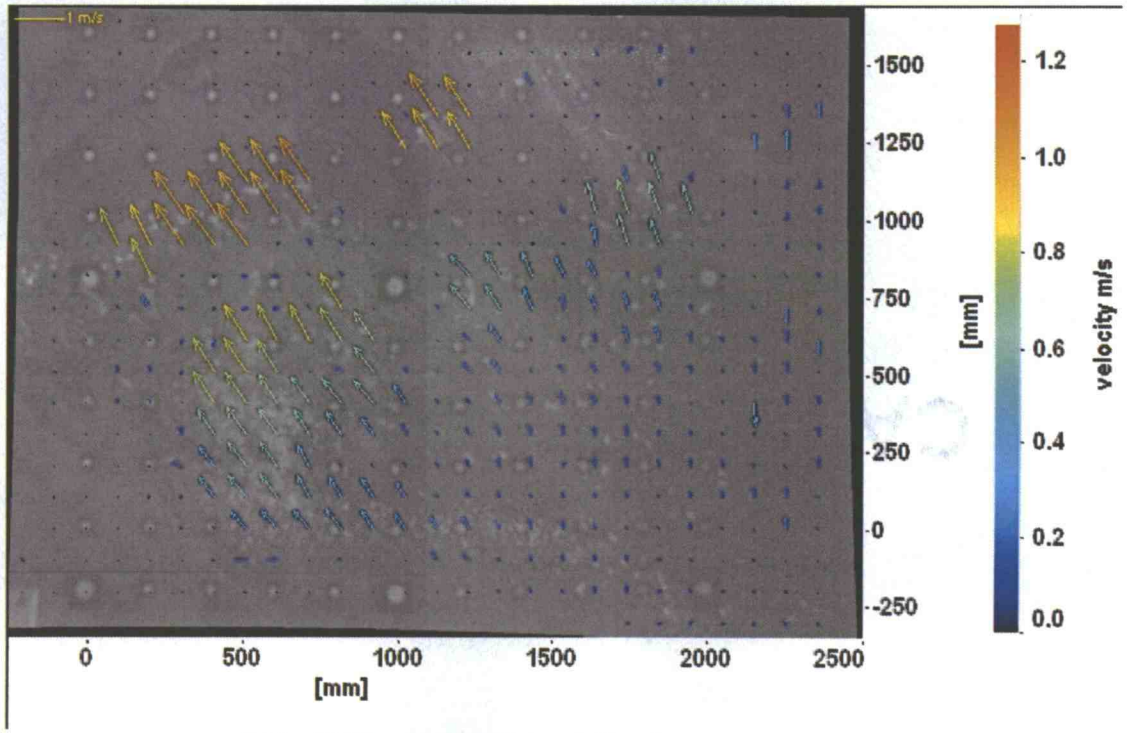

(b) t = 24.73 s; i = 148; Vmax=1.02 m/s

Figure 53: Vector field for test 11 and 12; low foreshore; D=55 cm; FOV=L-2; Ho=4.4 cm.

Figure 53 (continued, FOV=L-3)

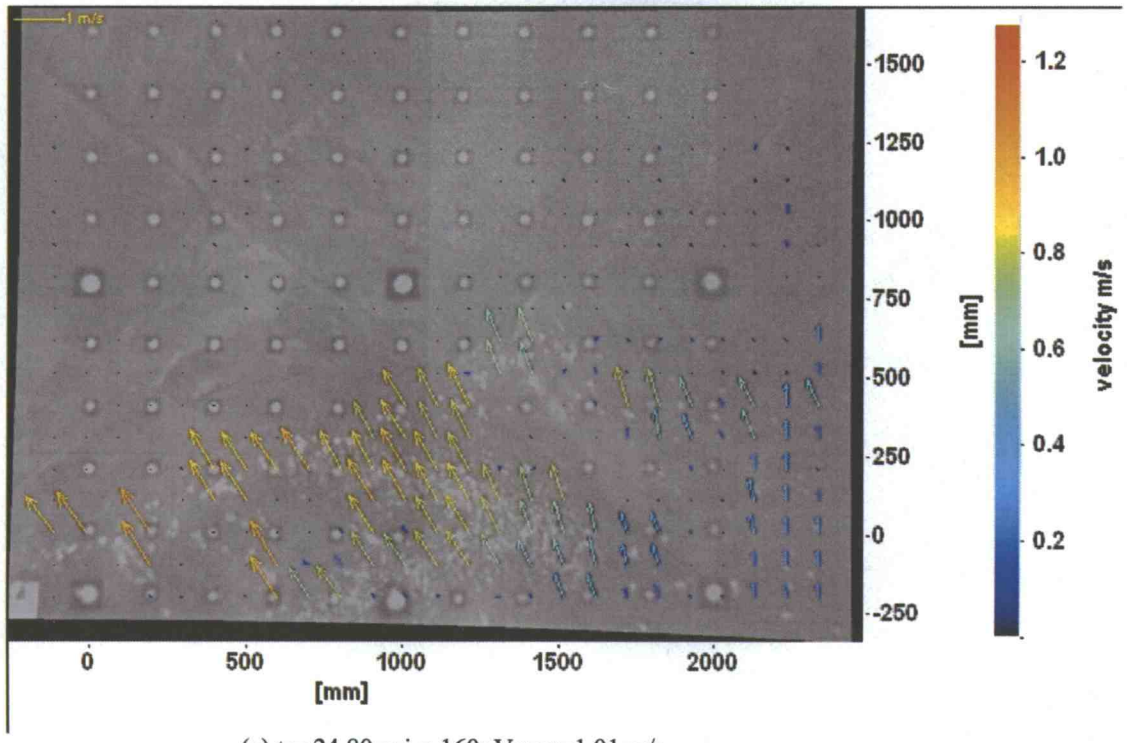

(c) t = 24.80 s; i = 160; Vmax=1.01 m/s

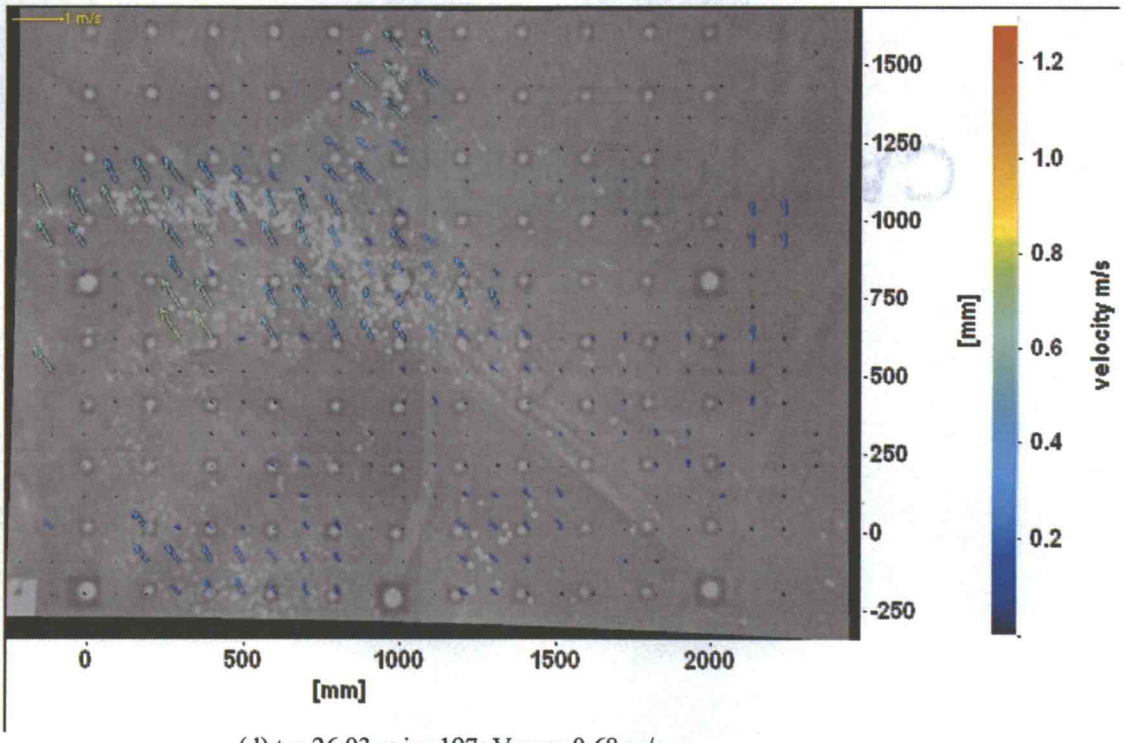

(d) t = 26.03 s; i = 197; Vmax=0.68 m/s

(3) Test 13 (D=55 cm, FOV=L-3, Ho=22.7 cm)

Figure 55 shows vector fields for test 13. A wave (Ho=22.7 cm) at the steep bluff section broke as a plunging breaker. On the other hand, the same wave profile at the low foreshore section was categorized as a surging wave. In general, surging wave occurs with waves of low steepness. In a surging wave, the base of the wave surges up the bathymetry face so that the crest collapses and disappears. Therefore, the wave did break, but the breaker point was hard to recognize in the low foreshore section. As a result, no major white water was observed from Figure 55 for the surging wave. Since no white water was recognized in the FOV, the resulting vector field was more reliable than others with plunging breakers. Most velocity vectors are found at the front part of a surging wave as shown in Figure 55(a). In addition, some vectors following the wave front were obtained as shown in Figure 55(b) to (d). It physically makes sense that the velocity at the wave front is the maximum and velocity following the wave is smaller. The results of test 13 are considered most reliable among all of the tests for case 4 since it was for surging breakers. Figure 54 shows the snap shot of the case 4 wave at the embayment and the low foreshore sections.

Figure 54: Wave propagation at the embayment and the low foreshore; Ho=22.7 cm.

Figure 54 shows that the wave was surging at the low foreshore and breaking at the embayment. The surging wave at the low foreshore section travel further than the breaking wave did at the embayment. This means that wave velocity at the low foreshore was larger than that of the embayment. Therefore, the wave velocity in test 13 should be larger that of test 19. The results will be compared in chapter 5.1.4.

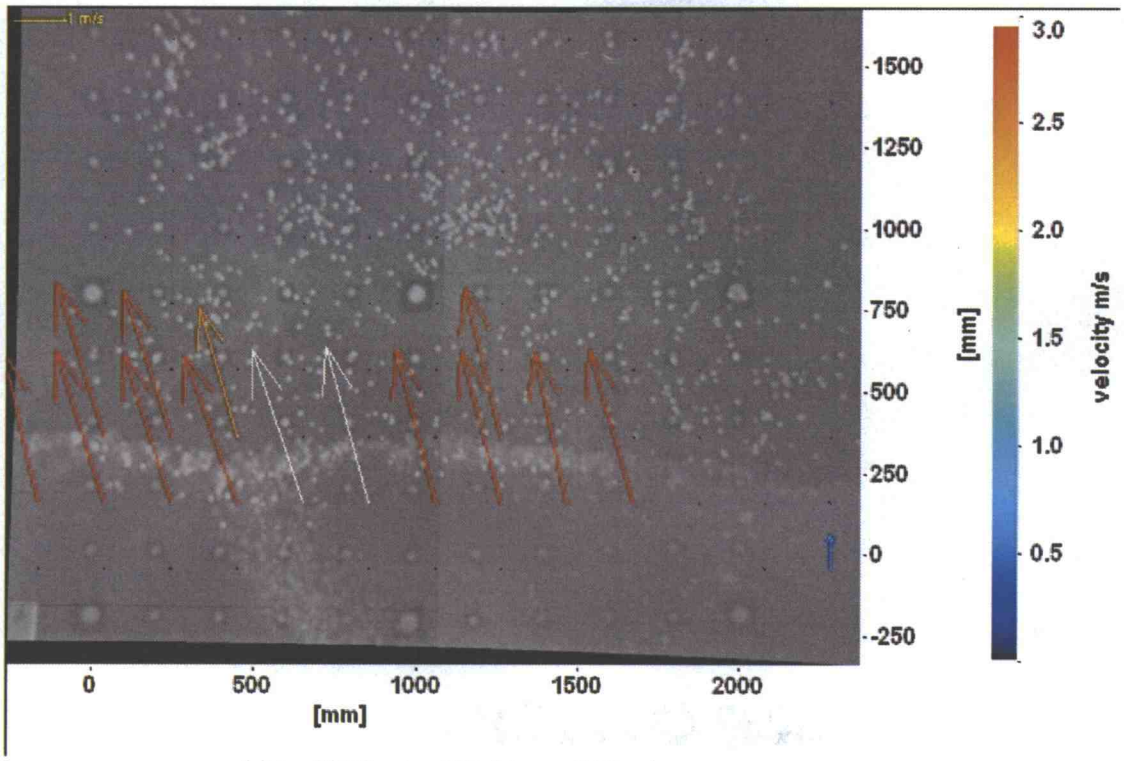

(a) t = 29.70 s; i = 100; Vmax=2.98 m/s

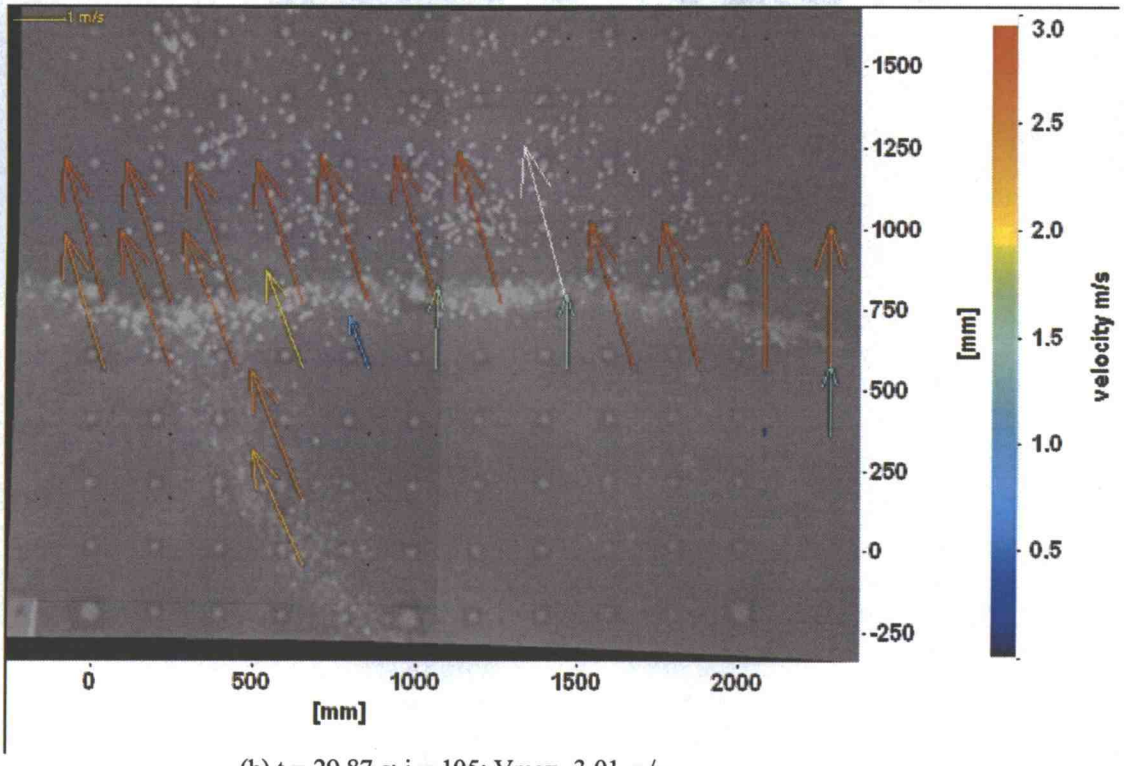

(b) t = 29.87 s; i = 105; Vmax=3.01 m/s

Figure 55: Vector field for test 13; low foreshore; D=55 cm; FOV=L-3; Ho=22.7 cm.

Figure 55(continued)

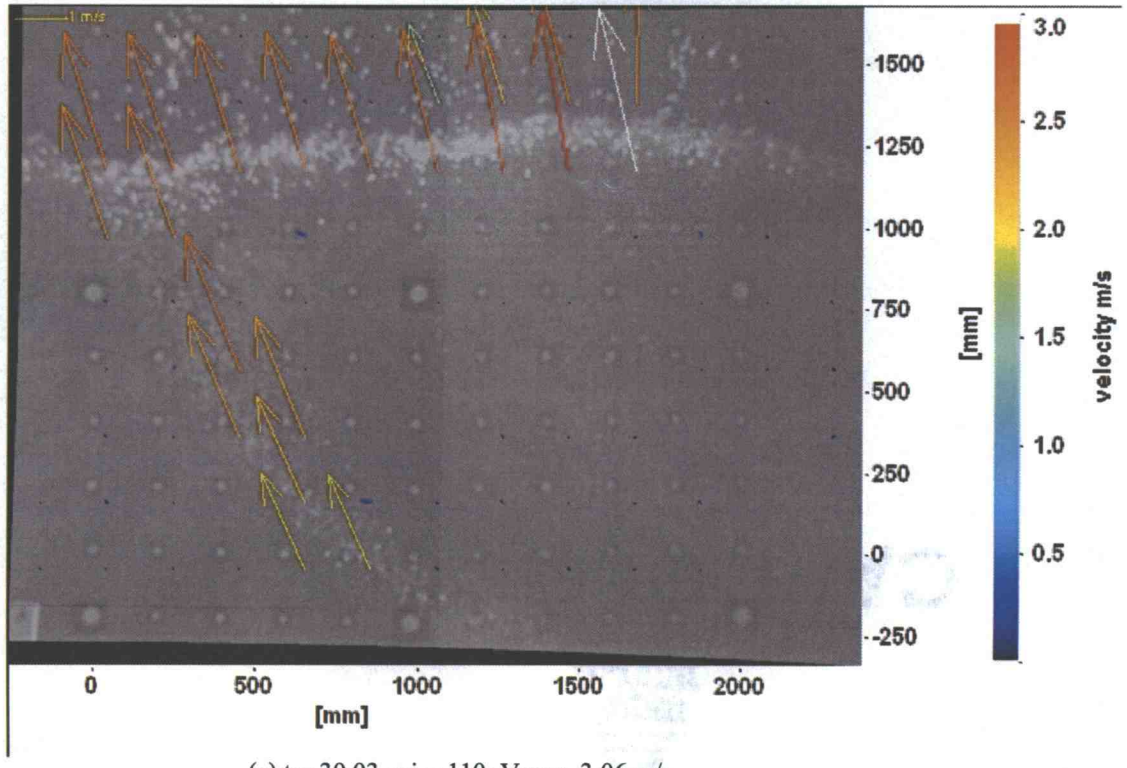

(c) t = 30.03 s; i = 110; Vmax=3.06 m/s

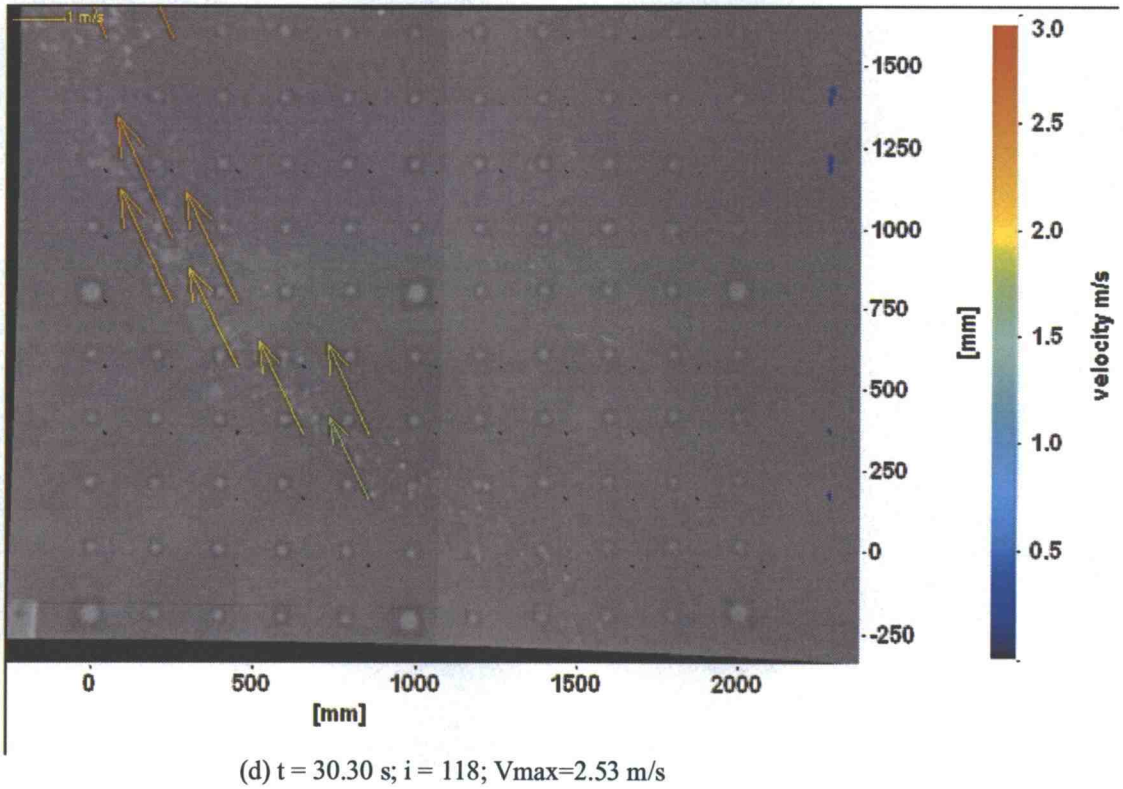

(d) t = 30.30 s; i = 118; Vmax=2.53 m/s

5.1.4 PIV results at the embayment

(1) Test 15 and 17 (D=44 cm, Ho=7.93 cm, FOV=E-1 and E-2)

Figure 56(a) and (b) show the vector fields for test 15 (i.e. FOV E-1). Figure 56(c) and (d) show the vector fields for test 17 (i.e. FOV E-2).

The embayment section was the shallow water area. The water depths were 2.7 cm and 13.7 cm for the offshore water depth of 44 cm and 55 cm, respectively. The bottom profile at the embayment section was flat (i.e. uniform water depth over the section). From these points, the embayment section had quite different characteristics from the steep bluff and the low foreshore section.

The wave started breaking when it entered the FOV E-1(i.e. shallow water depth). This wave compared to a bore in a real world scenario. Since the section was surrounded by high boundaries, the wave propagating onshore direction was affected by the boundaries. This can be observed well in Figure 56(b). Due to the boundary and the bore, the vector field was relatively noisy manner for this case. At the embayment, most tracers were put on the water surface before starting the wavemaker. No remarkable velocity change was observed as the wave propagated through the FOV. This may be explained by the flat bathymetry of this section.

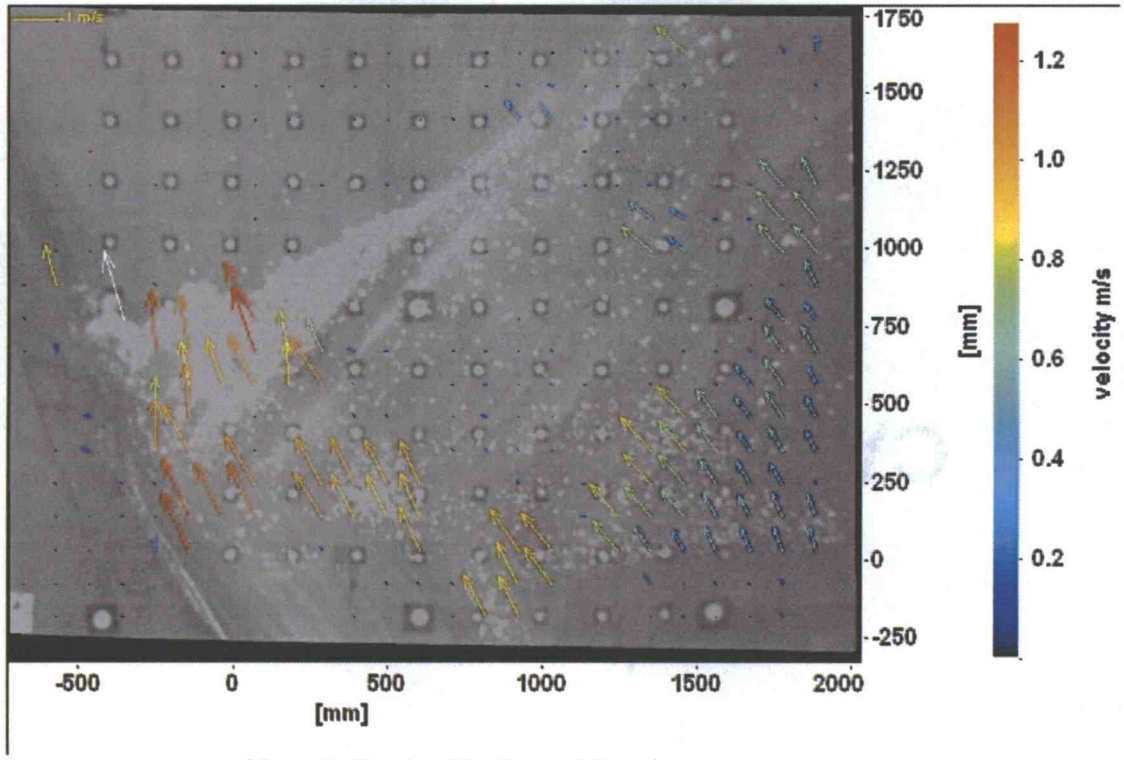

(a) t = 47.43 s; i = 185; Vmax=1.35 m/s

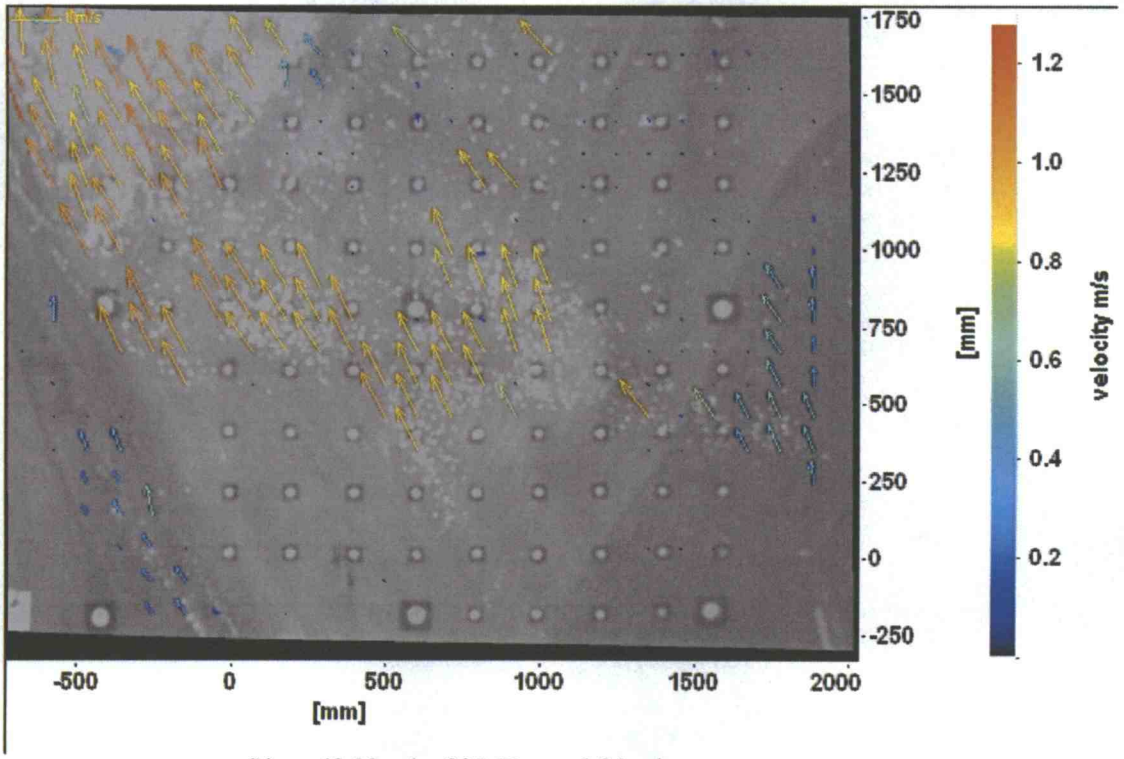

(b) t = 48.09 s; i = 205; Vmax=1.24 m/s

Figure 56: Vector field for test 15 and 17; embayment; D=44 cm; FOV=E-1; Ho=4.5 cm.

Figure 56 (continued, FOV=E-1)

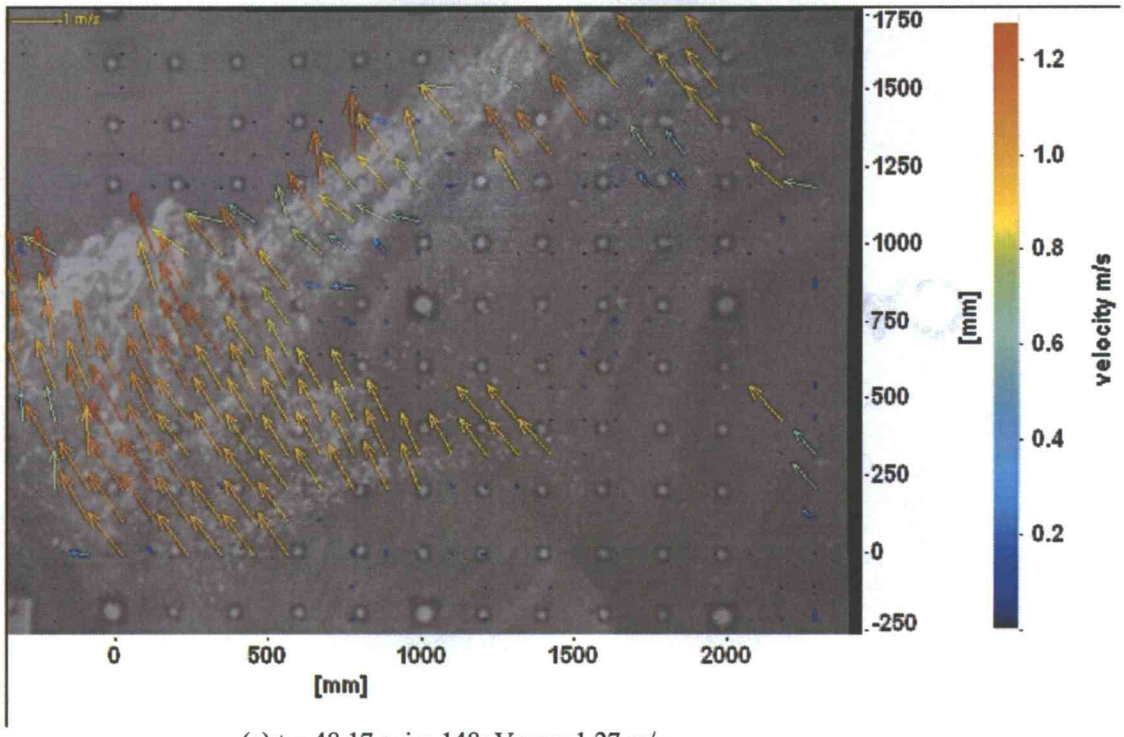

(c) t = 48.17 s; i = 148; Vmax=1.27 m/s

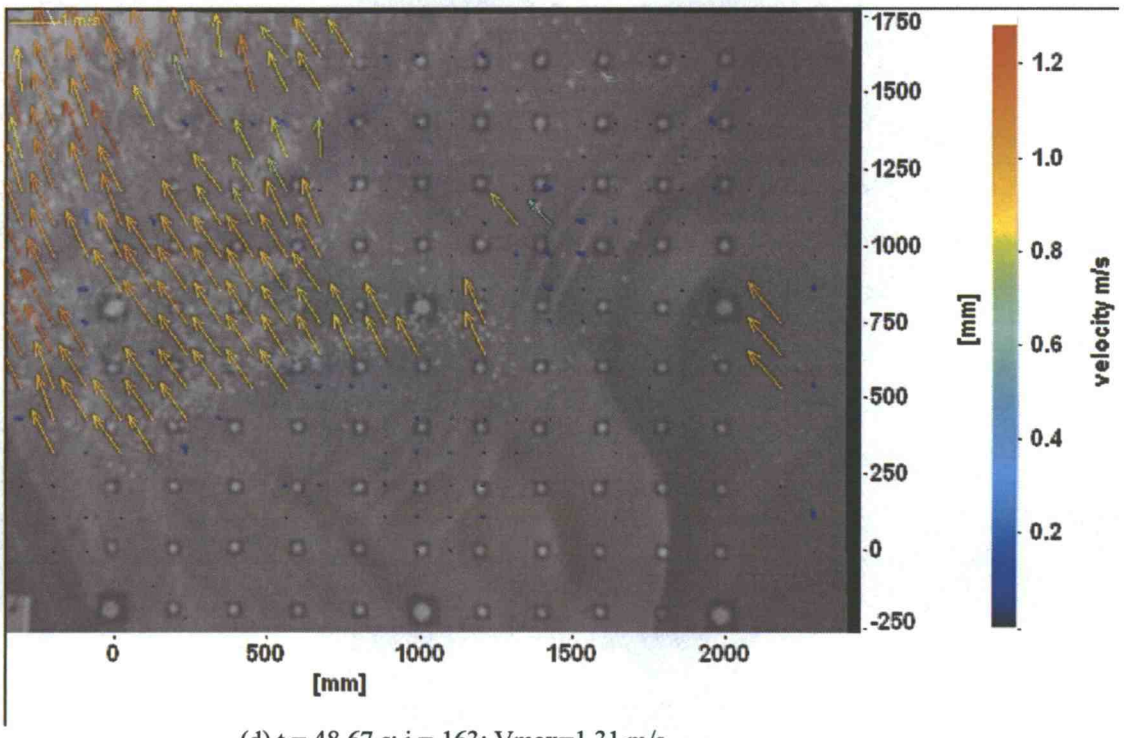

(d) t = 48.67 s; i = 163; Vmax=1.31 m/s

(2) Test 18 and 20 (D=55 cm, FOV=E-1 and E-2, Ho=4.4 cm)

Figure 57 (a) and (b) show the vector fields for test 18 (i.e FOV E-1). Figure 57 (c) and (d) show the vector fields for test 20 (i.e. FOV E-2).

The wave was propagating through the FOV without breaking. The wave velocities in Figure 57 are relatively small compared to other tests and also have uniform direction. The propagating wave was reflected by the steep wall (boundary) then formed a return flow as shown in Figure 57(e). After the recording of the return flow was conducted, the PIV time series was synchronized using the time series of LED and wave gage. It can be observed that the return flow was as strong as the incoming flow. However, the return flow showed a complicated manner. The wave crests in Figure 57(e) propagated toward the inside of the embayment. The interference of incoming and outgoing flow prevented most tracers moving toward outside of the embayment. Finally, tracers stayed at the same locations.

The comparisons with ADV data is conducted for the PIV time series for this test. The results will be discussed following chapter 5.2.

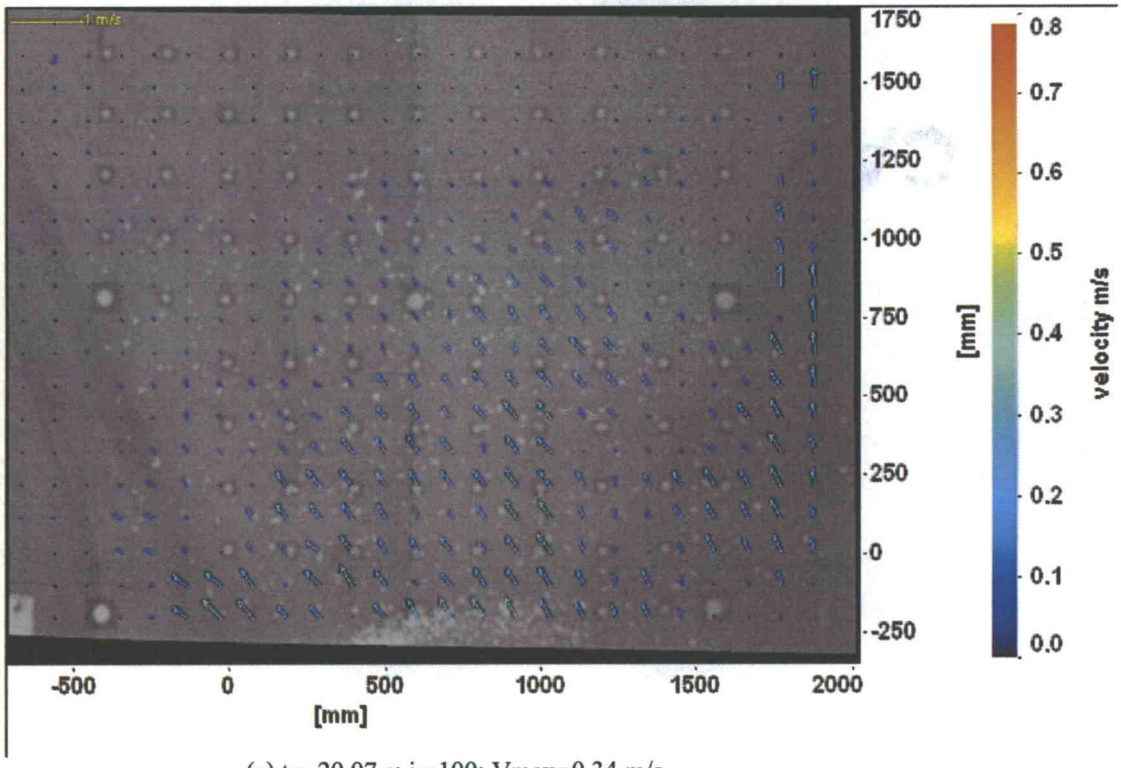

(a) t = 20.07 s; i =100; Vmax=0.34 m/s

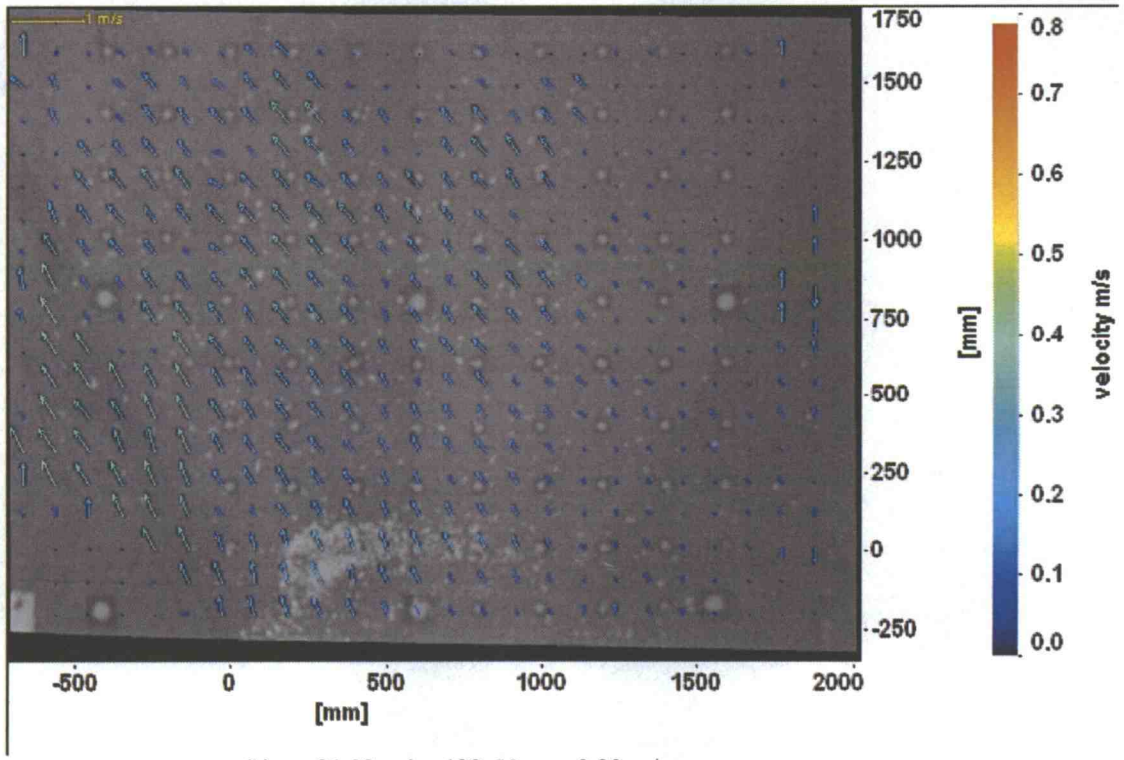

(b) t = 21.03 s; i = 129; Vmax=0.39 m/s

Figure 57: Vector field for test 18 and 20; embayment; D=55 cm; FOV=E-1; Ho=4.4 cm.

Figure 57(continued, FOV=E-2)

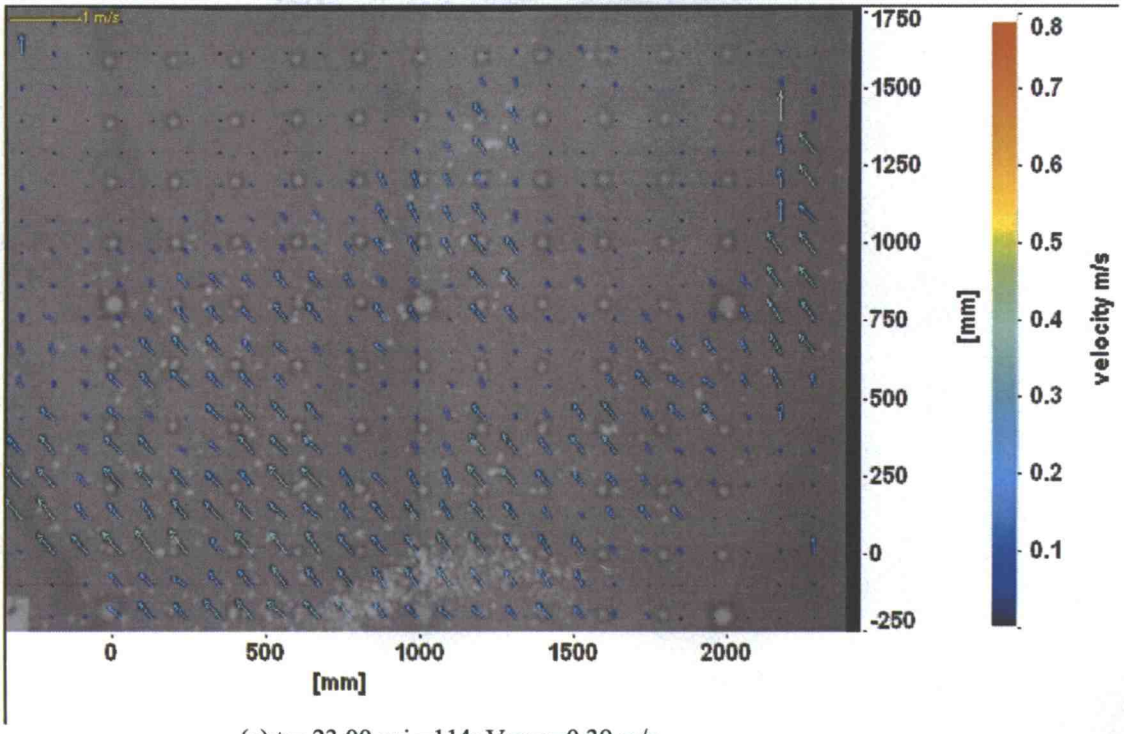

(c) t = 23.00 s; i =114; Vmax=0.39 m/s

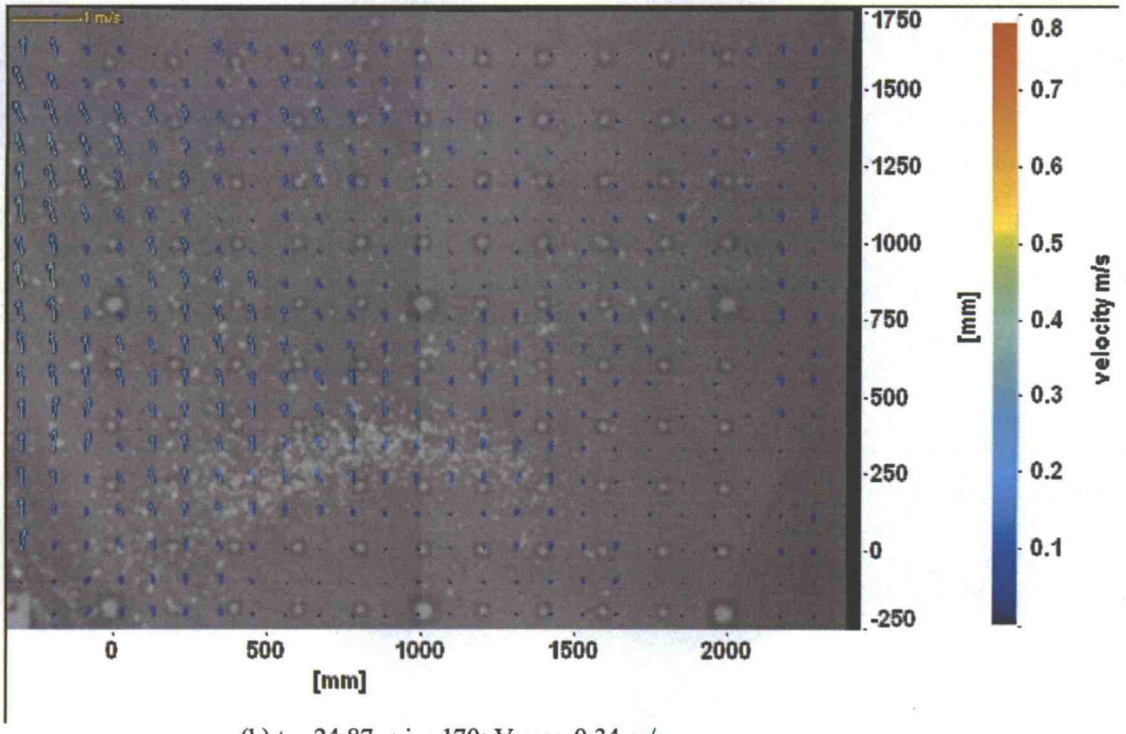

(b) t = 24.87 s; i = 170; Vmax=0.34 m/s

Figure 57(continued, FOV=E-2)

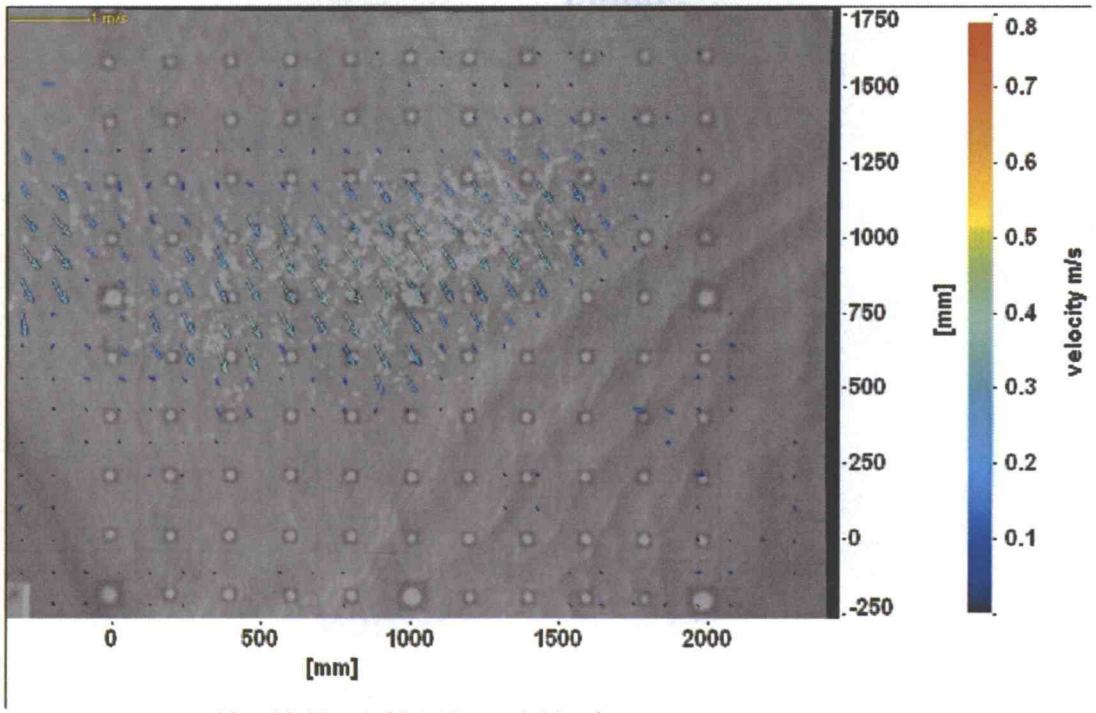

(e) t=33.97 s; i=206; Vmax=0.38 m/s

(3) Test 19 (D=55 cm, FOV=E-1, Ho=22.7 cm)

Velocity vectors at the embayment were generally noisier than those of other sections. This trend also holds for wave case 4. Figure 58 shows vector fields for test 19. The wave type can be categorized as a plunging wave. The white water covering the tracers was observed, and the PIV seemed to detect these as tracers as was seen in test 5. Since the vectors at the white water have some uncertainty, there are some ways to analyze the accuracy of the data. First, as seen from the video recorded for the case, the velocity at the embayment was definitely smaller than that of the low foreshore. Comparing the velocity fields of test 19 with test 13, it was confirmed that the velocity of test 19 was smaller that that of test 13. Second, there were some vectors calculated from the tracers in Figure 58 (c) and (d). These velocities were smaller than those at white water area, which hold for the physical properties of velocity distributions. The results from test 19 were also used for comparison with ADV data in the next section. Vector fields for other tests are in Appendix D.

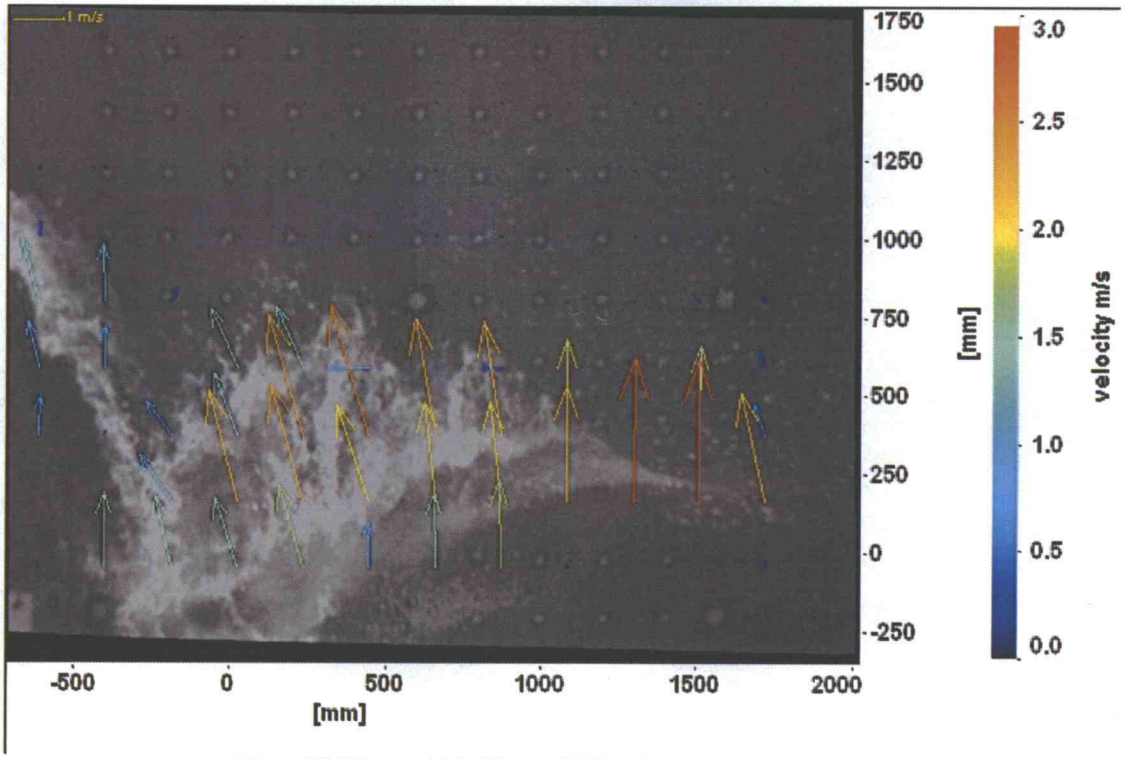

(a) t = 17.07 s; i =104; Vmax=2.77 m/s

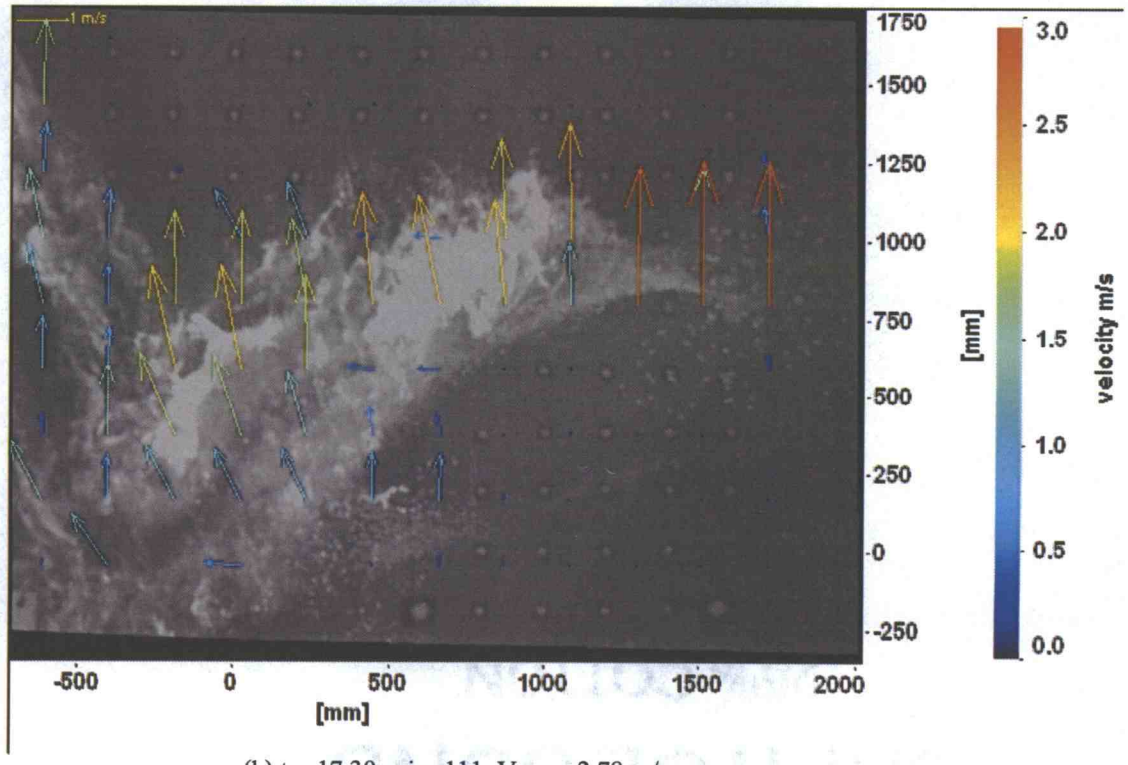

(b) t = 17.30 s; i = 111; Vmax=2.78 m/s

Figure 58: Vector field for test 19; embayment; D=55 cm; FOV=E-1; Ho=22.7 cm.

Figure 58 (continued)

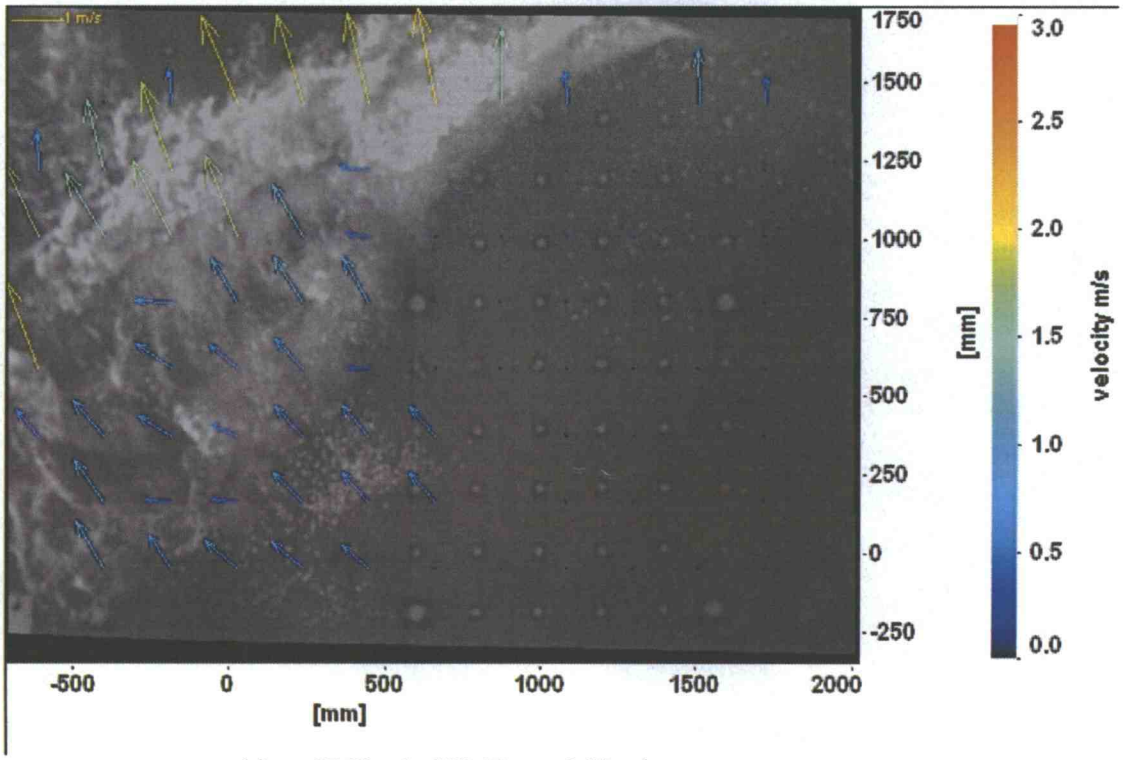

(c) t = 17.60 s; i =120; Vmax=1.93 m/s

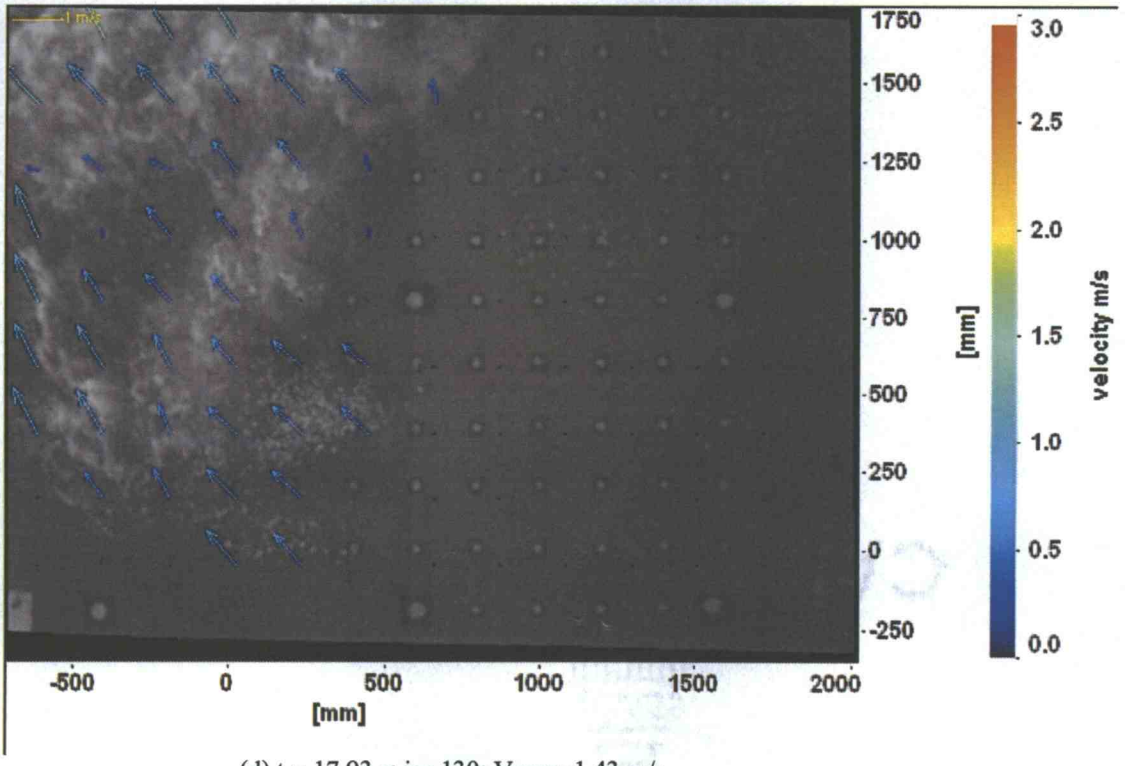

(d) t = 17.93 s; i = 130; Vmax=1.43 m/s

5.2 Comparison between ADV and PIV data at the embayment section

The velocity data of test 18(D=55 cm, FOV=E-1, Ho=4.4 cm) and 19(D=55 cm, FOV=E-1, Ho=22.7 cm) were compared with the ADV data. The ADV locations were at X=18, 19 and 17 m with Y=16 m. The local vector fields were picked up by selecting interrogation windows corresponding to the ADV locations. For test 18, the local velocities at 2 x 2 interrogation windows were extracted to compare with ADV data. In Figure 59, the scalar field of the velocity in the along tank direction (Vy) was overlaid on vector fields. Each square of scalar field was fit in an interrogation window (i.e. identical to interrogation window size). It was confirmed that each vector was on each interrogation window. Since the FOV was divided into the interrogation window, which is the smallest element to calculate velocity, the exact location of the ADV measurements can not be chosen. Therefore, the 2 x 2 interrogation windows including each measured location by ADV were chosen. The white dots surrounded by the square (1), (2) and (3) in Figure 59 are located at X=18, 19 and 17 m with Y=16 m.

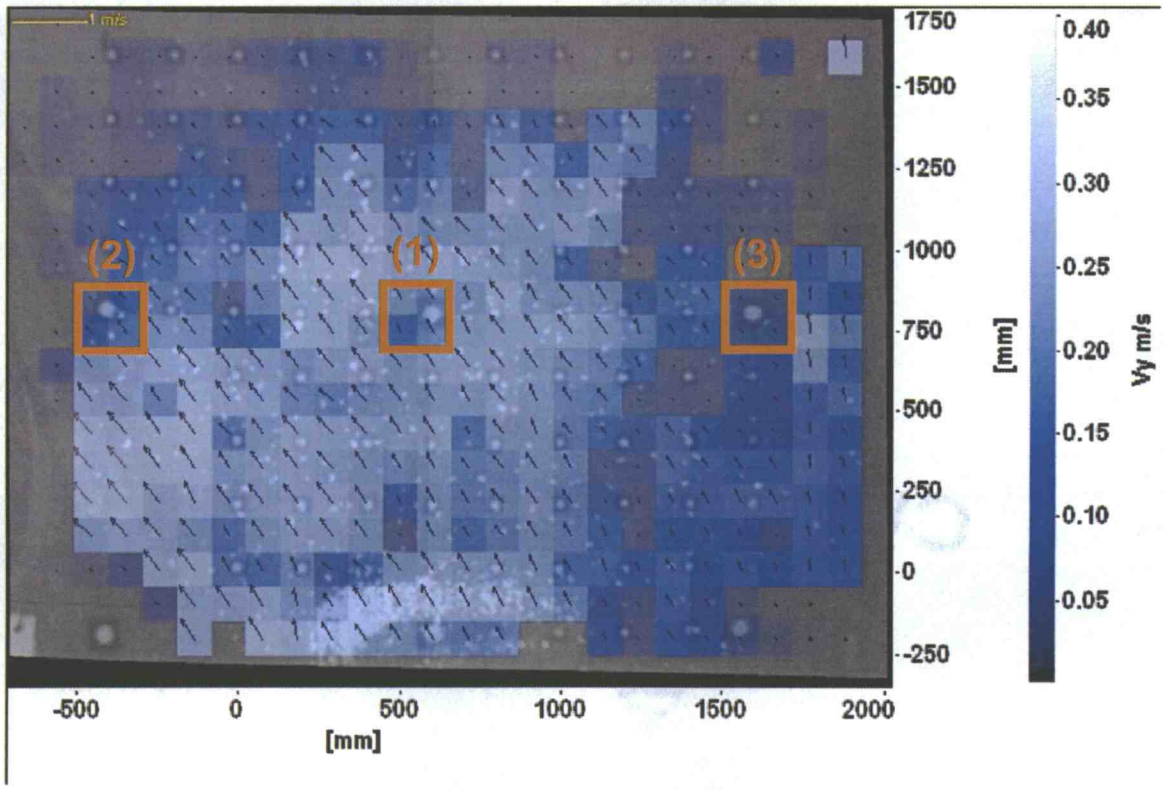

Figure 59: Three locations for ADV and PIV comparison for test 18.

After the local velocity, Vy, was calculated at each square in Figure 59, the PIV local velocities were synchronized with ADV data using the time series for the ADV and the wave gages, and the LED and the wave gages, respectively. It is worth noting that the comparison of velocities of the ADV and the PIV was based on the idea that the ADV is more accurate than PIV for the following reasons:

First, the PIV measurements were conducted for the first time in the Tsunami Wave Basin while ADV measurements have been conducted many times prior. Second, the PIV measurements were sensitive to many factors as mentioned in chapter 4.2. The ADV measurements were reliable as long as they were conducted in properly seeded water while keeping the proper water depth beneath the probes. Third, the sampling rate of the ADV was 50 Hz which was higher than that of the PIV, which was 30Hz.

Figure 60 shows the results of comparing Vy for the ADV and the PIV test 18 (D=55 cm, FOV=E-1, Ho=4.4 cm). In Figure 60(a), at X=18 m and Y=16 m, Vy of the ADV was slightly larger than that of PIV. Velocities in the time series showed very similar profile. However in Figure 60(b), X=19 m and Y=16 m, Vy of ADV was slightly smaller than that of the PIV and the velocities in time series of PIV were slightly out of phase from that of the ADV. In Figure 60(c), at X=17 m and Y=16 m, Vy of PIV showed a noisy profile. However the peak velocity profile showed good agreement with that of the ADV. These noises may have been caused by fewer tracers in a selected area. In general, Vy of PIV shows good agreement with that of ADV.

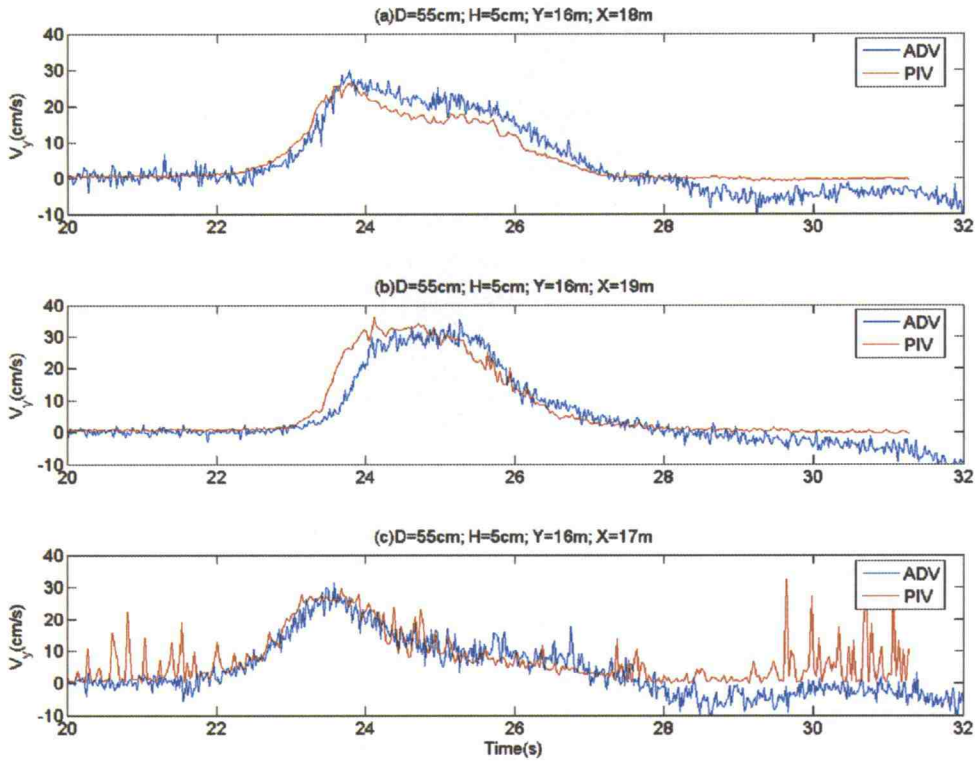

Figure 60: Comparisons of the timeseries for ADV and PIV; case 3.

Figure 61 shows three locations for the comparisons for Test 19. Figure 62 results of comparing of Vy for the ADV and the PIV for test 19 (D=55 cm, FOV=E-1, Ho=22.7 cm). The velocity for the ADV and the PIV shows different mannerisms in both the profile and the time of peak occurrence for this case. Some possible causes are considered for this. Ho=22.7 cm wave had already broken as it entered FOV E-1. The magnitude of velocity of the PIV generally shows good agreements to those of the ADV for the comparisons in Figure 60 (previous case). However, the Vy of the PIV was much larger than that of ADV for this case. As mentioned before, PIV seemed to mostly detect not tracers but white water from the breaking wave. On the other hand, the ADV measured the water particle velocity below water surface, which was in non-breaking condition. This may be the reason why the velocity by the PIV was larger than that of the ADV.

The velocity distribution in shallow water condition was uniform along the water depth. It can also be seen from Figure 60 that the water particle velocity at the water surface by the PIV showed good agreements with the velocity below the water surface by the ADV. It should be noted that either at the water surface or below the water surface, the wave was not breaking for the previous case. However, for test 19, the PIV measured white water particles on the water surface and the ADV measured the water particle velocity at non-breaking condition since it was below the water surface. Further discussion about the PIV accuracy for the braking wave is in Appendix E.

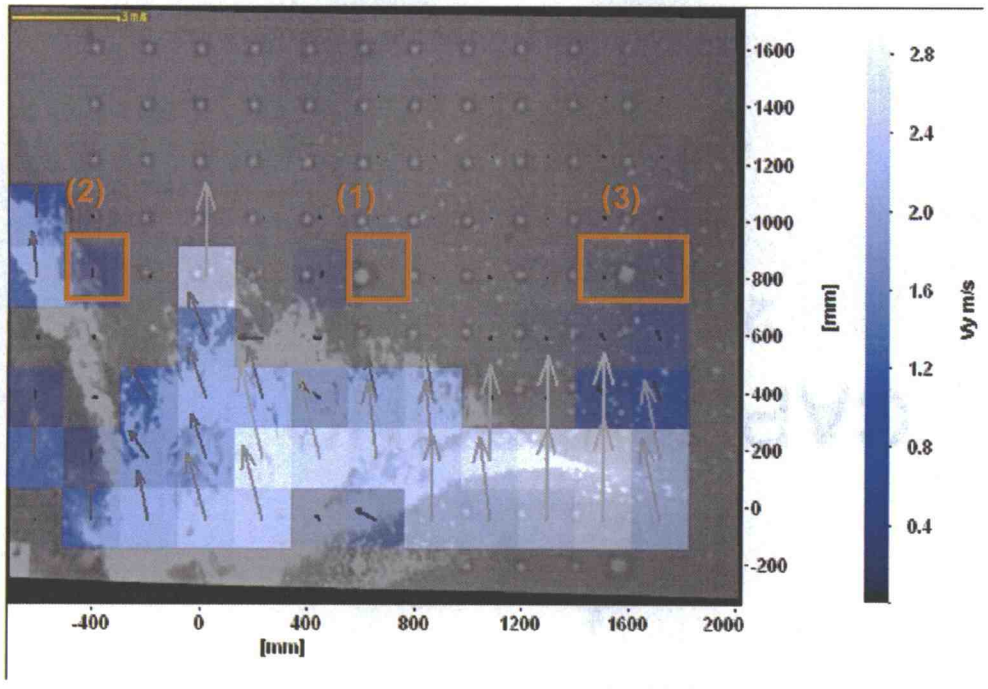

Figure 61: Three locations for ADV and PIV comparison for test 19.

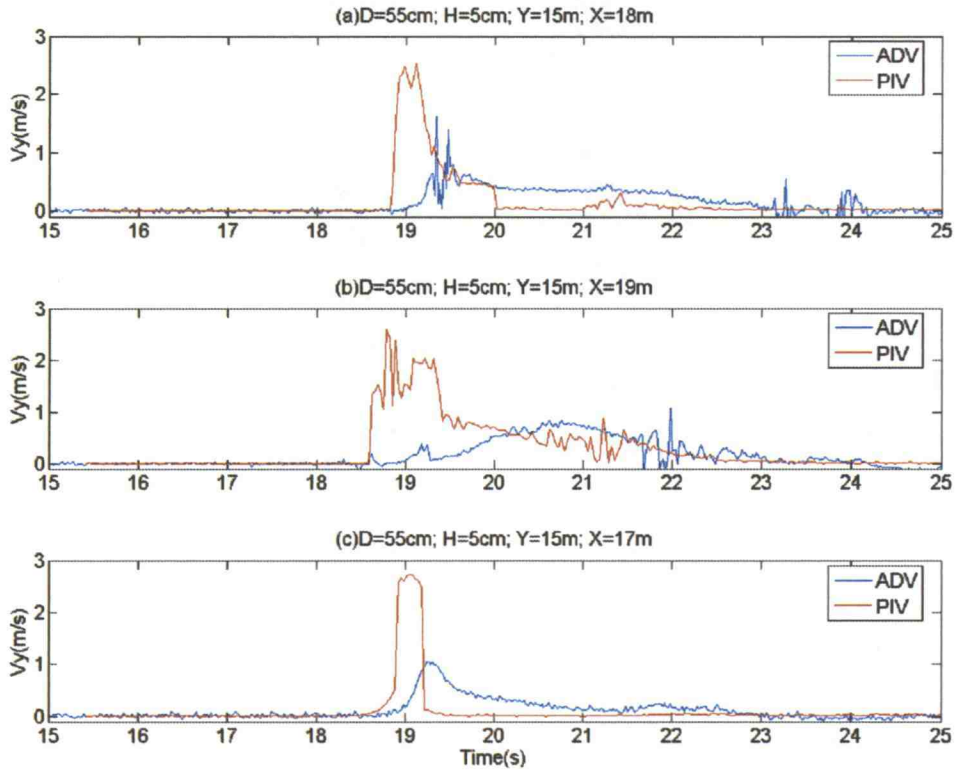

Figure 62: Comparisons of the timeseries for ADV and PIV; case 4.

6. Conclusion

This work presents one of the first experiments to provide comprehensive laboratory measurements of tsunami inundation over a complex 3D bathymetry. Four cases were run at two different water depths to provide several conditions including non-breaking waves, breaking waves, conditions in which the mass is conserved on the model, and conditions in which there is strong overtopping of the model.

Three sections of the model were studied in detail, including a steep bluff, low foreshore, and shallow embayment which are representative of features commonly found in coastal areas. At the steep bluff section, the tsunami was observed to have strong runup and rundown patterns. The run down velocity was observed to be as large as the runup velocity. At the low foreshore section, the characteristics of the runup/run down were distinctly different, and the rundown itself could not be observed easily. At the embayment section, both breaking and non-breaking waves were observed.

A procedure for measuring tsunami inundation velocities using a commercial particle image velocimetry (PIV) system was developed and documented in this report. This procedure included developing a synchronization mechanism, determining appropriate seeding and light levels, image calibration and calculation of horizontal velocity vectors. In situ comparisons with acoustic Doppler velocimetry measurements showed good agreement for the case of non-breaking waves. For the case of breaking waves, the brightness of the bore made PIV measurements difficult.

Appendix A

Reference grid at the embayment and the low foreshore

Figure A. 1: Reference grid at the embayment.

Figure A. 2: Reference grid at the low foreshore.

Appendix B

Observed Maximum inundation at the steep bluff and the low foreshore

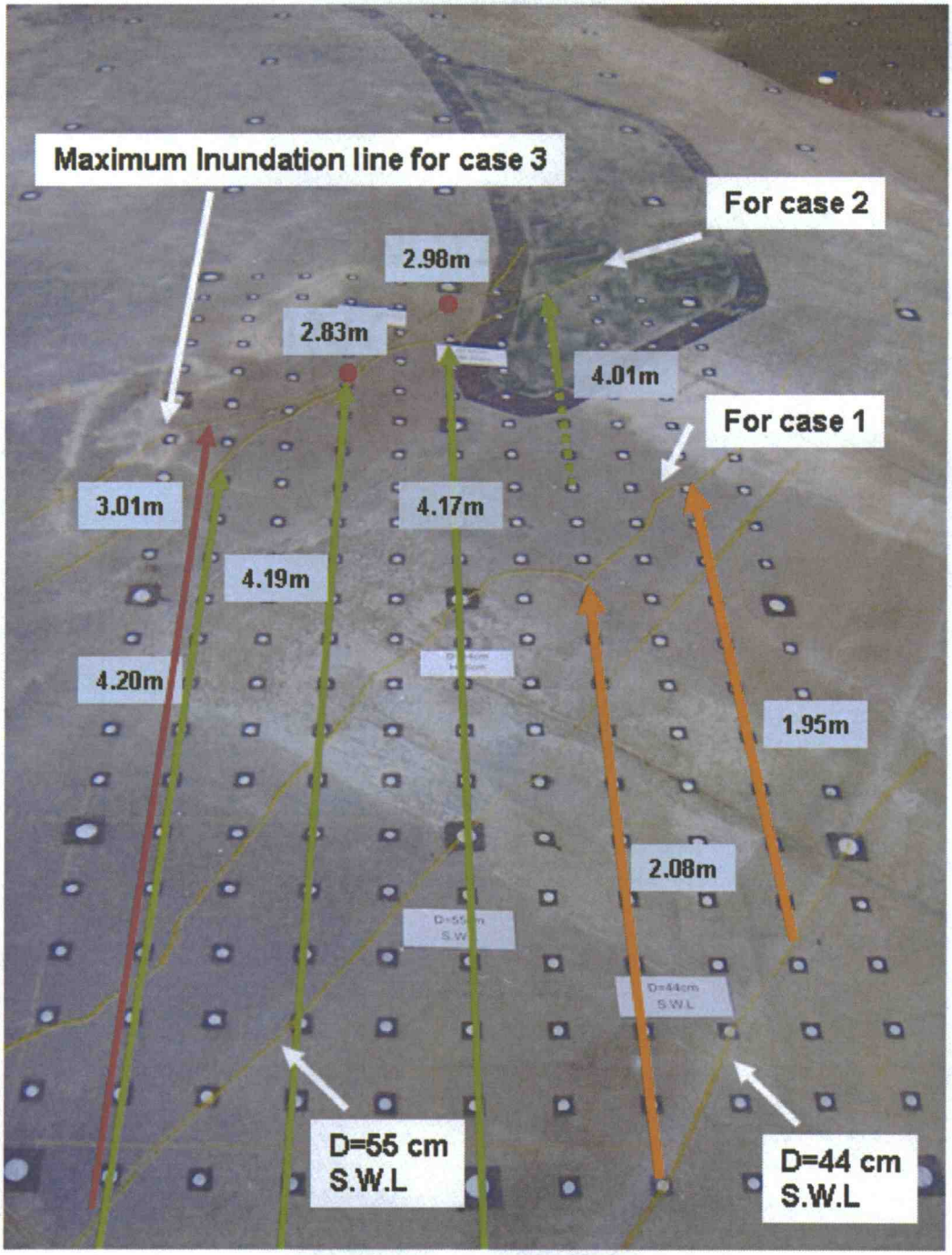

Figure B. 1: Observed maximum inundation at the steep bluff.

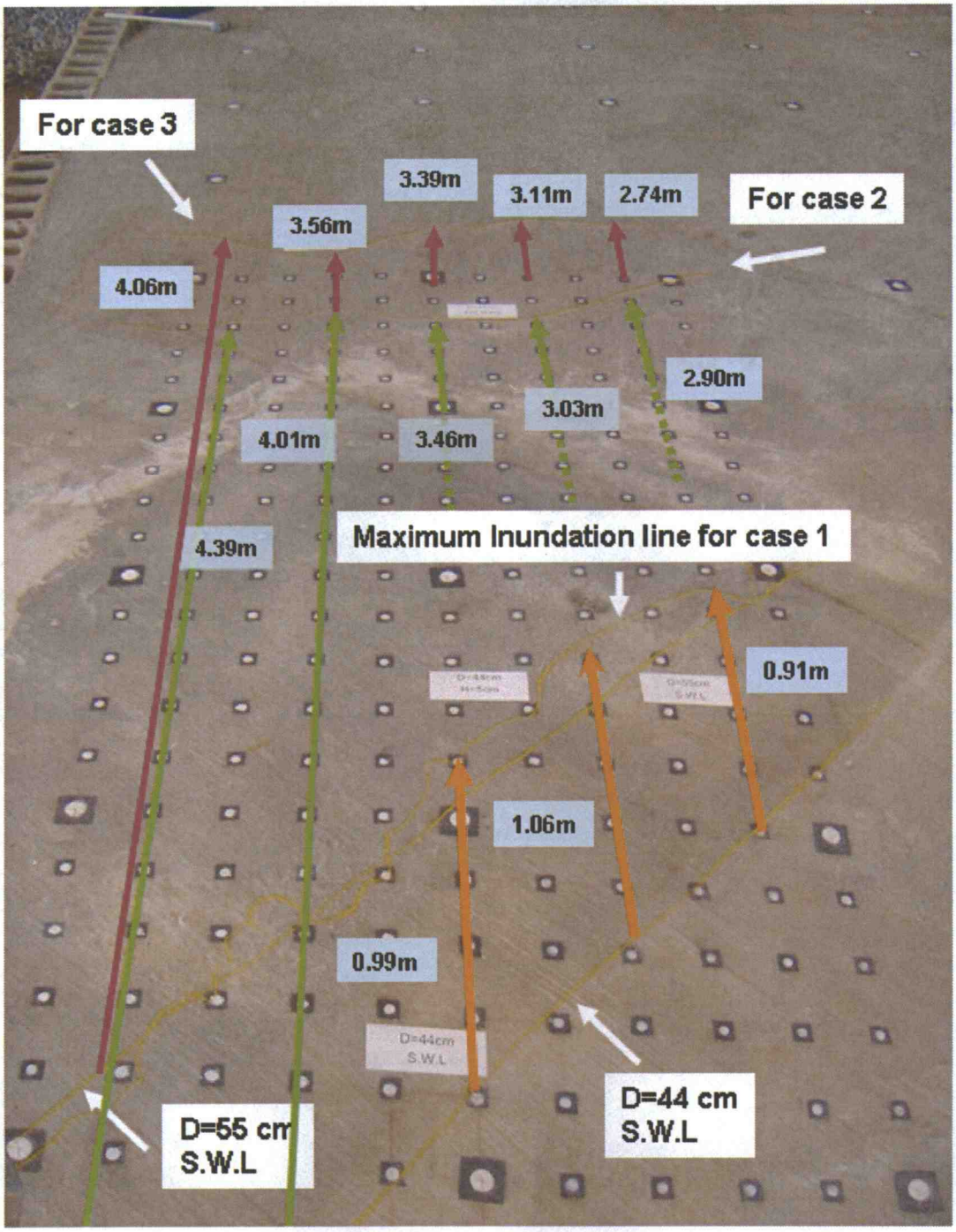

Figure B. 2: Observed maximum inundation at the low foreshore.

Appendix C

Time series of the LED and wave gage for each test

Table C. 1: Time series of LED and weave gage.

Test Num.	t_W (sec)	t_L (sec)	i_L
1	5.37	11.50	53
2	33.77	39.70	30
3	34.17	40.30	28
4	34.00	41.13	19
5	5.47	11.27	44
6	7.13	13.97	19
7	7.17	14.37	19
8	33.77	46.90	32
9	36.37	45.73	47
10	42.30	52.90	53
11	9.8	21.7	57
12	9.5	20.87	51
13	17.53	27.53	35
14	5.67	15.83	51
15	35.60	42.27	30
16	7.00	19.13	29
17	34.9	43.60	32
18	7.77	17.63	27
19	6.93	14.90	39
20	5.77	18.50	39

t_W = time of maximum water surface elevation

t_L = time at the transition point of LED

i_L = image index of PIV at the transition point

Appendix D

PIV time series for each test

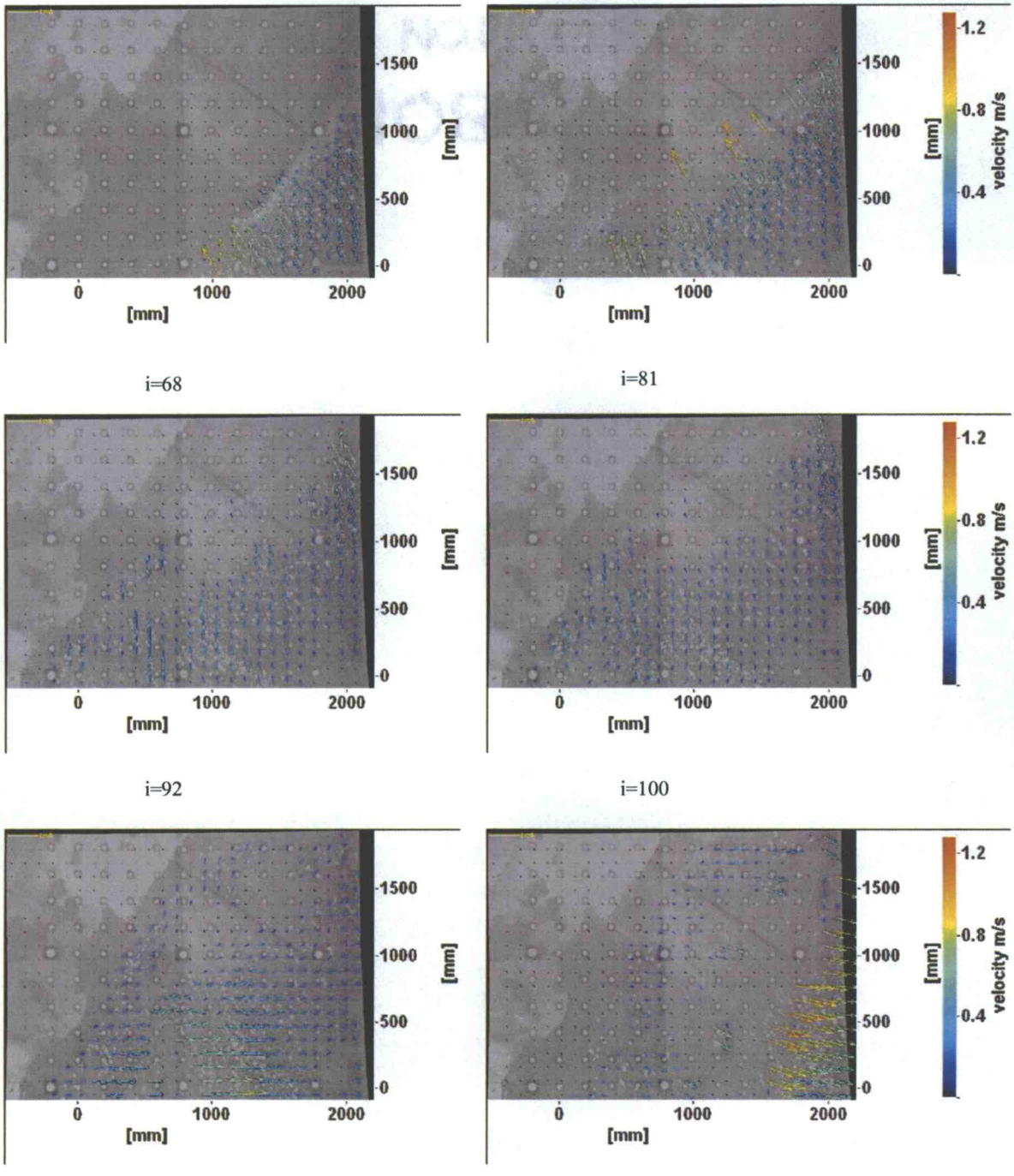

i=68 i=81

i=92 i=100

i=119 i=150

Figure D. 1: Vector field for test 1.

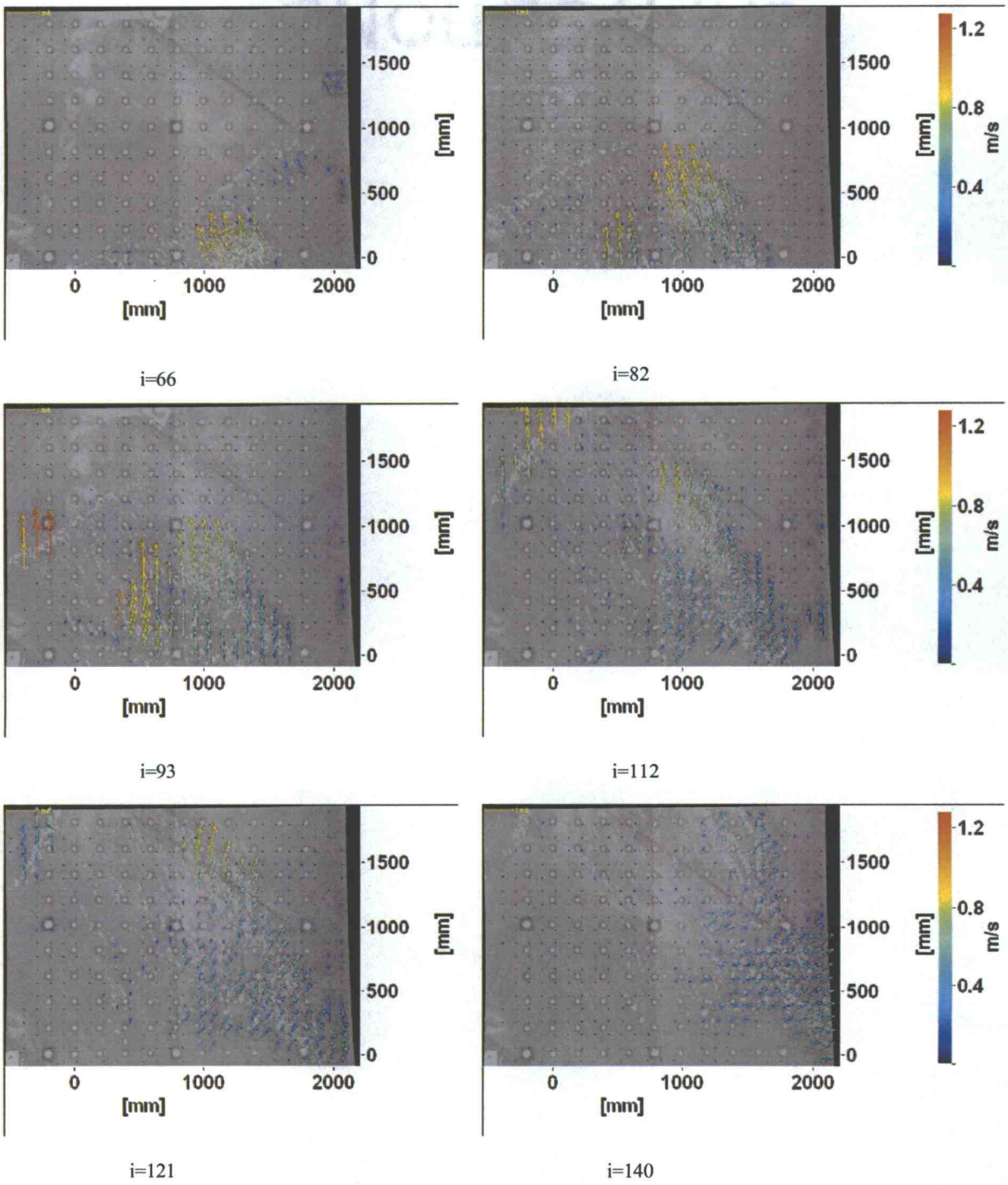

i=66 i=82

i=93 i=112

i=121 i=140

Figure D. 2: Vector field for test 2.

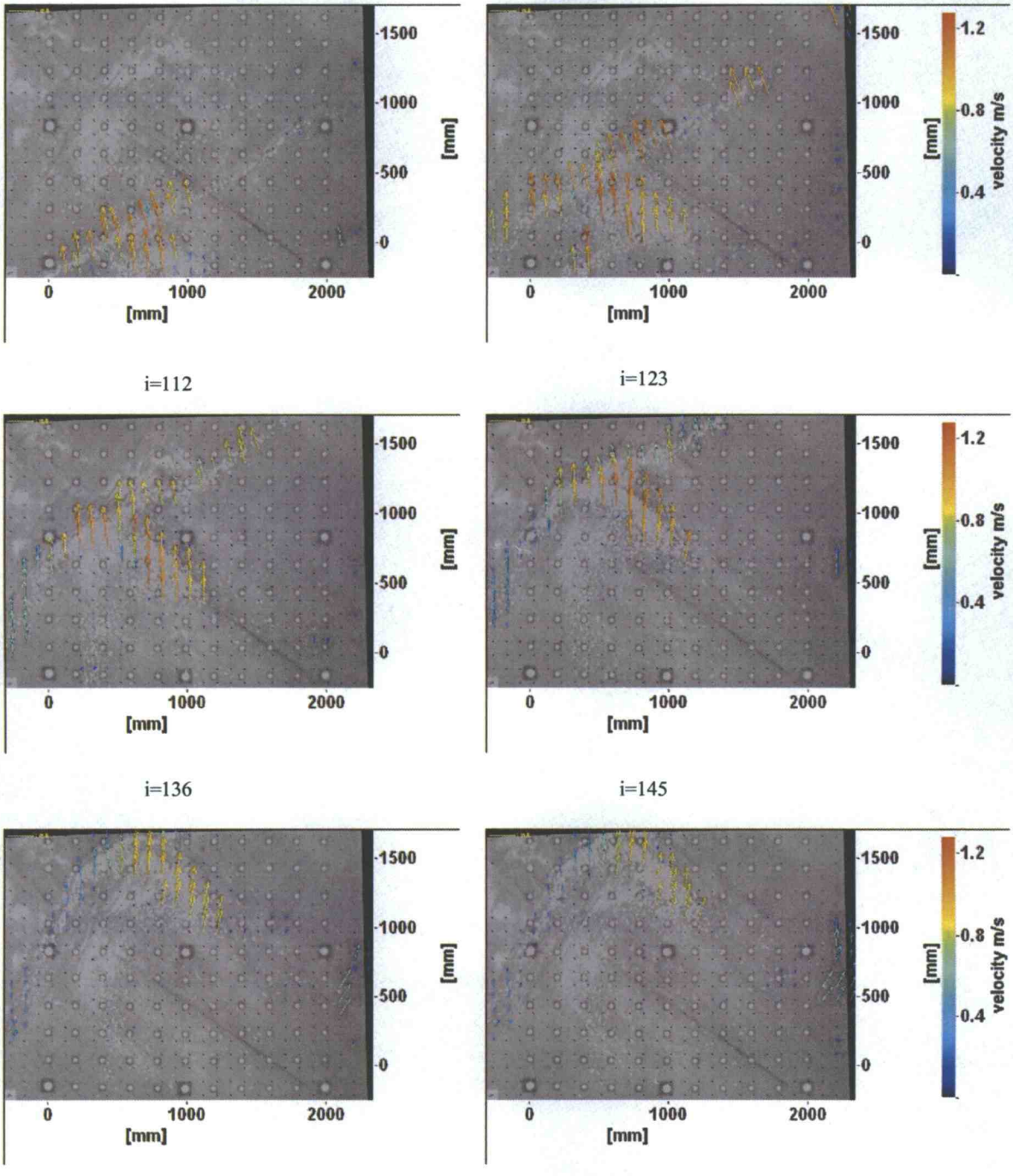

i=112 i=123

i=136 i=145

i=150 i=158

Figure D. 3: Vector field for test 3.

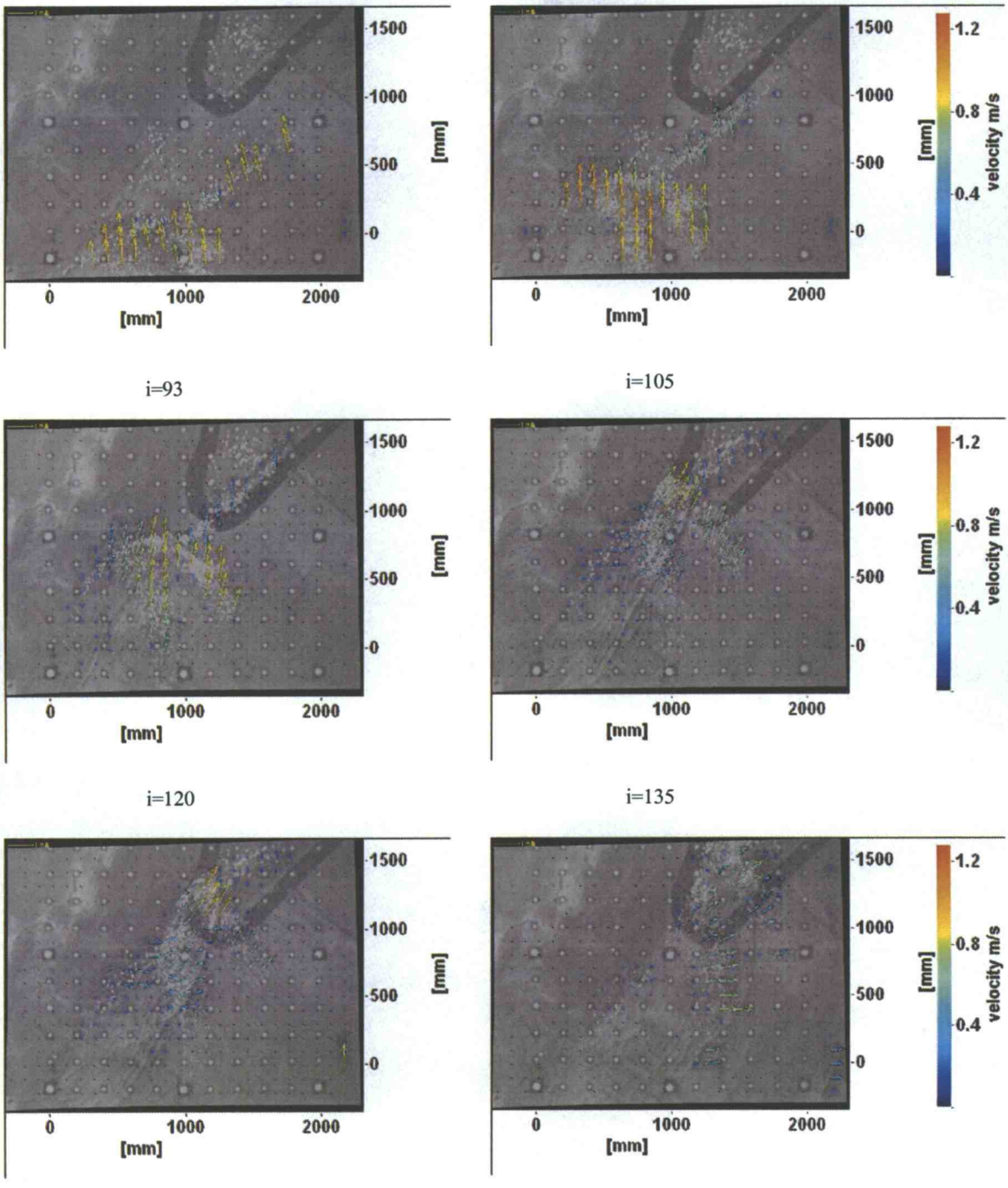

i=93 i=105

i=120 i=135

i=140 i=157

Figure D. 4: Vector field for test 4.

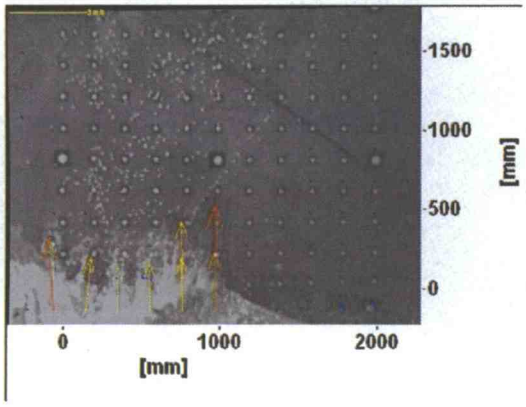

i=101

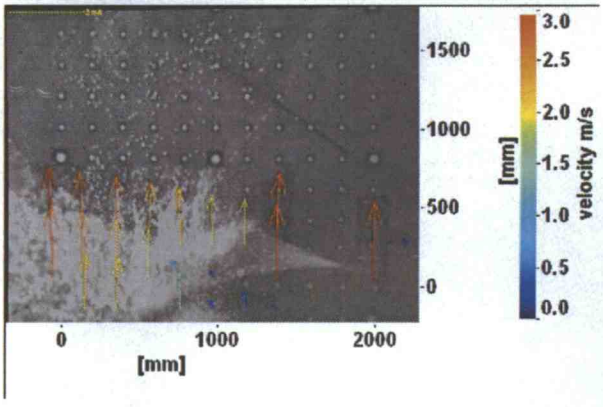

i=105

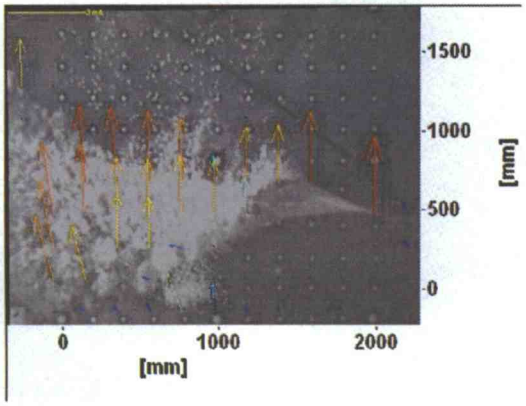

i=109

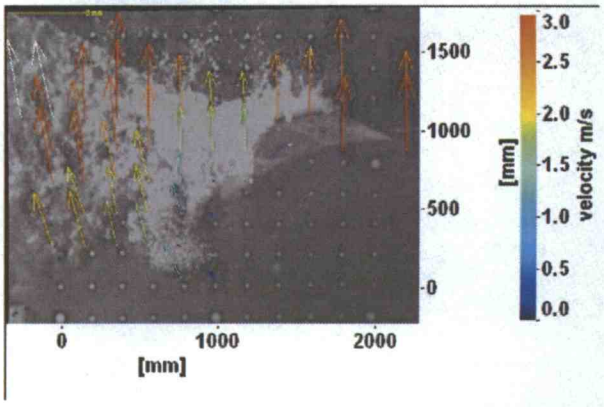

i=114

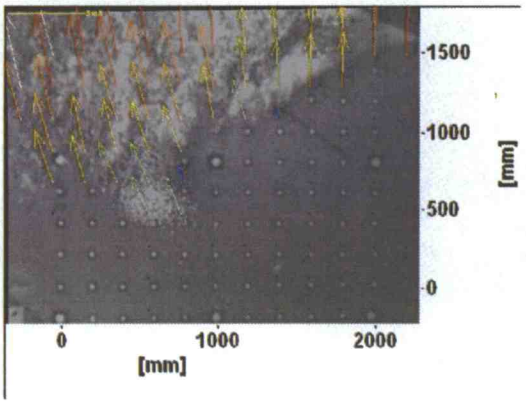

i=121

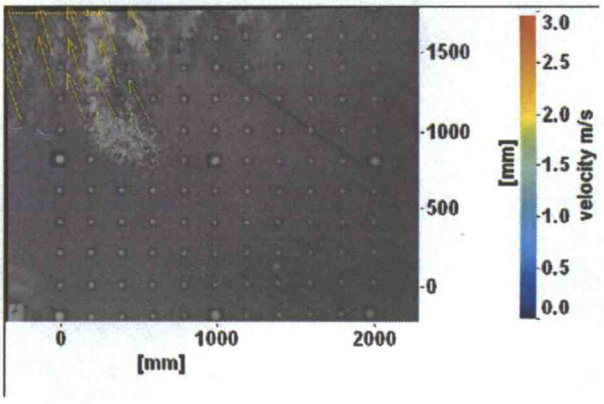

i=130

Figure D. 5: Vector field for test 5.

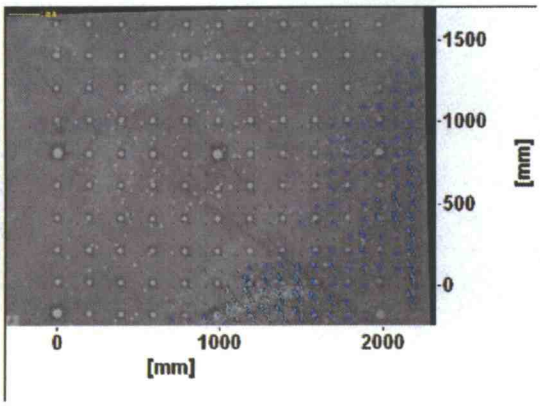

i=91

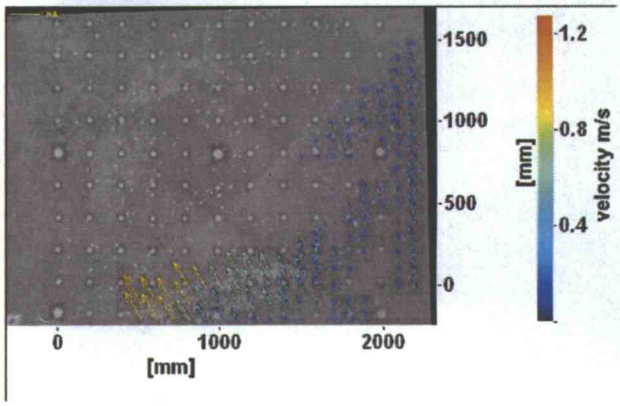

i=99

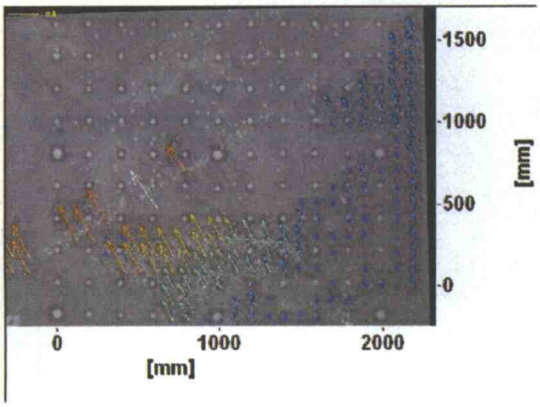

i=109

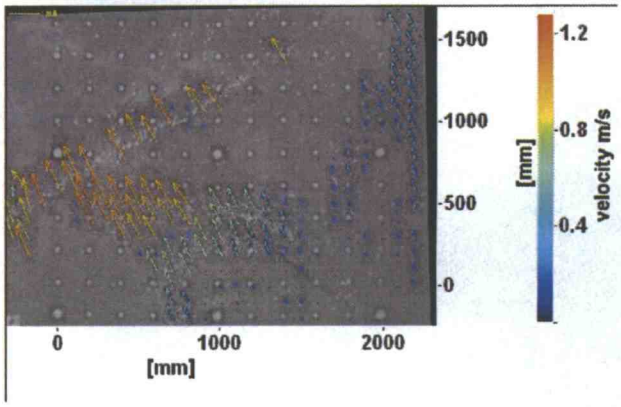

i=117

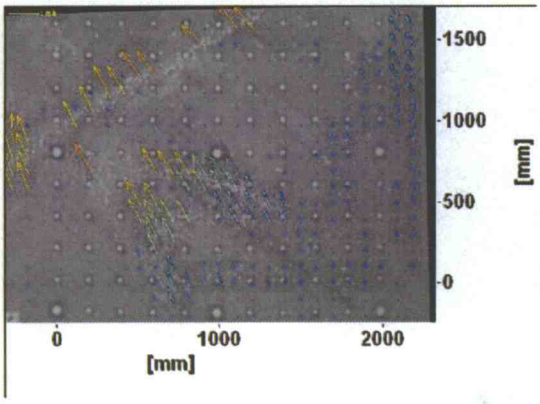

i=126

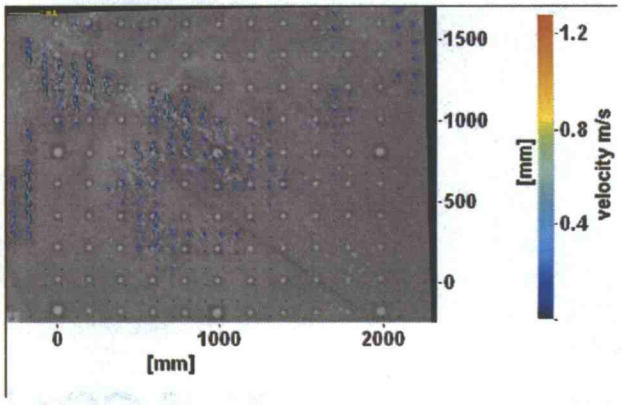

i=146

Figure D. 6: Vector field for test 6.

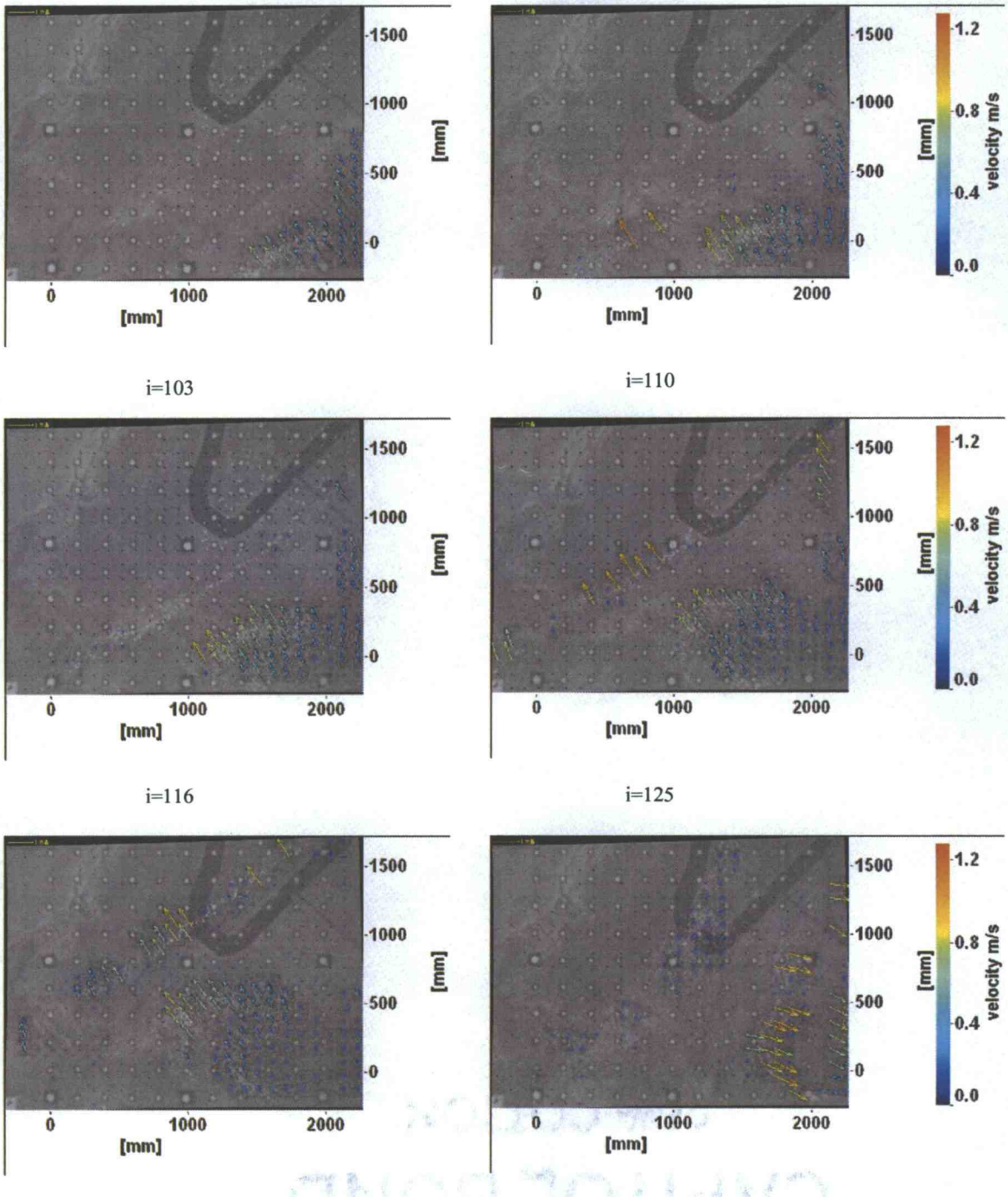

i=103 i=110

i=116 i=125

i=134 i=194

Figure D. 7: Vector field for test 7.

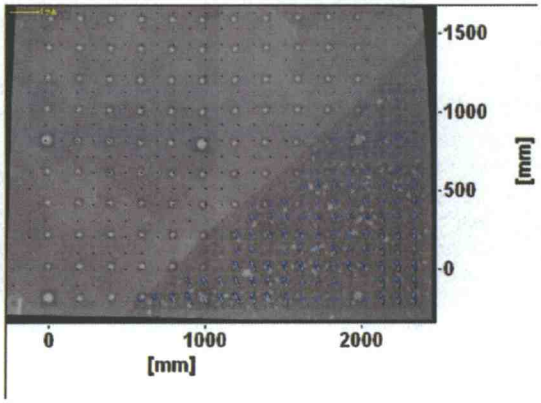

i=72

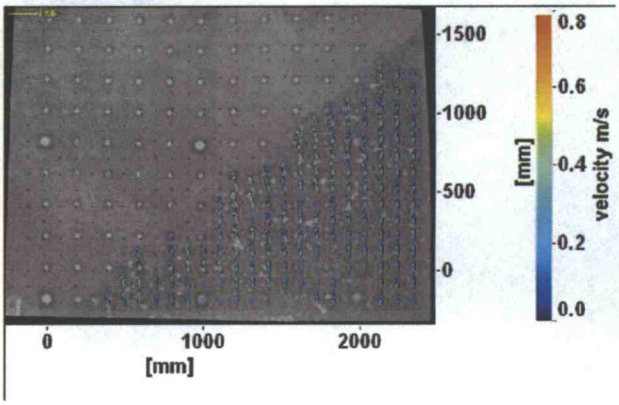

i=89

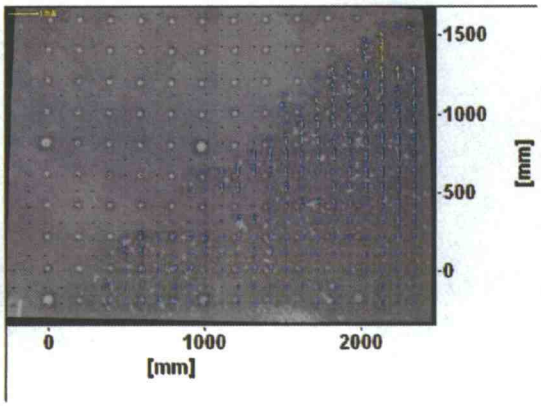

i=102

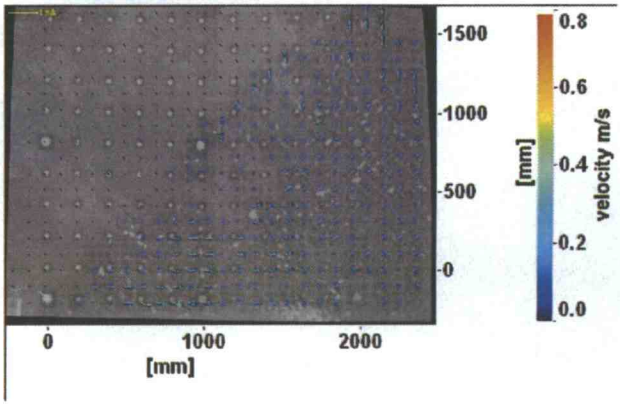

i=115

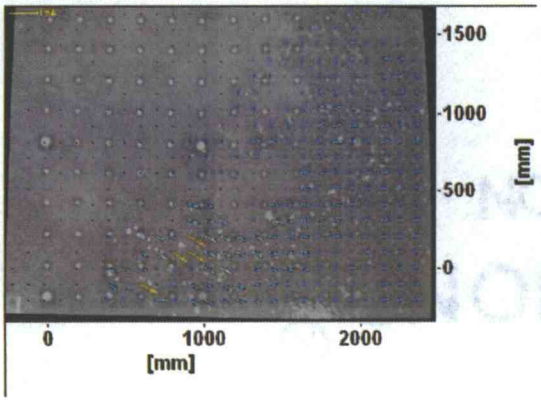

i=124

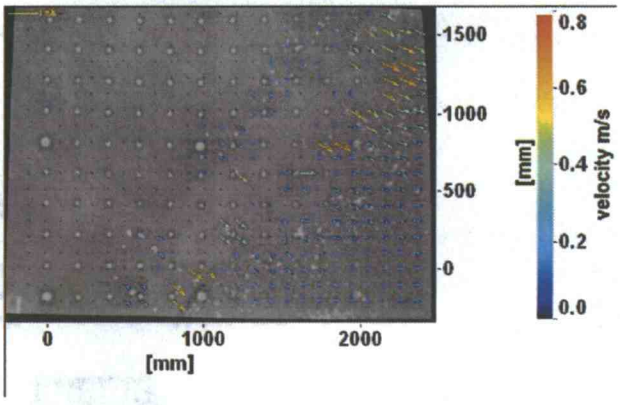

i=141

Figure D. 8: Vector field for test 8.

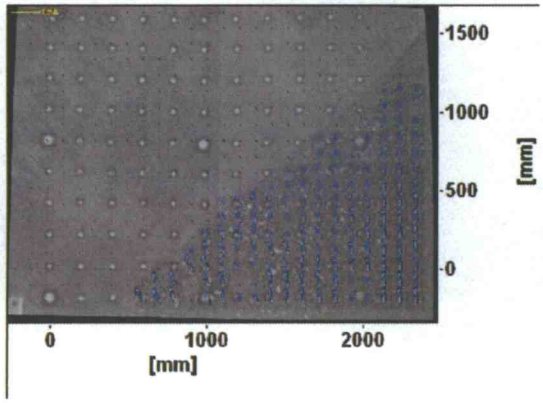

i=129

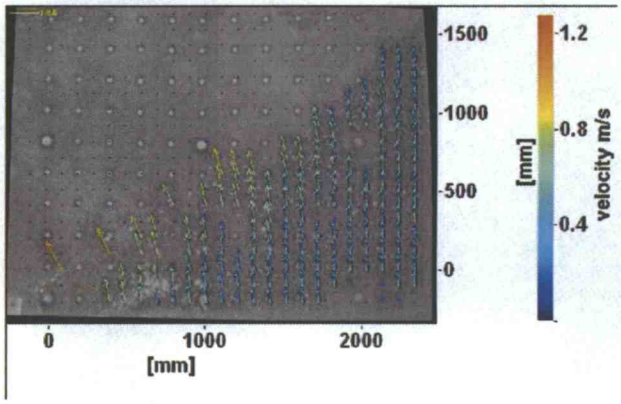

i=144

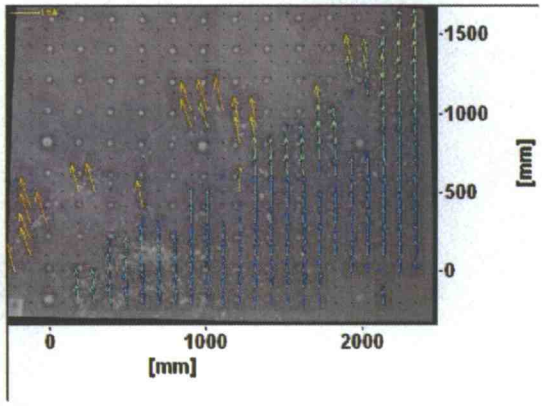

i=155

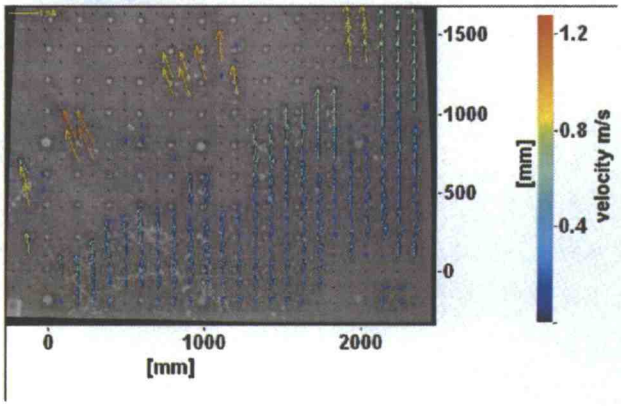

i=162

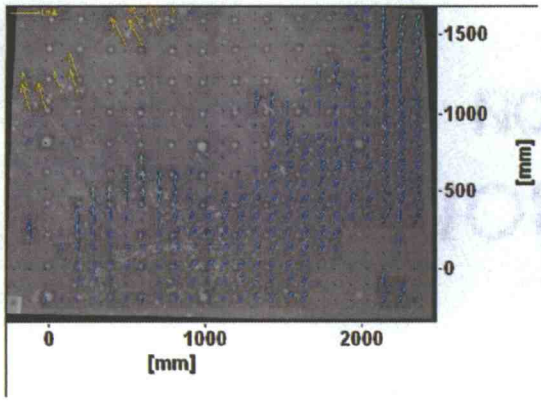

i=175

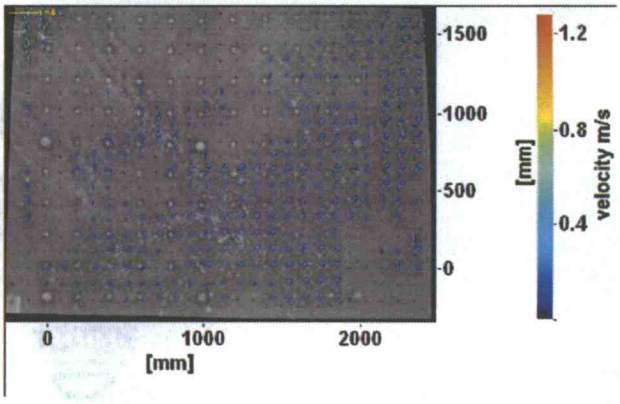

i=197

Figure D. 9: Vector field for test 9.

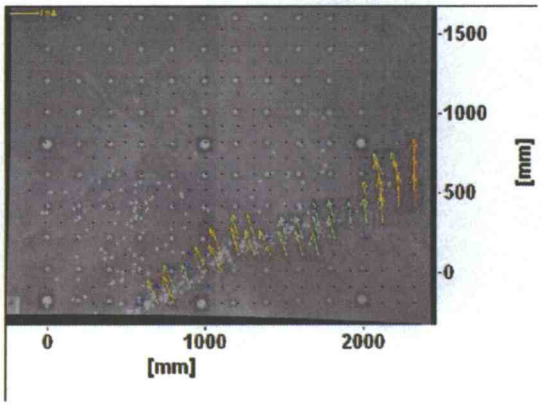

i=152

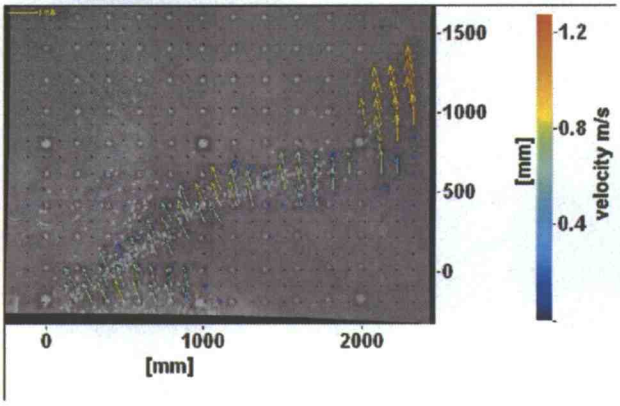

i=164

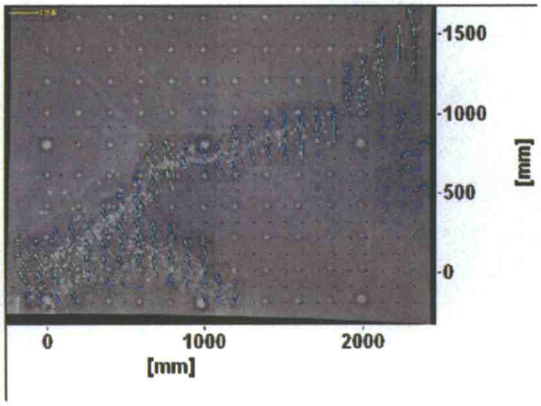

i=177

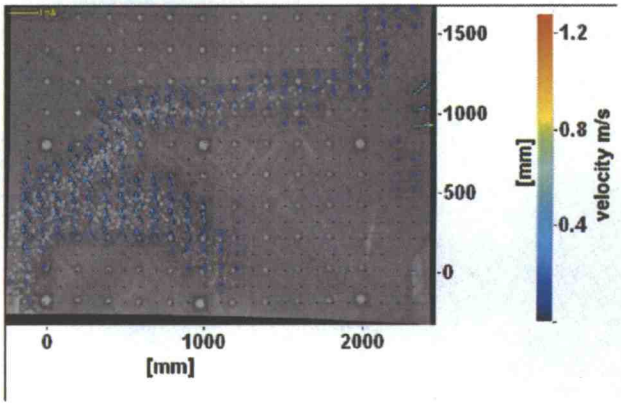

i=197

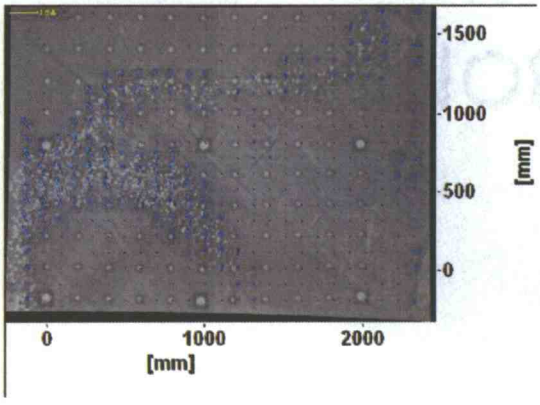

i=211

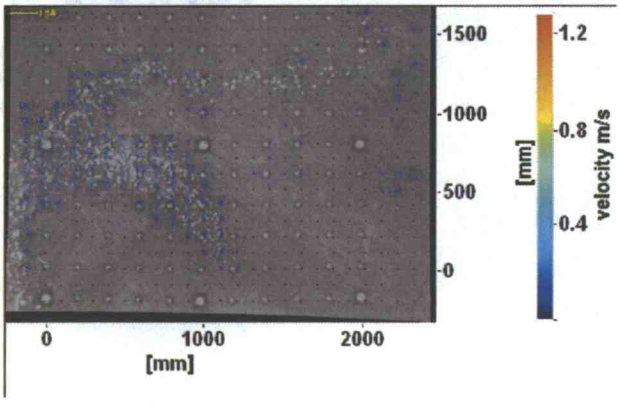

i=222

Figure D. 10: Vector field for test 10.

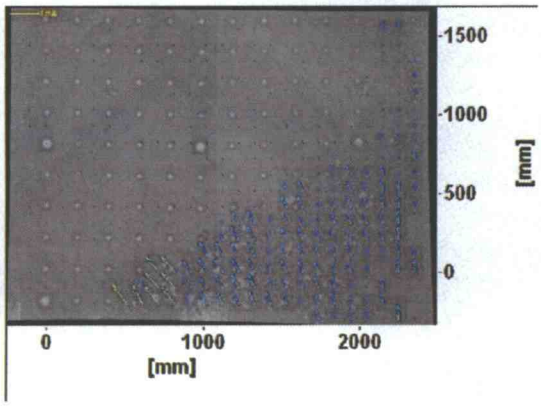

i=111

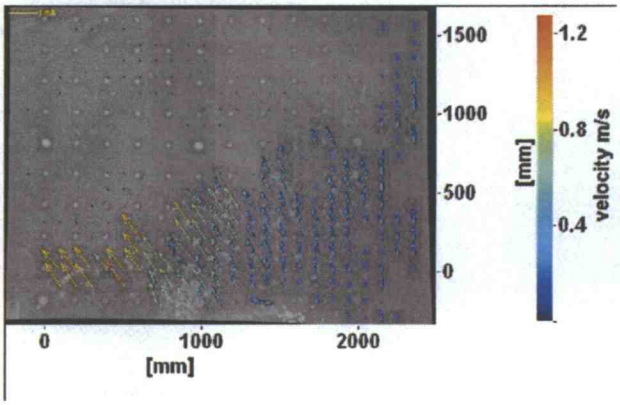

i=121

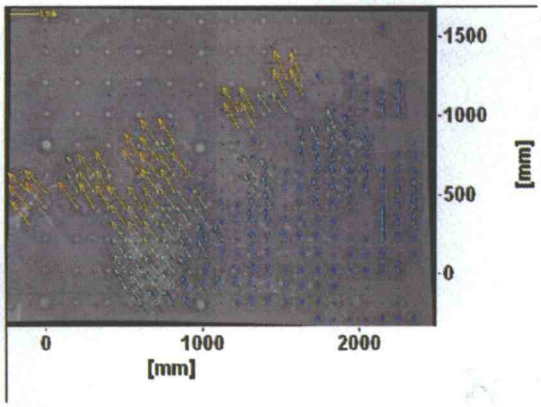

i=137

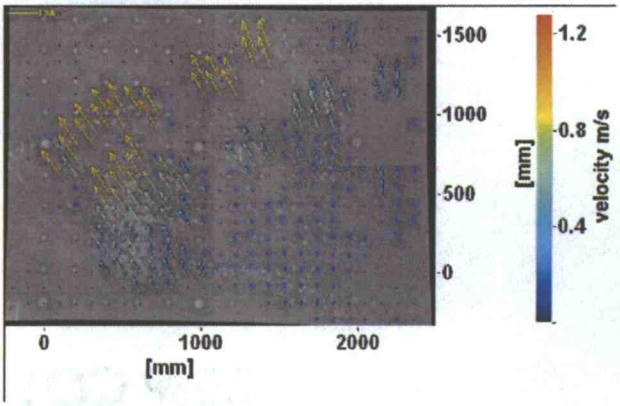

i=146

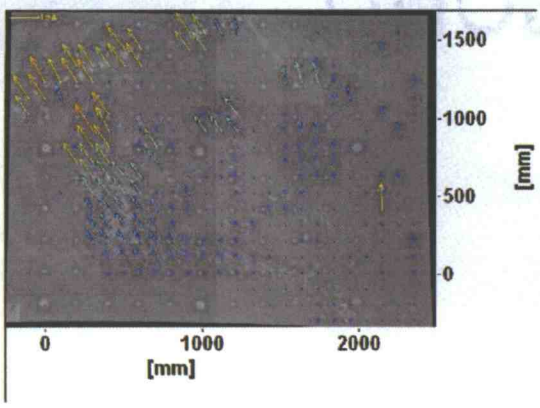

i=158

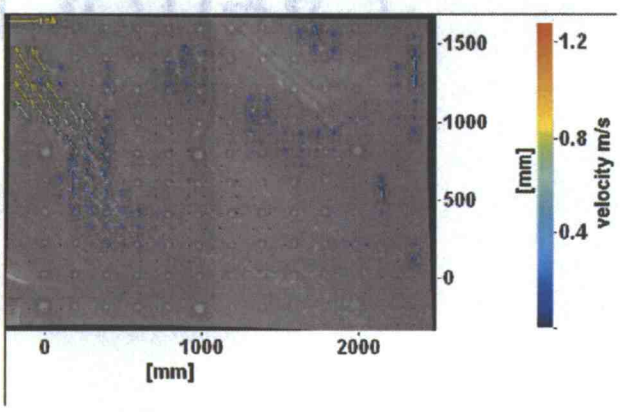

i=179

Figure D. 11: Vector field for test 11.

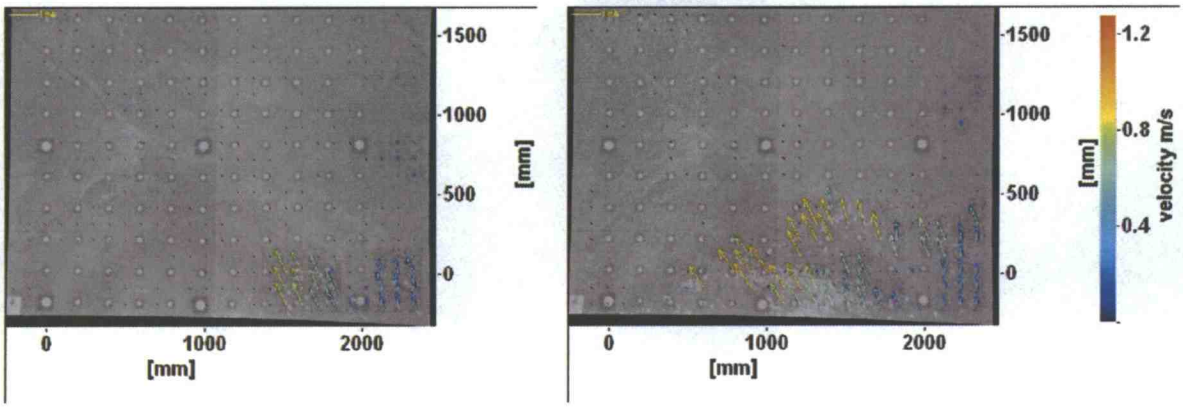

i=137 i=151

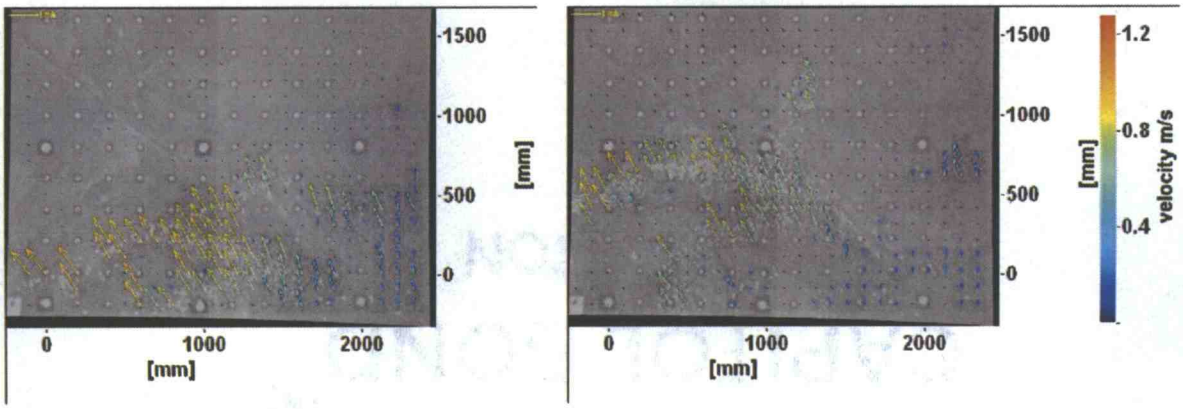

i=160 i=177

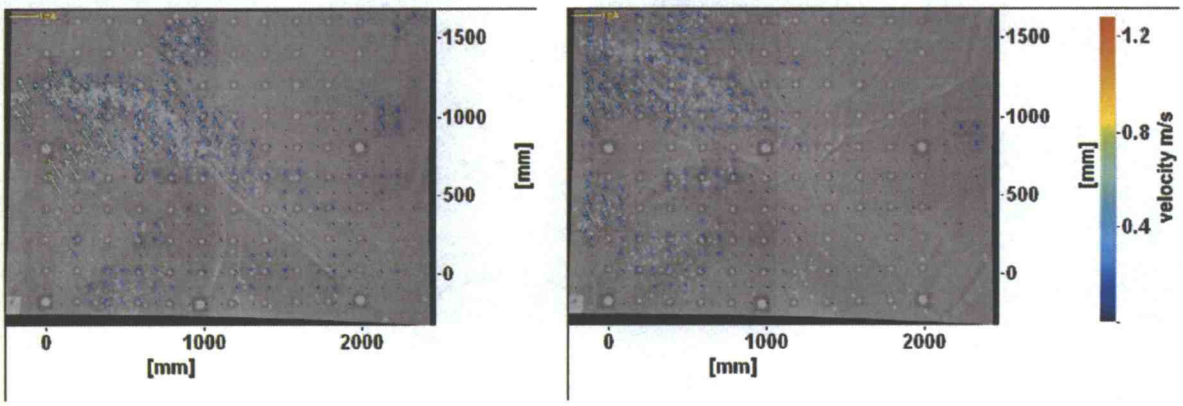

i=202 i=225

Figure D. 12: Vector field for test 12.

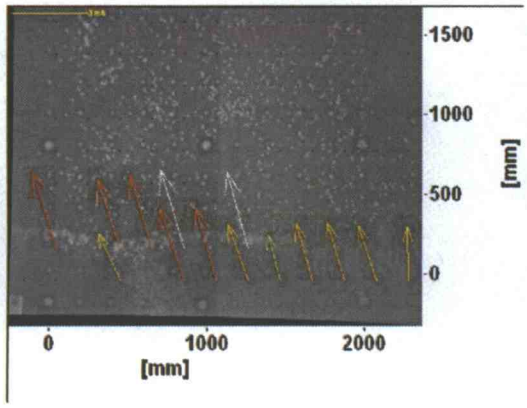

i=99

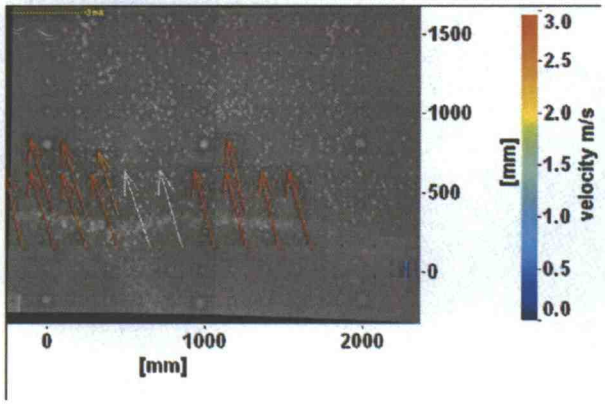

i=100

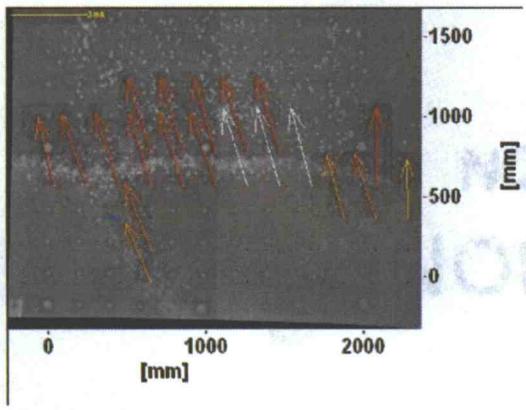

i=104

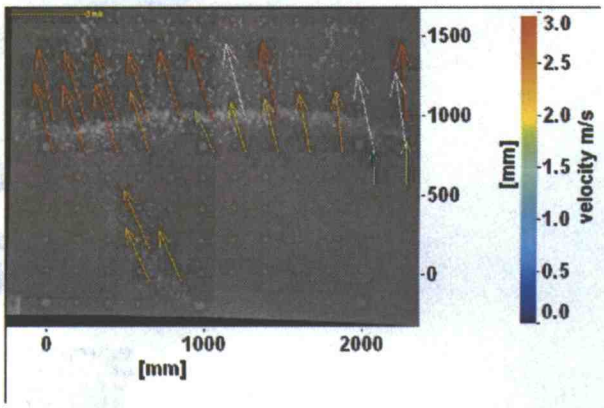

i=107

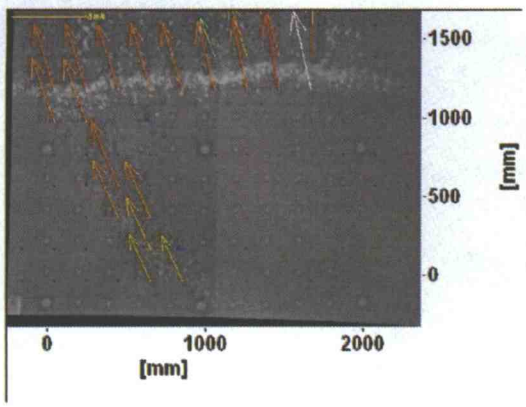

i=110

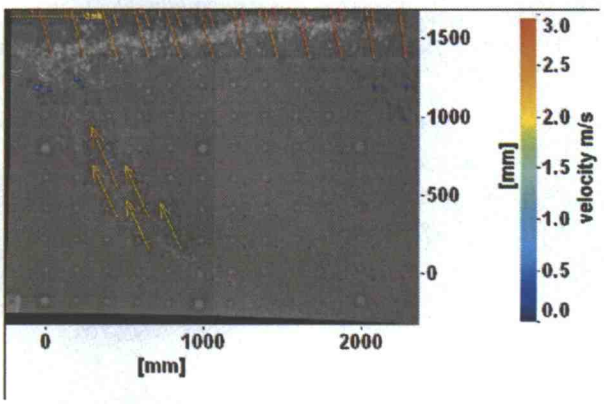

i=113

Figure D. 13: Vector field for test 13.

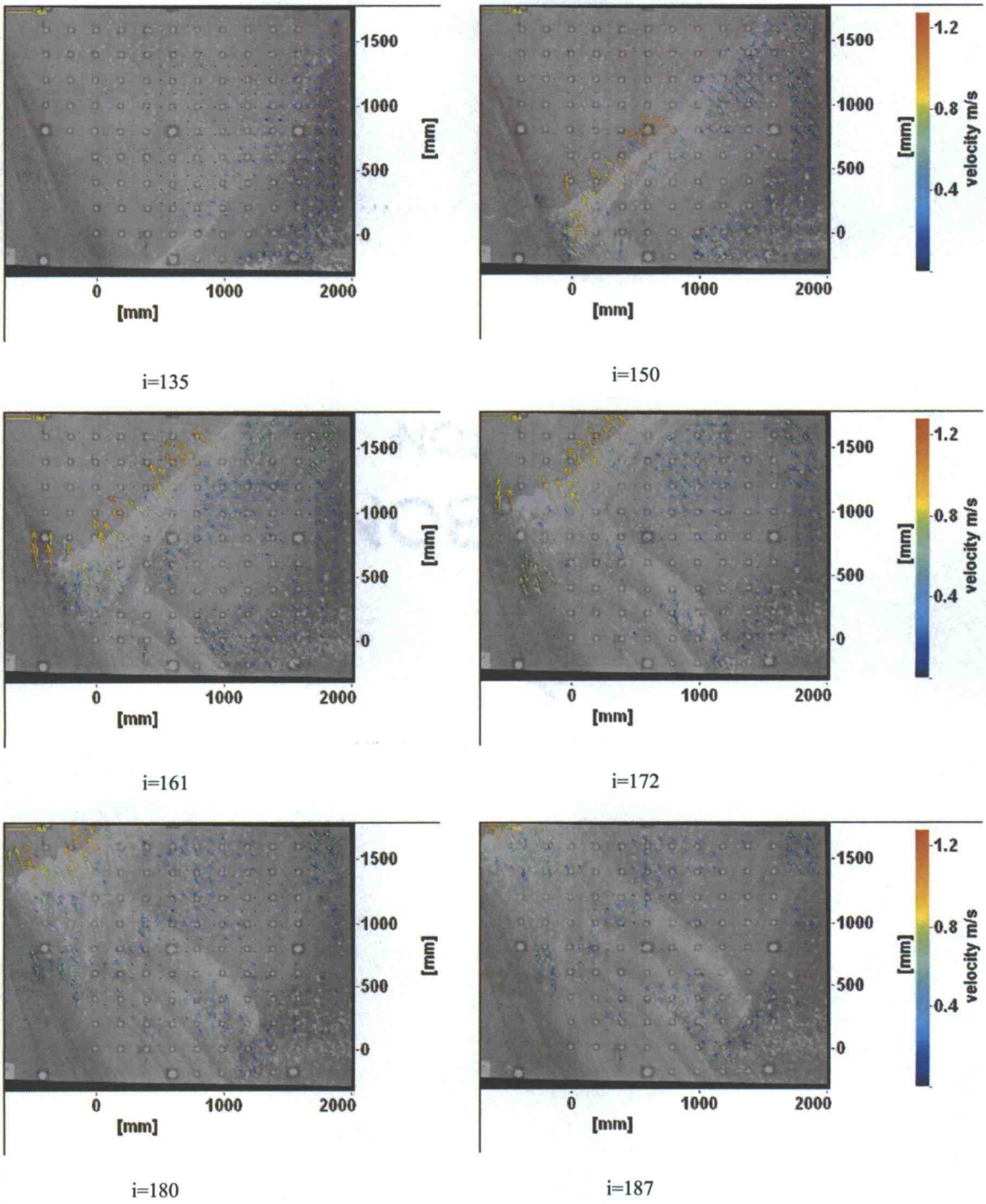

i=135 i=150

i=161 i=172

i=180 i=187

Figure D. 14: Vector field for test 14.

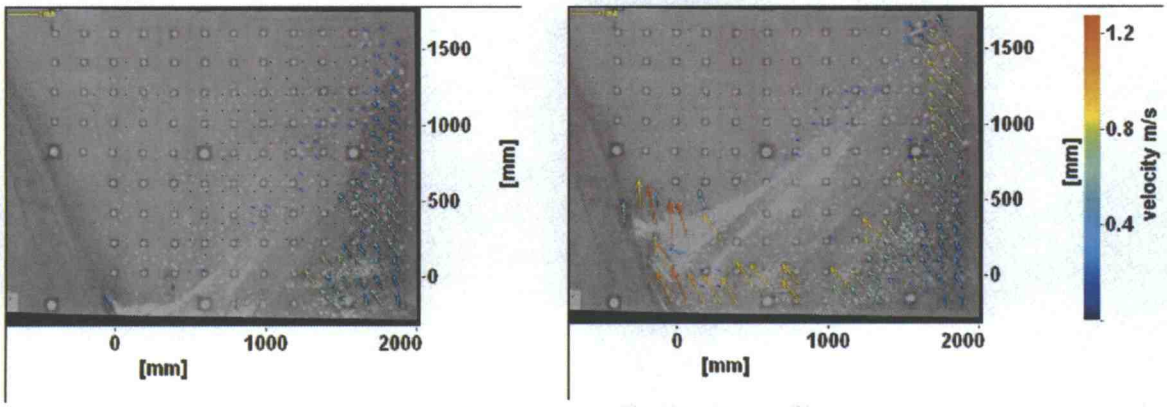

i=165 i=176

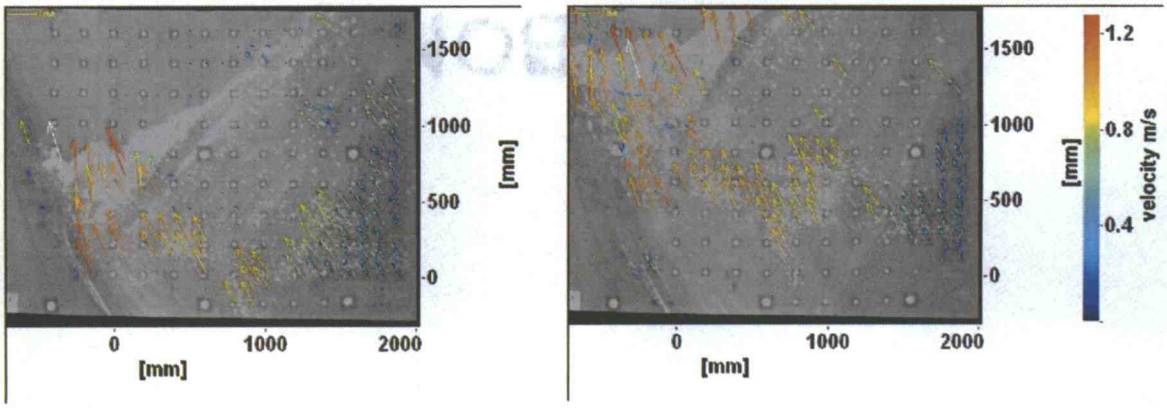

i=185 i=198

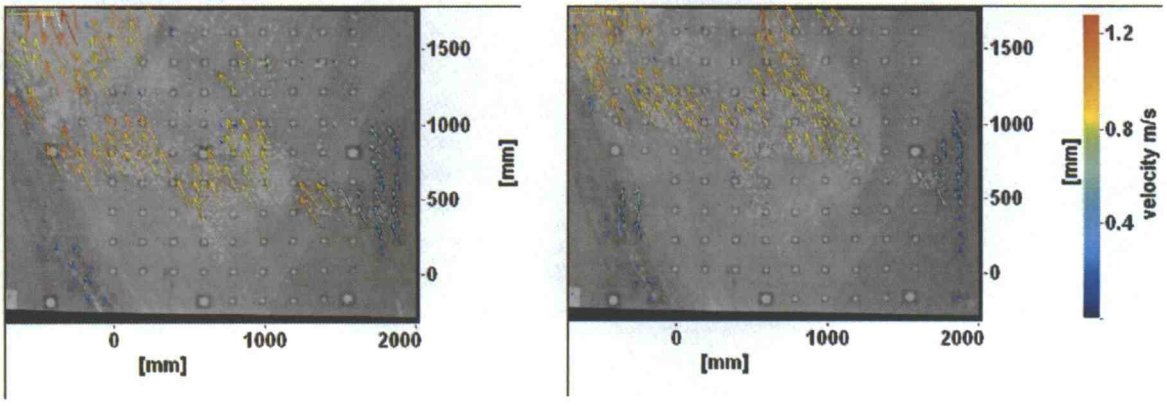

i=204 i=216

Figure D. 15: Vector field for test 15.

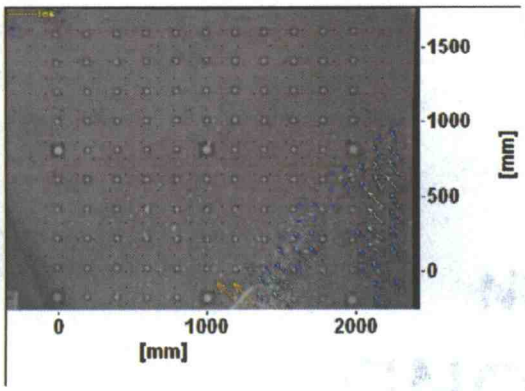

i=88

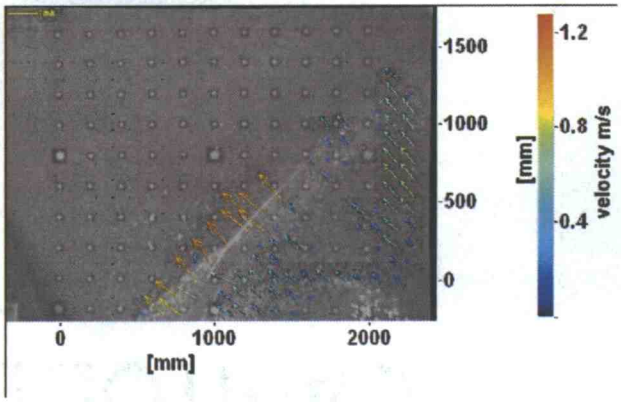

i=99

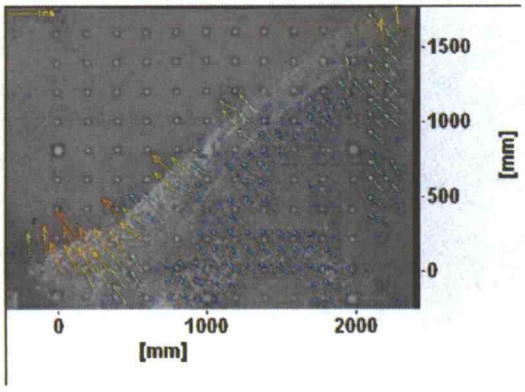

i=112

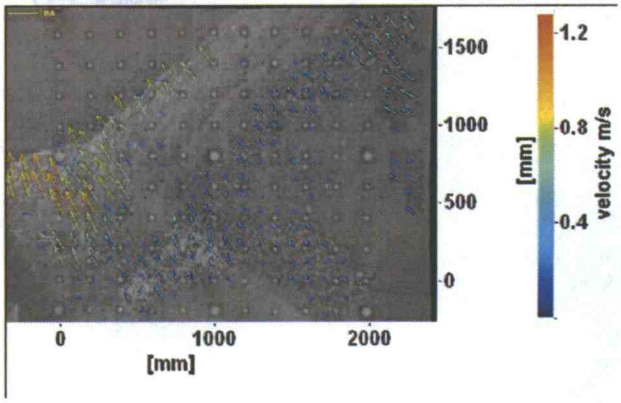

i=128

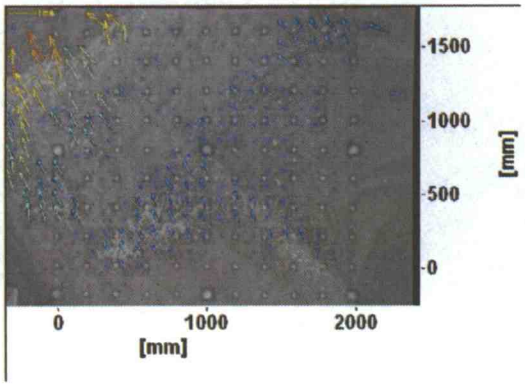

i=141

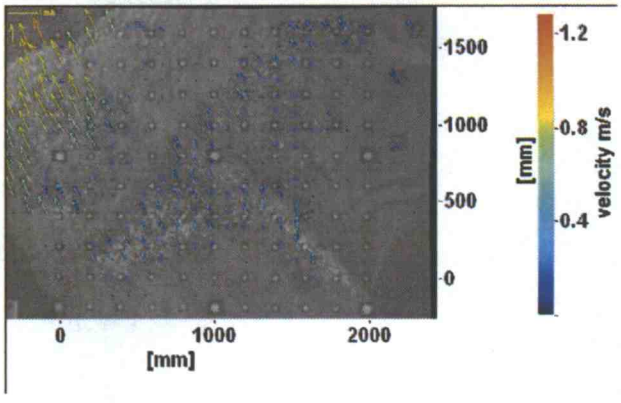

i=144

Figure D. 16: Vector field for test 16.

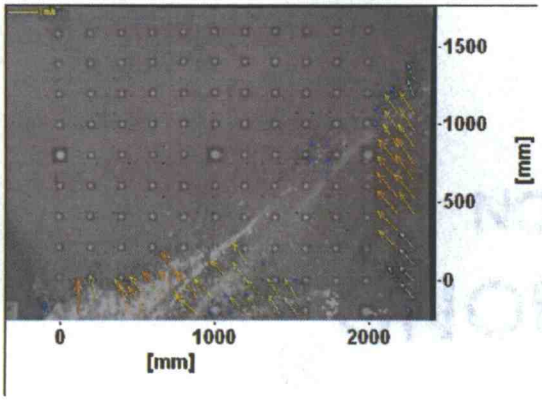

i=127

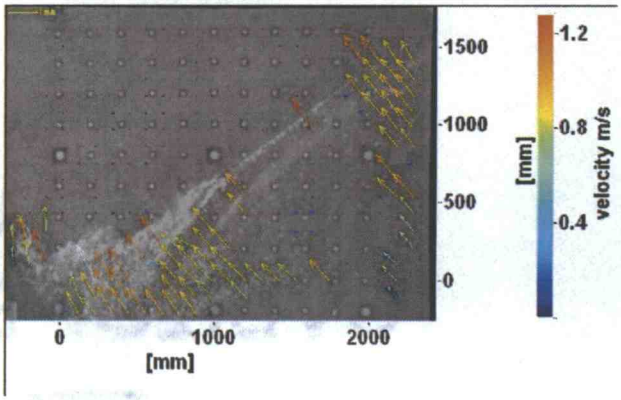

i=134

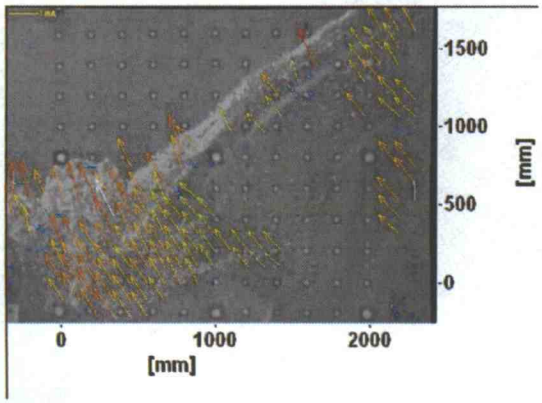

i=142

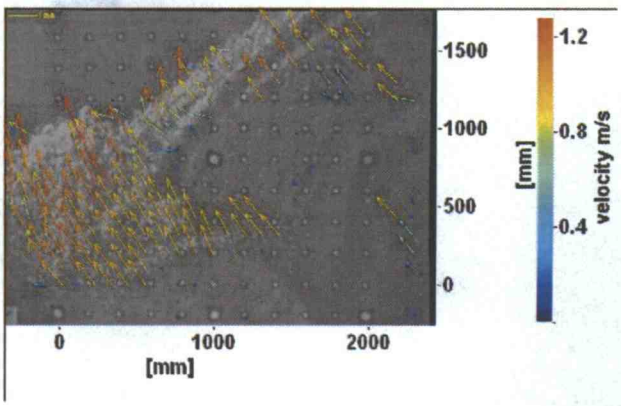

i=148

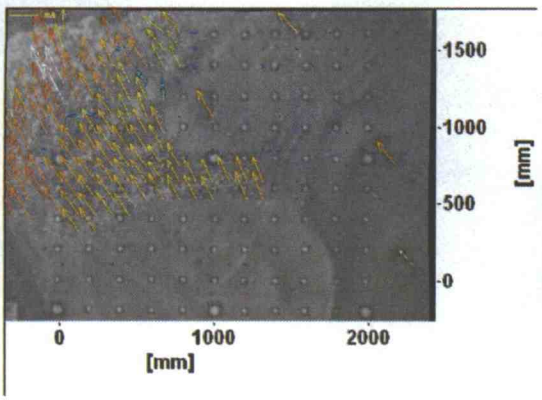

i=160

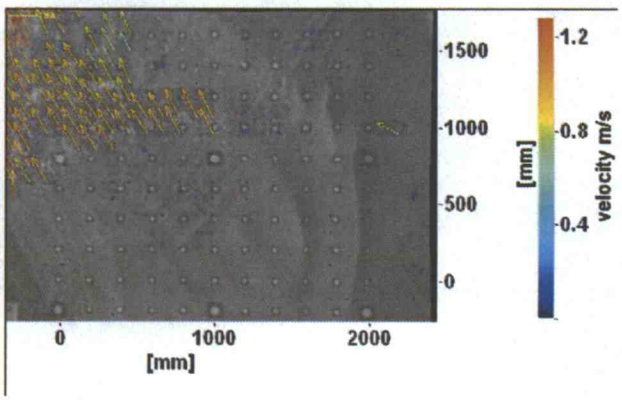

i=175

Figure D. 17: Vector field for test 17.

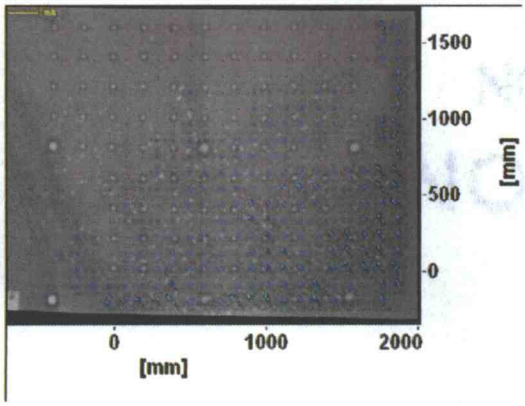

i=92

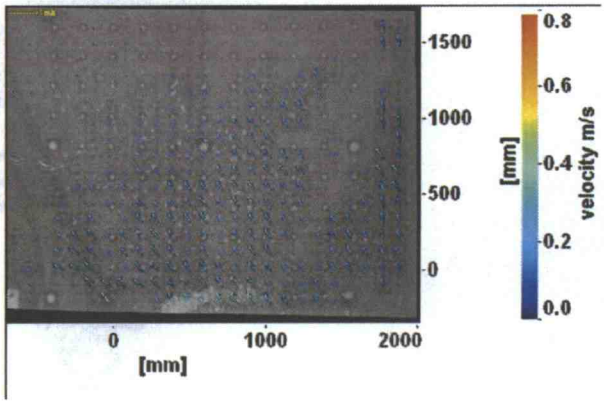

i=105

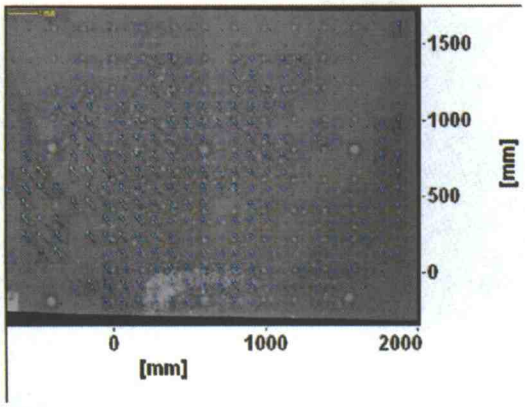

i=120

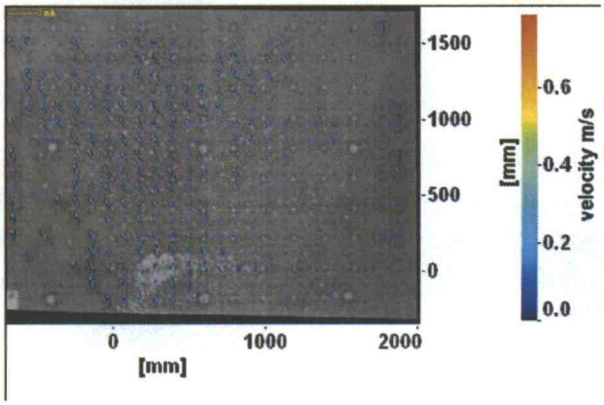

i=131

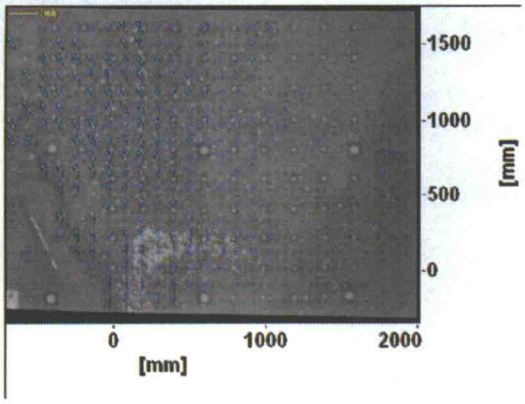

i=148

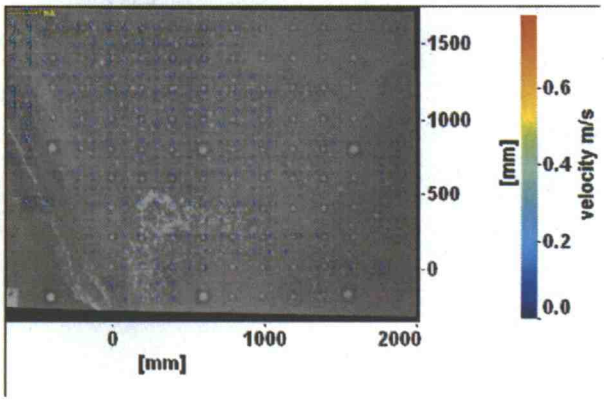

i=181

Figure D. 18: Vector field for test 18.

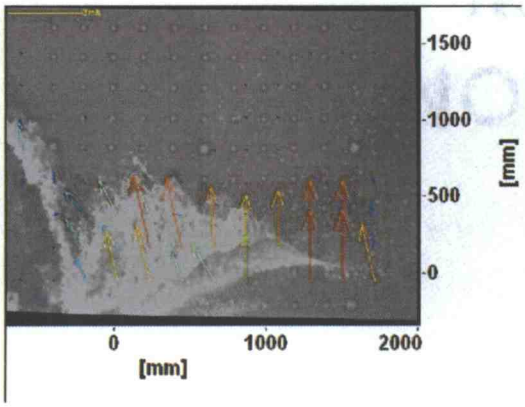

i=102

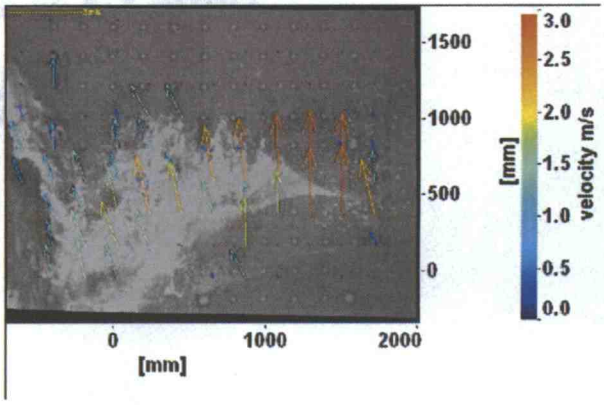

i=107

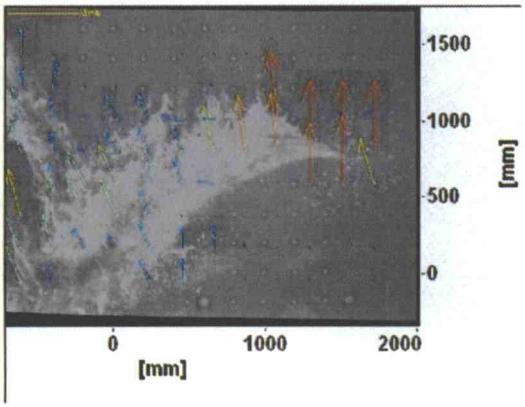

i=110

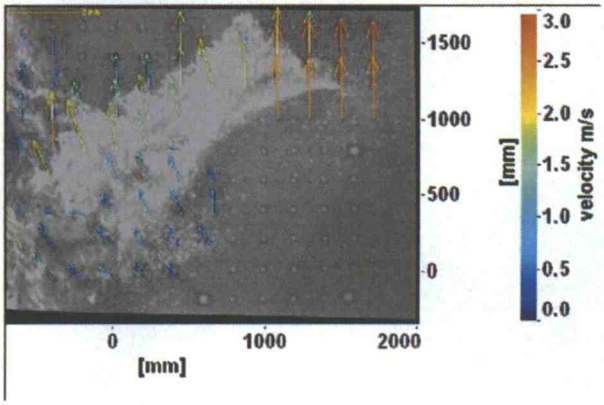

i=115

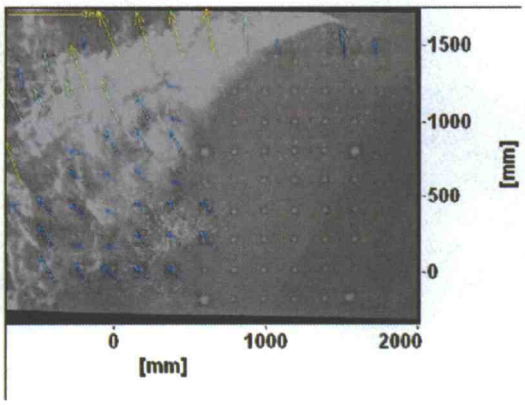

i=120

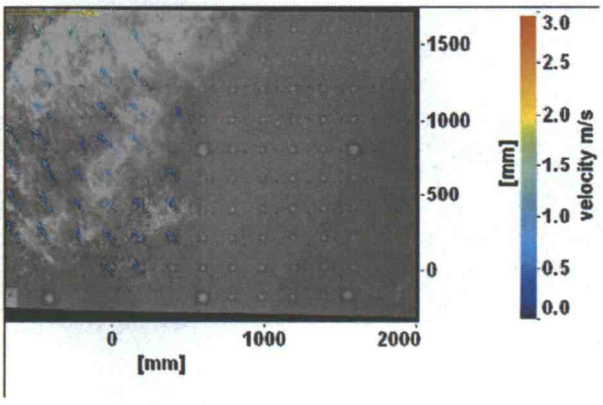

i=126

Figure D. 19: Vector field for test 19.

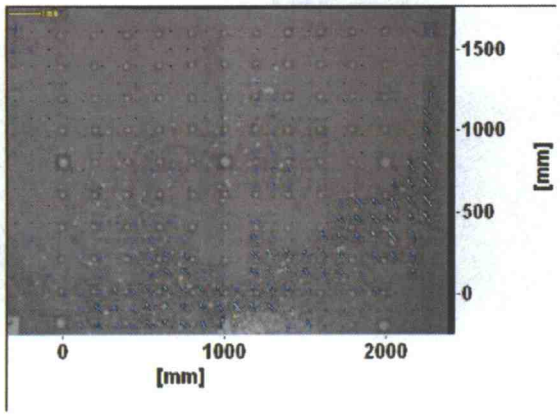

i=100

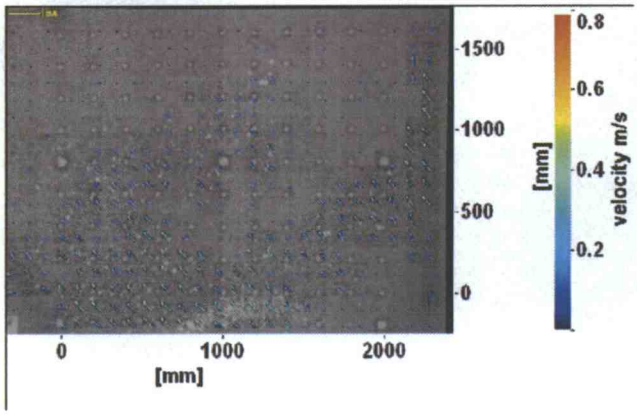

i=110

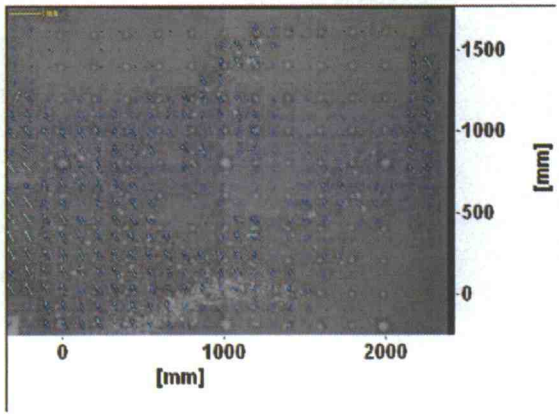

i=126

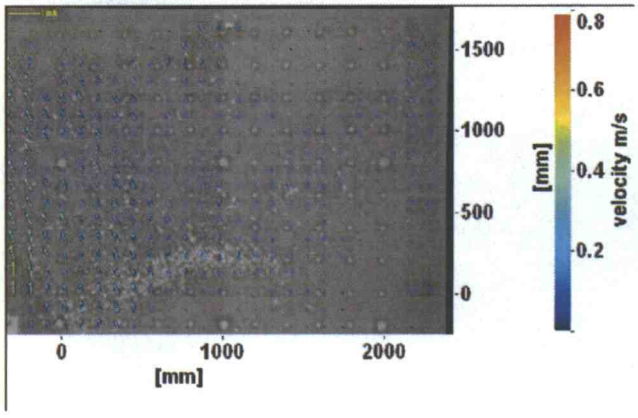

i=152

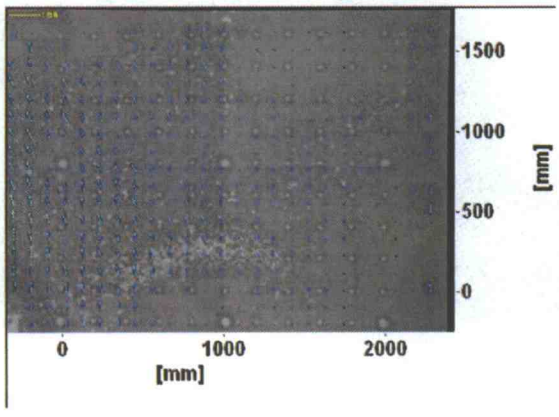

i=158

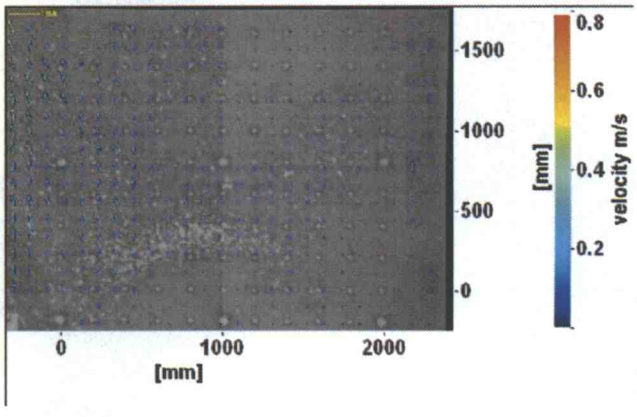

i=171

Figure D. 20: Vector field for test 20.

Appendix E

PIV accuracy for the breaking wave

In chapter 5.2 the PIV data overestimated the ADV data. It is considered that the ADV data is more reliable than that of PIV. This is because the PIV data has a close relation to several components such as brightness in the FOV, size of tracers, camera location and density of tracers in the FOV. Therefore, the comparison of the PIV and ADV was based on the idea that the ADV was more accurate than the PIV in terms of measuring velocity.

From Figure 60, it is concluded that the PIV shows good agreements with the ADV. It is worth noting that the PIV measure velocity by tracers floating on water while the ADV measures water particle velocity below the water surface. Therefore, good agreements of data for the PIV and the ADV mean that the velocity was nearly depth-uniform. This makes sense because the velocity profile along the water depth was uniform with shallow water conditions. However, it should be noted that this was a non-breaking wave case. For the breaking wave it is assumed that the PIV and ADV measure the velocity in different conditions; the PIV measured white water (i.e. breaking) and the ADV measured water particle under the white water (i.e. non breaking). Therefore, the ADV data for a breaking wave may not be comparable to the PIV data. It can be assumed that the water surface velocity may be at least larger than that of the ADV since it was a breaking wave.

In Figure 60, for the non-breaking wave case, the accuracy of the PIV data was verified by comparing it with the ADV data. However, the ADV data may not be used to compare with the PIV data for the breaking wave. Therefore, another approach to the PIV accuracy is needed for this case. As mentioned, the FOV was divided into small squares called interrogation windows. After the post processing was conducted, one vector was obtained for each interrogation window.

In an interrogation window, a vector was calculated by taking a tracer's displacement. Tracers' displacement was found by with a cross-correlation function which identifies the relationship of tracers at small time differences. In fact, most of the errors of the PIV occur during the process to find correlation. For example, if the light reflection occurs during the cross-correlation process, the PIV may lose sight of tracers and can not get the proper correlation after a small time period. Another example is the case for wave breaking. As mentioned before, the PIV seemed to trace not tracers, but the white water. However, as opposed to tracers, white water sometimes shows up immediately and diminishes suddenly. No white water will be 100% guaranteed to work as the proper tracers to calculate the velocity.

Here is one approach to checking the accuracy of the PIV by taking a very local velocity. A local velocity is calculated by a tracer displacement at a small time separation. From the raw image movie, some tracers can be found and traced at a small time separation. This is exactly the same procedure as what was done automatically by cross correlation.

Figure E. 1 shows a corrected image for test 19. A few tracers which could be recognized in the FOV were needed. Since tracers around white water were hard to recognize, the squared area was chosen to find some tracers in Figure E. 1.

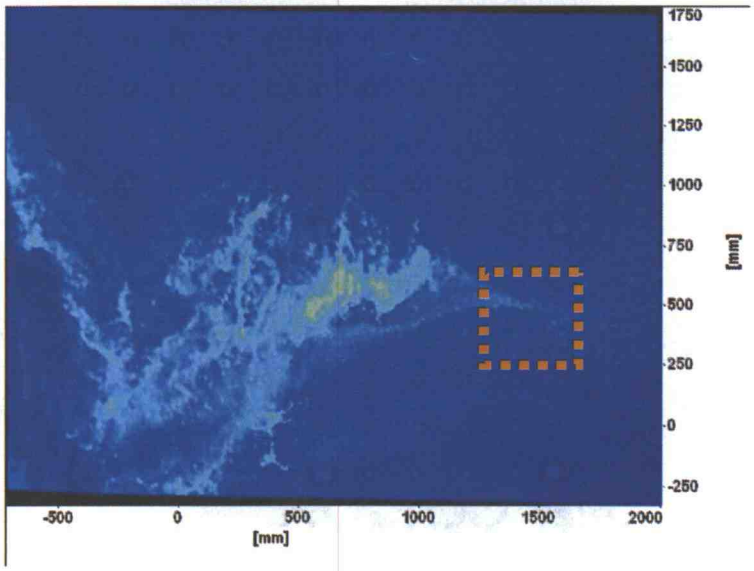

Figure E. 1: Selected area to find tracers.

Figure E. 2 shows the enlargement of the square in Figure E. 1. In Figure E. 2 (a), the four tracers were selected to check the displacements after a small time separation. Corresponding tracers are found in Figure E. 2 (b). The displacements and the calculated Vy values are listed in Table E. 1.

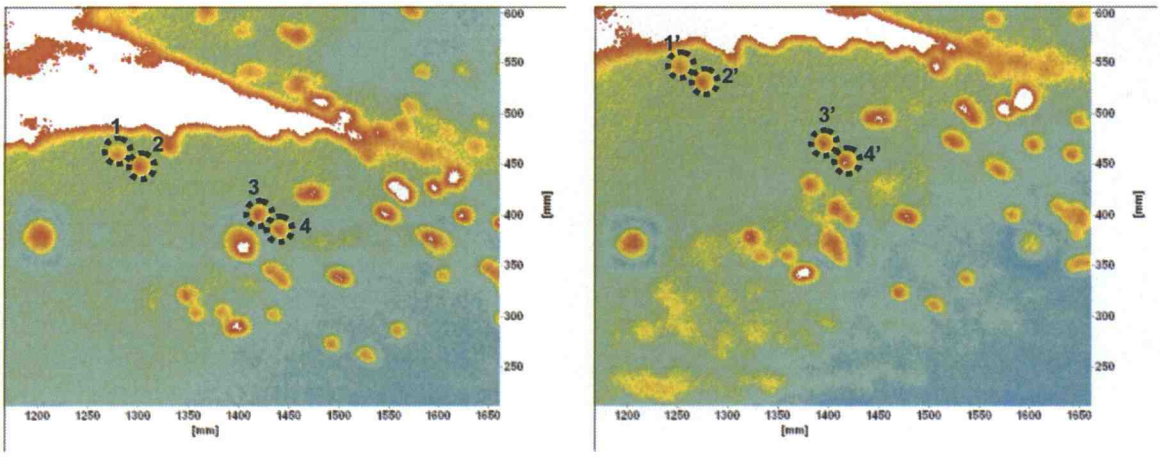

i = 108 i = 109

Figure E. 2: Corresponding tracers at a small time separation.

Table E. 1: Local velocity for each tracer.

Tracer Num.	i = 108		i = 109		Vy(m/s)
	X(mm)	Y(mm)	X(mm)	Y(mm)	
1	1281.47	456.409	1254.88	546.172	2.69
2	1306.41	444.774	1278.15	529.549	2.54
3	1426.09	394.906	1401.16	466.383	2.14
4	1447.70	379.946	1424.43	451.423	2.14

Figure E. 3 shows the scalar field of Vy overlaid on the vector field. This vector field was calculated from the 109th and 108th images. The squared area was identical to the squared area in Figure E. 1. This square consisted of four interrogation windows Corresponding Vy were listed in Table E. 2.

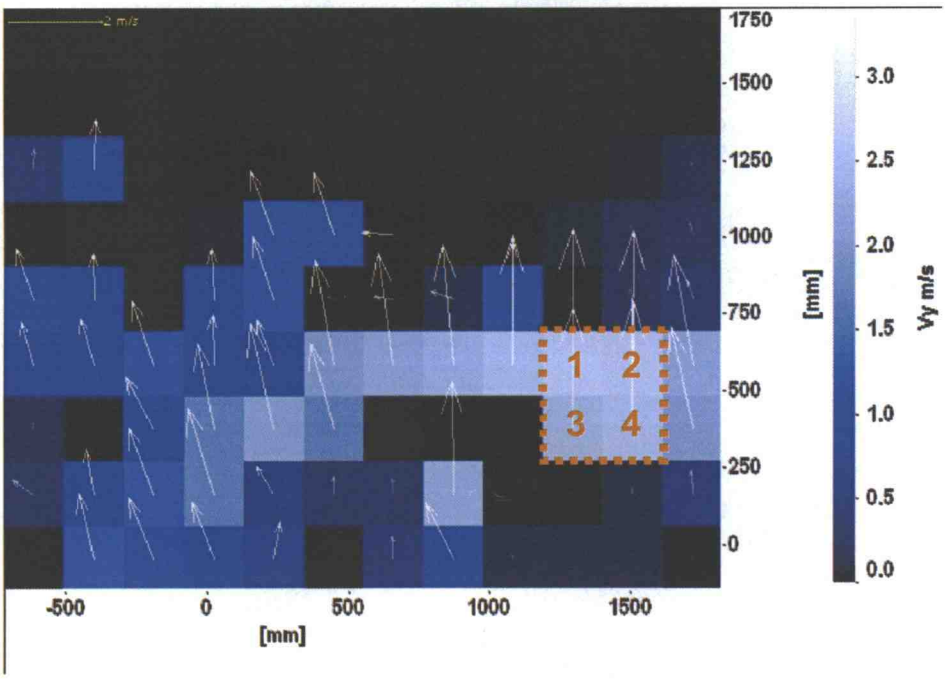

Figure E. 3: Corresponding interrogation windows for the selected area in the raw image.

Table E. 2: Local velocity at each interrogation window.

Interrogation window Num.	Dimension x(mm), y(mm)	Vy(m/s)
1	x= 1196~1407, y=476~690	2.653
2	x= 1407~1618, y=476~690	2.609
3	x= 1196~1407, y=262~476	2.384
4	x= 1407~1618, y=262~476	2.494

Comparing Tables E.1 and E.2, the local velocity for each tracer did not necessary represent the local velocity in the interrogation window which included it. However, it is true that the local velocity at the tracer was included when the local velocity of each interrogation window was calculated. In this sense, the calculated velocity at each interrogation window seems not far off from the local velocity at each tracer. Therefore, it is concluded that the velocities calculated from the PIV were more reliable to represent actual water surface velocity for the breaking wave than those from the ADV.

Bibliography

Briggs, M.J., Synolakis, C.E., Harkins, G.S., and Green, D.R. (1995). "Runup of solitary waves on a circular island." *Long-Wave Runup Models*. 363-374.

Briggs, M.J., Synolakis, C.E., Harkis, G.S., and Hughes, S.T. (1995). "Large scale three-dimensional laboratory measurements of tsunami inundation." *Tsunami: Progress in Prediction, Disaster Prevention and Warning*, 129-149.

Emarat, N., Christensen, E.D., Forehand, D.I.M., and Mayer, S. (2000). "A study of plunging breaker mechanics by PIV measurements and a Navier-Stokes solver." *Coast. Engrg,.* 891-901.

Fujita, I., Muste, M. and Kruger, A. (1998). Large-Scale Particle Image Velocimetry for Flow Analysis in Hydraulic Applications, • *J. Hydr. Res.*, 36(3), pp. 397-414.

Greated, C.A., Skyner, D.J., and Bruce, T. (1992). "Particle image velocimetry (PIV) in the coastal engineering laboratory." *Coast. Engrg,.* 212-225.

Kompenhans J, Raffet M, Willert C. (1998). "Particle image velocimetry – A practice guide.", Springer, Berlin.

LaVision (2005). "DaVis FlowMaster software manual for DaVis 7.0." LaVision Gmbh, Anna-Vandenhoeck-Ring 19, D-37081 Gottingen, Produced by LaVision Gmbh, Gottingen.

Liu, P. L.-F., Synolakis, C.E., and Yeh, H.H. (1991). "Report on the international workshop on long-wave run-up." *J. Fluid. Mech.*, 229, 675-688.

Tsutsumi, A., Shimamoto, T., Kawamoto, E., and Logan, J.M. (2000) "Nearshore flow velocity of southwest Hokkaido Earthquake tsunami." *J. Wtrwy. Port Coast. and Oc. Engrg.*, 126(3), 136-143.

Yamada, F., and Takikawa, K. (2000). "Determination of internal characteristicas of breaker deformation using a PIV technique that satisfies the mass conservation law." *Coast. Engrg,.* 902-915.